Reconfigurable Neural Probe for Chronic Recording

by

Boying Meng

Bachelor of Science, Electrical Engineering
Rice University, 2015

Submitted to the Department of Electrical Engineering and Computer Science
in Partial Fulfillment of the Requirements for the Degree of

Master of Science
at the
Massachusetts Institute of Technology

February 2018

Author____
Boying Meng
Department of Electrical Engineering and Computer Science
January 31, 2018

Certified by____
Joel Voldman
Professor of Electrical Engineering and Computer Science
Thesis Supervisor

Accepted by____
Leslie A. Kolodziejski
Professor of Electrical Engineering and Computer Science
Chair, Department Committee on Graduate Students

Reconfigurable Neural Probe for Chronic Recording

by

Boying Meng

Submitted to the Department of Electrical Engineering and Computer Science
on January 31, 2018
in Partial Fulfillment of the Requirements for the Degree of Master of Science

ABSTRACT

To facilitate the usage of neural prosthesis, a sustainable recording method of cleaner neural signals is desired. While invasive neural electrodes can record neural activities with less noise than non-invasive methods and provide the ideal spatial-temporal resolution of the recorded signal, one major challenge of this invasive method is the potential tissue responses. The scar tissue that forms around the penetrating tip of the electrode may significantly degrade the signal quality in time, which causes the reading to be unreliable in the long-term. Solving this problem is key to enabling chronic usage of neural prosthetic systems.

To tackle this challenge, previously Aalap Dighe has designed a reconfigurable neural probe using flexible polyimide material[1]. The design used a spring-like structure to allow the electrode probe tip to move further inside the brain weeks after the initial implantation surgery. The latest generation of the devices, Gen 3, was tested both *in vitro* and *in vivo* using rodent models.

In this thesis, the author continued the characterization of Gen 3 devices based on problems and observations occurred during the *in vivo* tests by Dighe, and proposed and tested an improved version of the device design, Gen 4. In particular, this thesis focused on solving the mechanical failure of some devices post-implantation and on reducing the instability of electrical properties of the electrodes. An improved structural mechanics simulation model of the design was used to characterize the mechanical properties of the devices. The simulation results were partially validated using benchtop load force tests, and were used to revise device design parameters for Gen 4. Experiments with Gen 4 devices showed that the new design met the design target well. Long-term *in vitro* impedance analysis of the electrodes was also performed using Gen 3 devices, which confirmed the observation of decreasing impedance over time in the previous *in vivo* tests. The results suggested delamination occurring between the polyimide layers, and the fabrication process was modified based on this hypothesis. Benchtop impedance tests of the new generation of devices confirmed that the delamination issue has been significantly improved.

Thesis Supervisor: Joel Voldman

Title: Professor of Electrical Engineering and Computer Science

---

[1] A. Dighe, "Reconfigurable Neural Probes for Chronic Electrical Recording," Cambridge, MA, 2015.

ACKNOWLEDGEMENTS

I would like to express my sincere gratitude to my thesis advisor and research mentor, Professor Joel Voldman, for his continuous support for the project. He introduced me not only to the opportunity to work on this project, but also to the fascinating field of bio-MEMS and the precious hands-on experience of micro-fabrication. Thoroughout the process, he patiently provided me with crucial technical guidance, as well as general directions and advice for performing academic research.

I would like to thank Aalap Dighe for his brilliance and hardwork in designing and characterizing the previous generations of the devices, which laid the foundation for this project.

I would like to thank the National Science Foundation and the Center for Sensorimotor Neural Engineering for sponsoring this project.

The fabrication of the devices was done in MIT Microsystems Technology Laboratories (MTL), and the benchtop experiments were performed in MIT Research Lab for Electronics (RLE). I would like to especially thank the MTL staff for providing thorough technical support. The training on using fabrication tools and their suggestions on how to tackle specific challenges in my fabrication process were invaluable.

Special thanks to Lin Zhu (Southeast University, Nanjing, China) for his assistance on solving the stress singularity issue in the non-linear FEA model of the device. The mechanical characterization of the device would not have been possible without his advice.

And last but not the least, I would also like to thank all members of the Voldman group for providing helpful suggestions and feedbacks on my project updates throughout the years, and all my friends and family for their love and support.

Table of Contents

Table of Contents 5
Table of Figures 7
Chapter 1: Introduction 11
  1.1 Background and Motivation 11
    1.1.1 Neural Prosthetics and Common Recording Methods 11
    1.1.2 Challenges with Invasive Electrodes: Tissue Responses 11
    1.1.3 Current Approaches to Reduce Effect by Tissue Responses 13
    1.1.4 Our Approach: Reconfigurable MEMS Neural Probe 14
  1.2 Thesis Overview 15
Chapter 2: Gen 3 Device Characterization 17
  2.1 Introduction 17
  2.2 Gen 3 Mechanical Analysis 17
    2.2.1 Re-Visiting the Original Linear Analytic Model 18
    2.2.2 Limitations of the Original Linear Model 21
    2.2.3 FEA Simulation Model 21
    2.2.4 Simulation Results: Stress vs. Deflection Relationships 30
    2.2.5 Simulation Results: Force vs. Deflection Relationships 31
    2.2.6 Limitations of the FEA Model 31
    2.2.7 A Review of Gen 3 Parameters 32
    2.2.8 Verification of FEA Results: Deflection vs. Load Force Test 34
  2.3 Gen 3 Impedance Test 37
    2.3.1 Experiment Setup 37
    2.3.2 Results and Discussions 39
  2.4 Conclusions and Directions for Gen 4 Design 44
Chapter 3: Gen 4 Device Design and Testing 45
  3.1 Introduction 45
  3.2 Gen 4 Device Parameters 45
    3.2.1 Effects of Design Parameters on Stress-Deflection Relationship 46
    3.2.2 Proposed Leg Parameters 47
    3.2.3 Force-Deflection Relationships using Chosen Parameters 50
    3.2.4 Leg Separation 51
    3.2.5 Summary: Proposed Variations of Gen 4 Devices 52

3.3 Device Design and Mask Layout 52
  3.3.1 Device Schematics 52
  3.3.2 Test Devices for Deflection vs. Force Measurement 53
  3.3.3 Mask Layout 54
3.4 Gen 4 Device Fabrication 54
  3.4.1 Fabrication Process Flow 55
  3.4.2 Main Adjustments from Gen 3 Process 57
  3.4.3 Lessons Learned from Fabrication Modifications 58
3.5 Gen 4 Benchtop Characterization: Mechanical Performance 59
  3.5.1 Deflections with Load Forces 59
  3.5.2 Challenges with the Elasticity Test 62
  3.5.3 Discussions and Future Directions 64
3.6 Gen 4 Benchtop Characterization: Impedance 65
  3.6.1 Device 1 65
  3.6.2 Device 2 68
  3.6.3 Discussions and Future Directions 69
3.7 Conclusions 69
Chapter 4: Conclusions and Future Directions 71
4.1 Contributions 71
  4.1.1 Mechanical Model and Benchtop Experiment Setup 71
  4.1.2 Real-Time Impedance Monitoring 71
4.2 Future Directions 71
  4.2.1 Fabrication 71
  4.2.2 Mechanical and Electrical Characterization 72

Table of Figures

Figure 1-1 and caption adapted from [3] by [2]- Time course of glial scar formation at four time points as imaged by GFAP staining. At 2 and 4-week time points, the astrocytic processes fall back into the void left by the probe extraction before tissue processing. By 6 weeks, the processes have interwoven to form a stronger, more dense sheath surrounding the implant. Minimal changes between the 6- and 12-week time points indicate the glial scar completion within 6 weeks. 12

Figure 1-2 adapted from [4] - Aggregated data from eight chronic animals to show the trend of the weekly array yield for long-term microarray implants (≥6 weeks). 12

Figure 1-3 adapted from [11] - Device operation schematic by A. Dighe. 14

Figure 1-4 – Magnitudes of the impedances of the 16 electrode sites measured in benchtop tests pre-implantation, immediately post-implantation, and 1, 2, 5 weeks post-implantation using data from [11]. 15

Figure 2-1 – Model of the device leg in the x-y plane. Figure adapted from [11]. 18

Figure 2-2 – Model of a pair of leg, adapted from [11]. 19

Figure 2-3 – Center load on beam with two fixed supports. Figure from [13]. 19

Figure 2-4 – (a) The simple model of the leg using a beam with rectangular cross-section. (b) An example surface plot of the FEA result of von Mises stress on the deformed beam using a mesh of 2305 elements. Beam length (z-direction) l = $500\mu m$, width (x-direction) b = $20\mu m$, and height (z-direction) h = $10\mu m$. 23

Figure 2-5 – Locally refining the mesh near the corners in simple beam model. The number of mesh elements on the blue edges are specified. 23

Figure 2-6 - Maximum von Mises stress induced by $50\mu m$ deflection of one end in a $500\mu m$ beam vs. the number of elements calculated in the FEA study by COMSOL. 24

Figure 2-7 from [21] - Mesh sensitivity study – Fiber stress at clamped section and tip displacements of 2D model against Theory of Elasticity predictions. 25

Figure 2-8 - The COMSOL model to simulate the mechanics of this device is a symmetric section of the device including a pair of legs and a section of the shuttle in the center. A cross-sectional view of this model in the x-y plane is further detailed in Figure 2-9. 26

Figure 2-9 - The revised model with no deformation in x-y plane. In this model, one pair of legs is modeled instead of one leg to avoid constraining the end of the beam to move only in one direction. 26

Figure 2-10 – Simulated equivalent stress using a non-locally-refined extra-fine mesh. Simulation parameters were: $BeamL = 500\ \mu m$, $BeamW = 20\ \mu m$, $BeamH = 10\ \mu m$, $SideW = 500\ \mu m$, $ShuttleW = 500\ \mu m$, $ShuttleL = 500\ \mu m$, $Fx = 0.1\ mN$ and $FilletR = 20\ \mu m$. 27

Figure 2-11 – Locally refining the mesh near the corners in device model. The number of mesh elements on the blue edges are specified. 27

Figure 2-12 - Mesh Sensitivity Tests of maximum von Mises stress vs. number of FEA elements from simulating the model in Figure 2-9 using nonlinear model, without (Figure 2-12a) and with (Figure 2-12b) fillets. Simulation parameters were: $BeamL = 500\ \mu m$, $BeamW = 20\ \mu m$, $BeamH = 10\ \mu m$, $SideW = 400\ \mu m$, $ShuttleW = 500\ \mu m$, $ShuttleL = 500\ \mu m$, $Fx = 0.1mN$ and (a)$FilletR = 0$ or (b)$FilletR = 0.5\ \mu m$. 28

Figure 2-13 – Mesh Sensitivity Study of the deflection induced by a fixed load force of 1e-4N shows clear sign of convergence, (a) without and (b) with fillets. Simulation parameters are: $BeamL = 500\ \mu m$, $BeamW = 20\ \mu m$, $BeamH = 10\ \mu m$, $SideW = 500\ \mu m$, $ShuttleW = 500\ \mu m$, $ShuttleL = 500\ \mu m$, and $FilletR = 0.5\ \mu m$. 28

Figure 2-14 – Simulation results of the deflection and maximum von Mises stress induced by a fixed load force, with variations of SideW, ShuttleW and ShuttleL from 50 µm to 650 µm. In each trial, only one parameter was swept while others were kept constant. Simulation parameters when unchanged were: $BeamL = 1500\ \mu m$, $BeamW = 20\ \mu m$, $BeamH = 10\ \mu m$, , $FilletR = 20\ \mu m$, $Fx = 0.1\ mN$, $SideW = 500\ \mu m$, $ShuttleW = 500\ \mu m$, $ShuttleL = 500\ \mu m$. 29

Figure 2-15 – Comparison of simulation results using linear and nonlinear equations. Simulation parameters are: $BeamL = 500\ \mu m$, $BeamW = 20\ \mu m$, $BeamH = 10\ \mu m$, $SideW = 500\ \mu m$, $ShuttleW = 500\ \mu m$, $ShuttleL = 500\ \mu m$, and $FilletR = 0.5\ \mu m$. 30

Figure 2-16 - Comparison of simulation results using linear and nonlinear equations. Simulation parameters are: $BeamL = 500\ \mu m$, $BeamW = 20\ \mu m$, $BeamH = 10\ \mu m$, $SideW = 500\ \mu m$, $ShuttleW = 500\ \mu m$, $ShuttleL = 500\ \mu m$, and $FilletR = 0.5\ \mu m$. 31

Figure 2-17 - Photo of one Gen 3 T-20 Device under microscope. The reflection of light shows that the top surface is not flat. 32

Figure 2-18 – Simulation results of stress vs. deflection using parameters of Gen 3 devices (as shown in Table 2-1): (a) T10 Devices and (b) T20 Devices. Simulation parameters are: $BeamH = 10\ \mu m$, $SideW = 500\ \mu m$, $ShuttleW = 500\ \mu m$, $ShuttleL = 500\ \mu m$, $FilletR = 0.5\ \mu m$, and (a) $BeamL = 300\ \mu m$, $BeamW = 10\ \mu m$; (b) $BeamL = 500\ \mu m$, $BeamW = 20\ \mu m$. 33

Figure 2-19 – Simulation results of deflection vs. load force using parameters of Gen 3 devices (as shown in Table 2-1): (a) T10 Devices and (b) T20 Devices. Simulation parameters are: $BeamH = 10\ \mu m$, $SideW = 500\ \mu m$, $ShuttleW = 500\ \mu m$, $ShuttleL = 500\ \mu m$, $FilletR = 0.5\ \mu m$, and (a) $BeamL = 300\ \mu m$, $BeamW = 10\ \mu m$; (b) $BeamL = 500\ \mu m$, $BeamW = 20\ \mu m$. 33

Figure 2-20 – Experiment setup for load force vs. deflection measurements. 34

Figure 2-21 – Gen 3 device design from [11]. (a) NH-type device head, with the head in the middle of the moveable shuttle structure. (b) OH-type device head at the opposite end of shuttle as the tip. 34

Figure 2-22 – A section of a microscopic picture of the device. The length of the leg BeamL and the separation between legs are both known values, and with no load weight the two segments are perpendicular by design. 35

Figure 2-23 – Measuring scheme of the deflection dx. CD is parallel to AB. AC and BD represent the edge of the shuttle and the frame connected by the legs, respectively, and are parallel by design. 35

Figure 2-24 – Measured deflection versus load force in Gen 3 T20 device with 58 pairs of legs and a comparison against simulation result. The load weight was applied in strictly increasing order for the data points in this plot. Simulation parameters: $BeamL = 500\ \mu m$, $BeamW = 20\ \mu m$, $BeamH = 10\ \mu m$, $SideW = 500\ \mu m$, $ShuttleW = 500\ \mu m$, $ShuttleL = 500\ \mu m$, and $FilletR = 0.5\ \mu m$. 36

Figure 2-25 – Electrical path in the device. 37

Figure 2-26 – Experiment setup for long-term impedance monitoring. 38

Figure 2-27 – Microscope image of the device in water. 39

Figure 2-28 – A typical measurement between two reference electrodes. 40

Figure 2-29 – Magnitude of impedance at 1 kHz over time measured with constant PBS level on device tip: full experiment. 41

Figure 2-30 - Magnitude of impedance at 1 kHz over time measured with constant PBS level on device tip: first 6 hours. 41

Figure 2-31 – Magnitudes and phases of the impedance at significant time points. 42

Figure 2-32 - Magnitude of impedance over time measured with constant DI level on the device shows a significant rise in the first few hours and then relatively stabilized. 43

Figure 2-33 – Microscopic picture of one of the test devices after 35h in DI water showed severe delamination on the tip. 44

Figure 3-1 – Gen 3 PS-T20 design schematics from [11]. 45

Figure 3-2 – Simulated maximum von Mises stress vs. fillet radius with fixed deflection amount. Simulation parameters: $BeamL = 1500\ \mu m$, $BeamW = 20\ \mu m$, $BeamH = 10\ \mu m$, $SideW = 500\ \mu m$, $ShuttleW = 500\ \mu m$, $ShuttleL = 500\ \mu m$, and $dx = 50\ \mu m$. 46

Figure 3-3 – Simulated maximum von Mises stress vs. leg width with fixed deflection amount. Simulation parameters:$BeamL = 1500\ \mu m$, $BeamH = 10\ \mu m$, $SideW = 500\ \mu m$, $ShuttleW = 500\ \mu m$, $ShuttleL = 500\ \mu m$, $FilletR = 20\ \mu m,$ and $dx = 50\ \mu m$. 46

Figure 3-4 – Simulated maximum von Mises stress vs. leg length with fixed deflection amount. Simulation parameters:$BeamW = 20\ \mu m$, $BeamH = 10\ \mu m$, $SideW = 500\ \mu m$, $ShuttleW = 500\ \mu m$, $ShuttleL = 500\ \mu m$, $FilletR = 20\ \mu m,$ and $dx = 50\ \mu m$. 47

Figure 3-5 – (a) Design of the device from [11] and (b) the metal traces that goes through the legs. 48

Figure 3-6 – Deflection vs. load force per pair of legs using chosen BeamL. Simulation parameters:$BeamW = 20\ \mu m$, $BeamH = 10\ \mu m$, $SideW = 500\ \mu m$, $ShuttleW = 500\ \mu m$, $ShuttleL = 500\ \mu m$, $FilletR = 20\ \mu m$. 50

Figure 3-7 – Leg separation. 51

Figure 3-8 – Gen 4 design revised from the Gen 3 devices. 52

Figure 3-9 – Design schematics for the test devices. 53

Figure 3-10 – Mask layout of variations of Gen 4 devices and the test devices. 54

Figure 3-11 – Fabrication process of the device. The side view on the right shows a cross-sectional view along the green dashed line of the corresponding top view on the left. 55

Figure 3-12 – Wafer with patterned devices after fully curing both PI layers. 57

Figure 3-13 – Wrinkles in the metal trace layer. 58

Figure 3-14 – Microscope images of the test device legs when there is no load weight attached vs. when there is load. 60

Figure 3-15 – Measured deflection vs. load force result in T1200 Device. 61

Figure 3-16 – Measured deflection vs. load force result in T1500 Device. 61

Figure 3-17 – Measured deflection vs. load force result in T2000 Device. 62

Figure 3-18 – Deflection of the legs in T2000 after load forces were removed. 63

Figure 3-19 – Distance shuttle travels when load force is removed. 64

Figure 3-20 – Experiment 1: impedance magnitude of Gen 4 Device 1 tip in PBS at 1 kHz over time for 23 h. 65

Figure 3-21 - Experiment 1: impedance magnitude of Gen 4 Device 1 tip in PBS at 1 kHz over time for 23 h: first 5 hours. 66

Figure 3-22 – Experiment 2: impedance magnitude of Gen 4 Device 1 tip in PBS at 1 kHz over time for 5 h, after rinsed in DI water and dried after Experiment 1. 67

Figure 3-23 - Experiment 3: impedance magnitude of Gen 4 Device 2 tip in PBS at 1 kHz over time for 48 h. 68

Figure 3-24 – Measured impedance magnitude of Gen 4 Device 2 tip in PBS at 1 kHz around the time of stirring of the PBS. 69

Chapter 1: Introduction

1.1 Background and Motivation

1.1.1 Neural Prosthetics and Common Recording Methods

Neural prosthetics aim at replacing or improving the performance of malfunctioning parts of the nervous system due to disease or trauma. Imagine a patient who lost an arm or a patient who cannot control his or her arm well due to a spinal cord injury. If we know how neural activities in the brain corresponds to the control of arm motions and hand gestures, we can develop a system that redirects the commands from the brain to the peripheral nervous system, or build a prosthetic arm that can be controlled directly using brain signals.

To understand how the neurons control our bodies, the ability to access and record their activities is essential. The recording of brain signals has been a fascinating realm of exploration since scientists learned that neurons communicate through electrochemical signals. Not only can the neural activities be read directly from voltage measurements in individual neurons, but also from the electrical field that such signals generate in the neurons' adjacent surroundings.

Currently, both non-invasive and invasive neural probes are used to record neural activities. Common non-invasive recording techniques include electroencephalogram (EEG) and Electrocorticography (ECoG), which record from outside the brain and maximally avoid tissue damage. Invasive neural electrodes, on the other hand, penetrate brain tissue and read from within the brain. The invasive electrodes have much higher spatial-temporal resolution compared to EEG or ECoG [1], and is less prone to ambience noise or disturbance caused by body movements of the test subjects wearing them, which are both desired traits of recordings used for neural prosthetic devices.

1.1.2 Challenges with Invasive Electrodes: Tissue Responses

Although invasive electrodes are capable of recording cleaner data with higher spatial-temporal resolution, their functional lifetime is a big challenge in their chronic usage. The implants often trigger tissue responses that deteriorates the signal quality over time [2]. The initial insertion of the devices into the brain causes inflammatory response of the tissue due to mechanical trauma [2]. However, while this initial inflammatory response goes away in a few weeks, the long-term responses by glial cells, in particular reactive Astrocyte and activated microglia, is more concerning [2]. In reaction to a neural electrode insertion, these electrically inactive glial cells in the brain tissue gradually forms a condensed sheath around the inserted foreign body in between 4 to 6 weeks, as shown in Figure 1-1 [2] [3]. The glial sheath likely shields the electrically active neurons from the electrode, thus prevents the electrode form recording neural signals.

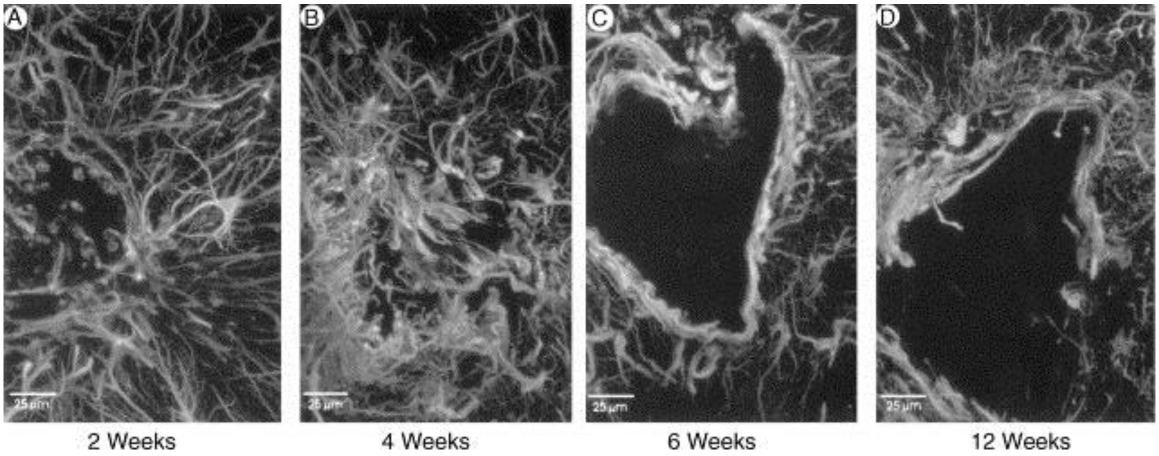

Figure 1-1 and caption adapted from [3] by [2]- Time course of glial scar formation at four time points as imaged by GFAP staining. At 2 and 4-week time points, the astrocytic processes fall back into the void left by the probe extraction before tissue processing. By 6 weeks, the processes have interwoven to form a stronger, more dense sheath surrounding the implant. Minimal changes between the 6- and 12-week time points indicate the glial scar completion within 6 weeks.

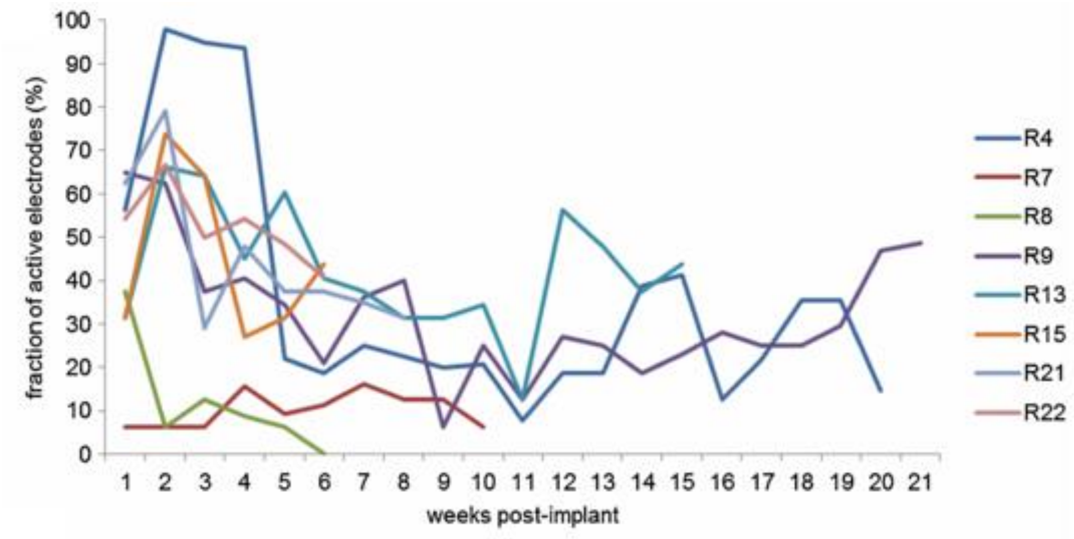

Figure 1-2 adapted from [4] - Aggregated data from eight chronic animals to show the trend of the weekly array yield for long-term microarray implants (≥6 weeks).

Previously, Prasad and Sanchez has performed a long-term study on the yield of active electrode over time after implantation using custom made microelectrode arrays [4]. Their results in Figure 1-2 shows that the fractions of active electrodes decrease after 2 to 3 weeks post-implantation in most implanted arrays. They attributed this decrease to the glial response.

This problem caused by the glial sheath formation suggests that brain implant surgeries need to be done frequently to replace the inactive probes with new ones in order to get reliable readings. This makes the long-term and large-scale use of such probes very inconvenient, if not impractical, for both doctors and patients. Therefore, one of the most critical challenges in invasive neural probe design is to lessen or avoid effect by long-term tissue responses.

1.1.3 Current Approaches to Reduce Effect by Tissue Responses

Currently, people have proposed various approaches to reduce tissue responses in the long-term, while others use repositioning probes to pierce through the formed glial sheath to reach fresh tissue.

1.1.3.1 Reducing Tissue Responses

Long-term tissue responses may be reduced by enhancing biocompatibility of the recording interface. Common ways to achieve biocompatibility are using biocompatible polymers or coating the implanted electrodes with highly biocompatible material. For example, a study by Rao et al. showed that Polyethylene glycol-containing polyurethane hydrogel coatings reduces the glial responses [5]. Immunohistochemistry performed after 6-week implantation in rat cortexes showed that the average thicknesses of the glial sheath were 35 µm around uncoated electrodes and 22 µm around coated ones.

Making the electrodes smaller can also lower negative effect from tissue responses. Ultra-small implants have been proven to cause significantly less glial sheath formation. Seymour and Kipke demonstrated that their design of a parylene 5-µm thick lateral structure caused significantly lower level of tissue responses and neuron loss than a 48-µm-by-68-µm shank with the same parylene surface 4 week post implantation [6]. Kozai et al. have proposed and tested an ultrasmall microthread electrode designs with a total diameter of 8.5-µm, and demonstrated that these electrodes were able to record single-unit neural signals for at least 5 weeks with a high yield and had no sign of degradation over the moderate period of time [7]. These studies suggests that electrodes with subcellular-geometry are be able to reduce tissue responses and are feasible for single-unit neural recordings.

Another approach is to use flexible material to make the electrodes. Lee et al. performed a study using neural probes made from silicon (~150 GPa), polyimide (1.5 GPa), OSTE+$_{\text{Hard}}$ (300 MPa), and OSTE+$_{\text{Soft}}$ (6 MPa) with comparable small thickness (15-µm silicon probe and 22-µm polymer probes) were implanted in adult mice [8]. The tissue responses were studied 4 and 8 weeks post implantation by performing a quantitative study of different inflammatory biomarkers around the site of implant. Results confirmed that flexibility is one key to reducing the tissue responses, since the silicon probes induced the most severe responses. However, results from the three softer polymer probes showed no significant difference, suggesting that beyond some threshold, further increasing the flexibility could not provide further help.

1.1.3.2 Repositioning Probes

While the mechanism of how to further lower or avoid tissue reaction is still under study, people have been using the technique of repositioning probes to prolong the functional lifetime of the neural implants. When the tissue reaction and SNR decrease, the electrodes get pushed further inside to pierce through the glial scars to get cleaner readings. For example, Jackson et al. designed a MEMS based device to push electrodes of size 50 µm × 4 µm × 5 mm forward when the SNR decreases to a level where signal and noise were undistinguishable [9]. The electrodes were implanted in rat somatosensory cortex, and each time the electrode was repositioned, the SNR stayed high enough for 2-4 days. Nevertheless, this is not an ultimate solution for chronic usage since after a certain number of repositions the electrodes will be pushed too far away to record from the target neurons.

Another study by Stice and Muthuswamy provided evidence that later repositioning of the electrodes causes less response than the initial insertion if repositioned after the initial healing process [10]. In the study, they performed a quantitative assessments of glial fibrillary acidic protein (GFAP) around the microeletrodes with a diameter of 114 µm implanted in rat cortex repositioned at different times. The electrodes were repositioned 2 days, 14 days, and 28 days post-implantation, and histology was performed 4 weeks post-movement, with control groups in which the electrodes were not repositioned. Results showed that although the level of GFAP expression was not significantly different between the control group and that moved 2 days post-implantation, the groups repositioned 14 and 28 days post-implantation showed much lower GFAP around the tip of the electrodes.

1.1.4 Our Approach: Reconfigurable MEMS Neural Probe

1.1.4.1 Device Design

Our approach utilizes a combination of the previously introduced methods: biocompatibility, small size, flexibility to reduce tissue response, and with repositioning feature. Previously, A. Dighe has proposed and tested a MEMS-based design that used biocompatible and highly flexible polyimide (PI) with tip thickness of about 10 µm [11]. The recording electrode was in the form of a gold trace, which was mostly covered in between the two PI layers, while one of the PI layers had a small opening on the tip of the device to allow exposure of the trace to the brain tissue. The repositioning operation schematics of the device is shown in Figure 1-3. This thesis will be based on his work.

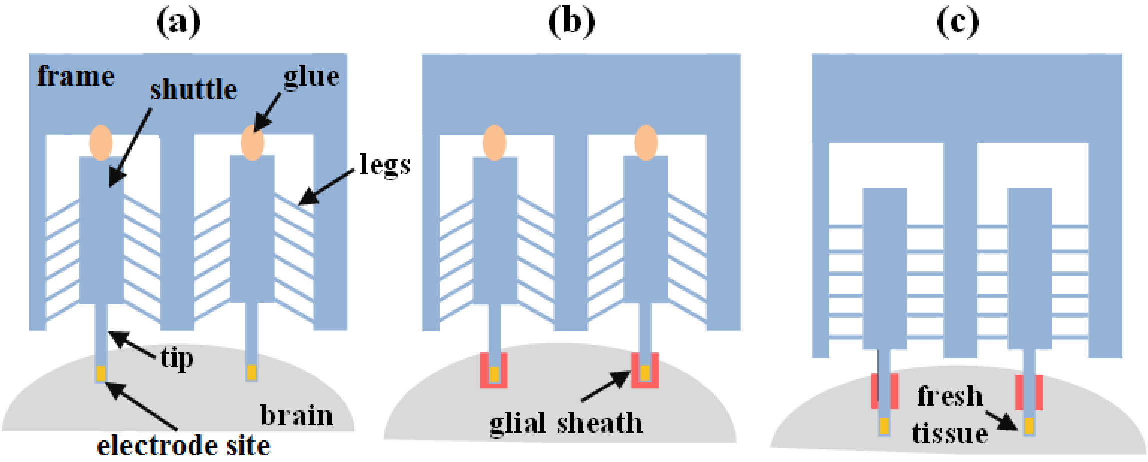

Figure 1-3 adapted from [11] - Device operation schematic by A. Dighe.

Figure 1-3 shows the MEMS device that consists of a shuttle that supports the tip with electrode sites, an outer frame, and thin legs that connects the shuttle to the frame. Prior to insertion, the shuttle is pulled and glued to the outer frame, as shown in (a). Since polyimide is highly flexible, the deflected thin legs act as springs to store mechanical energy. In (b), after the implant surgery, tissue reaction takes place and a glial sheath forms around the probe tip. This initial healing process is expected to take about a few weeks. Then, the glue holding the shuttle back gets dissolved, and the energy stored in the deflected legs helps push the shuttle forward and releases the probe tip to fresh tissue, as shown in (c).

The test of the design started with Gen 0, in which the mechanical feasibility of the leg-spring design was verified. Benchtop buckling tests of the tip was performed to ensure that the geometry of the tip was able to pierce through brain tissue. In Gen 1, the electrode traces were added, and the design of the legs was improved based on test results of Gen 0 devices. Gen 2 and Gen 3 further modified the design based on test results of their previous generations, and in Gen 3, a resistive heater mechanism was added to enable remote control of the shuttle deployment. The resistive heater mechanism was verified in benchtop *in vitro* setup.

1.1.4.2 Known Issues from *In Vivo* Studies and Proposed Hypotheses

The latest generation of the design, Gen 3, was used in both acute *in vivo* studies in optogenetic mice and preliminary chronic *in vivo* study in rats. The acute study showed high SNR of recorded neural signal in some electrodes, which proved the recording functionality of the devices. However, the recording was not reliable in all electrode sites. In the chronic study in which the device shuttles were initially pulled back during implantation, the devices failed to deploy after 5-weeks.

Mechanical failure of the legs was suspected — whether the force the legs could deliver was enough to pierce through the glial sheath, and whether the stress was too high to cause plastic instead of elastic deformation. Another hypothesis of the unsuccessful deployment was due to the failure of the resistive heater, as the impedance of the heater was measured to be open circuit after 5-weeks.

Besides the unsuccessful shuttle deployment, another especially concerning observation from the *in vivo* study was the significant decrease in measured impedance of the electrode sites.

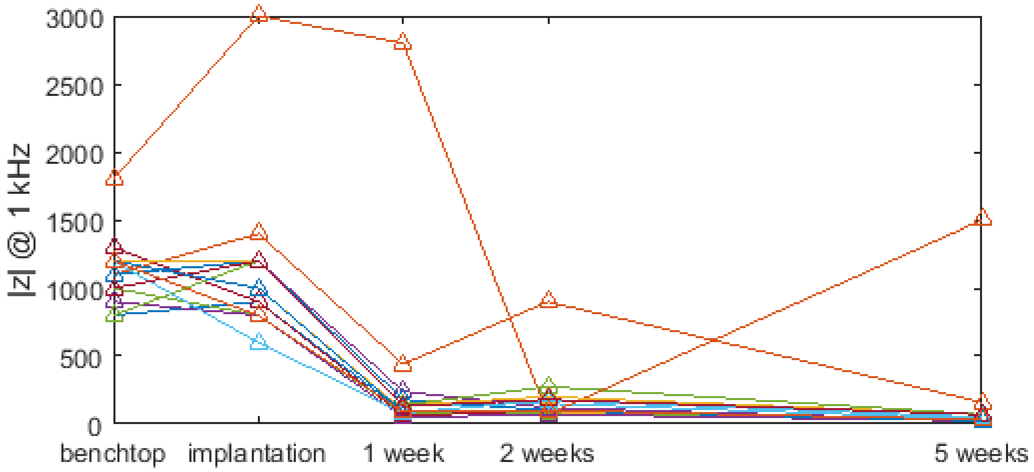

Figure 1-4 – Magnitudes of the impedances of the 16 electrode sites measured in benchtop tests pre-implantation, immediately post-implantation, and 1, 2, 5 weeks post-implantation using data from [11].

The impedance of the electrode sites at 1 kHz was measured in benchtop tests pre-implantation, immediately post-implantation, and 1, 2, 5 weeks post-implantation. As shown in Figure 1-4, for 14 out of the 16 implanted electrode sites, the impedances dropped dramatically during the first week after implantation.

The cause of the heater failure and impedance decrease was hypothesized to be the delamination of the two PI layers of the device. Water absorption causing adhesion loss has been a known issue for PI [12]. Thus if the adhesion between the two layers were not initially strong enough, submerging in a high moisture environment could have decreased the adhesion further, even breaking the bonding to cause delamination. That means there was a gap in between the layers, exposing more of the electrode traces than designed to the brain tissue environment. If the delamination happened rather fast after the implantation, it could also have contributed to the inability to record neural signals reliably in the acute *in vivo* experiment.

1.2 Thesis Overview

Therefore, the main goal of this thesis will be to test the remaining Gen 3 devices and produce an improved design based on the test results and resulting hypotheses.

Chapter 2 includes mechanical and electrical characterizations of the Gen 3 devices. The original analytical model used for mechanical design was re-examined, and simulations were used to verify the choice of design parameters. Then the simulation model will be compared to actual measurement results. The impedance of the electrode sites were recorded over prolonged time to verify if any changes would take place in *in vitro* settings.

In Chapter 3, using the results in Chapter 2, modifications were made to the mechanical parts of the design and to the fabrication process of the devices. This new generation, Gen 4, will be tested again for their mechanical and electrical properties to see whether the design or fabrication process has been improved.

Chapter 4 will include discussions on what contributions this work has made during its process, and future directions for those who might later take on this work.

Chapter 2: Gen 3 Device Characterization

2.1 Introduction

As introduced in Chapter 1, the shuttle deployment failure 5 weeks post implantation using Gen 3 devices in *in vivo* environment let us suspect both mechanical failure of the device legs and electrical failure caused by delamination.

In this chapter, the original mechanical model of the stresses induced by a certain leg deflection and the corresponding load forces required to provide such a deflection will be reviewed. Since an analytical linear model was used for the design of previous generations, nonlinear model will be used with the help of FEA simulation software to provide a better characterization of the mechanism.

On the electrical aspect, the impedance of the electrode sites will be recorded in an *in vitro* setting to see whether the decreased observed in *in vivo* setting can be replicated. The impedance will be recorded at short intervals for a prolonged time to determine if and how it decreases to potentially provide more insights into the causes; in particular, whether they are consistent with the delamination hypothesis.

2.2 Gen 3 Mechanical Analysis

In the assembly of the device packaging, the outer edge of the frame is glued to a holding glass slide, while the shuttle is not directly attached to the slide. Prior to implant surgery, the device shuttle is pulled and glued to the frame on one end. Since the device is made from Polyimide, which is highly flexible, when the stress induced in the legs by the deflection is below the elastic yield of Polyimide, the set of legs acts like a spring. When the load force is released by melting the glue, the reaction force will drive the shuttle in the opposite x-direction until legs are straight again.

In this design, three criteria are essential: the deflection of the legs, the force this spring provides when released, and the maximum induced stress. The deflection of the legs should be greater than the thickness of the glial sheath (estimated to be 5 µm [11]) to reach unblocked tissue. The force the spring provides while restoring its shape at rest should be strong enough to pierce through the glial sheath (estimated to be 5 mN [11]). The maximum induced stress should be lower than the elastic yield stress (70 MPa [11]) of Polyimide to make sure that the structure remains undamaged and able to restore its original shape. The last one is critical in that it makes sure that the deflection of the legs while held by glue is the same as the distance the shuttle travels when released, and that the reaction force can be predicted assuming elasticity of the material.

In the *in vivo* tests of Gen 3 devices, some devices failed to deploy when the glue is melted [11]. One of the potential reasons was mechanical failure, that the device tip failed to provide enough force or distance to pierce through some of the glial sheath. In choosing the design paramters for Gen 3, the mechanical properties were modeled using the linear model of beam deflection, and large safety factors were introduced in the predictions to account for the simplification of the mechanism. These mechanical properties, however, were not tested thoroughly in the devices.

This section re-examines the original mechanical model of the device to see whether the safety factors used were large enough to cover the simplifications by the model as well as other factors due to fabrication variations.

2.2.1 Re-Visiting the Original Linear Analytic Model

2.2.1.1 Model of the Deflected Device Legs as a Fixed-Fixed Beam

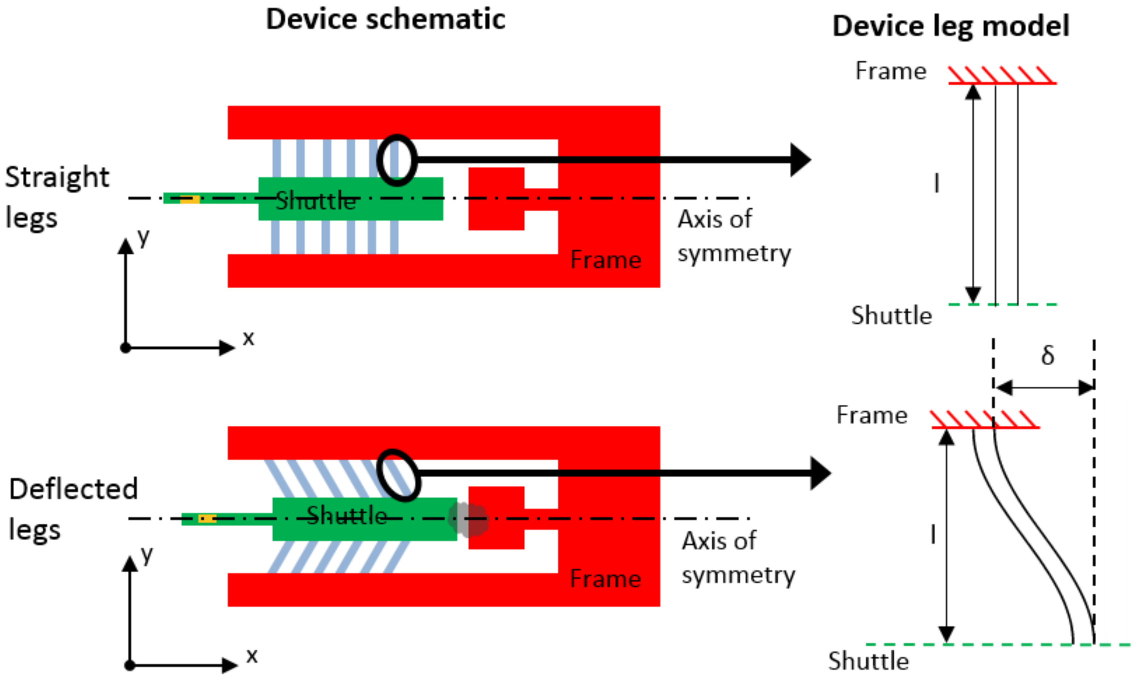

Figure 2-1 – Model of the device leg in the x-y plane. Figure adapted from [11].

Figure 6 shows the view of the device mechanism in the x-y plane. The device has uniform height in the z direction perpendicular to the x-y plane. All movements and deflections of the device are designed to occur only in the x-y plane.

Since the legs are very thin beams made from highly flexible material, the legs can be viewed as highly elastic. The shuttle and the frame, on the other hand, have relatively very large span at any point in all directions in the x-y plane, and thus can be approximated as rigid bodies when discussing movements and deflections in this plane. When a load force (by hand or by glue) is applied at one end of the shuttle along the axis of symmetry of the structure, the legs will deflect accordingly, allowing the shuttle to move in the same direction as the force, as shown in Figure 2-1.

Each device leg can be modeled as a beam with a uniform rectangular cross-section, and all legs are identical by design. The end of the beam connected to the frame can be modeled as a fixed support, while the end connected to the shuttle is allowed to move only in the x-directions. The distance of the frame from the shuttle is kept at l, which is the length of the original undeflected leg. The deflection δ is measured by the distance the end connected to the shuttle moves.

Due to the symmetry of this setup and the approximation of the shuttle as rigid body, the model in Figure 2-1 can be transformed into the model in Figure 2-2 by mirroring the beam with respect to the shuttle end (green dashed line).

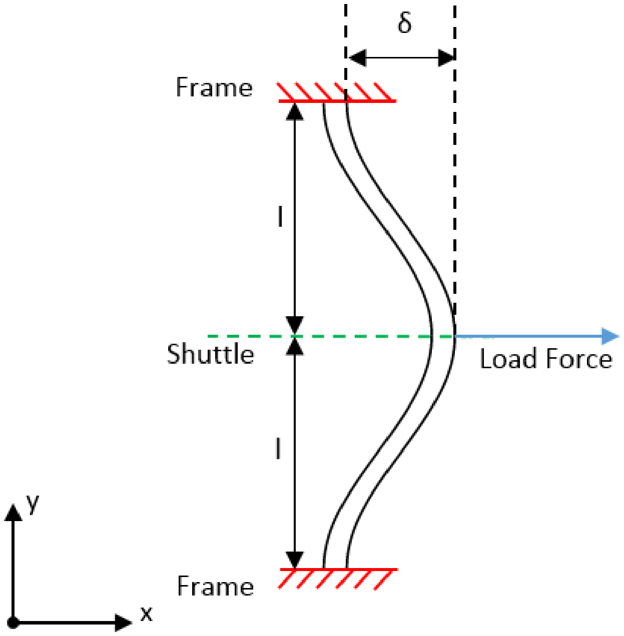

Figure 2-2 – Model of a pair of leg, adapted from [11].

The revised model in Figure 2-2 models a pair of legs at both sides of the shuttle, since all legs are identical by design. The load force is applied to the connection point of the beams along the green dashed line, which is now the axis of symmetry. The constraint that the shuttle end of the beam only moves in x-directions in the previous model in Figure 2-1 is now by default due to the symmetry.

And since all legs are identical by design, we can model only one pair of the legs to predict the amount of deflection and stress induced by load forces. The deflection and maximum stress induced in all legs are the same as those in one pair of legs, and the total load force equals the load force on one pair of legs times the total number of pairs.

2.2.1.2 Deflection vs. Load Force in a Fixed-Fixed Beam

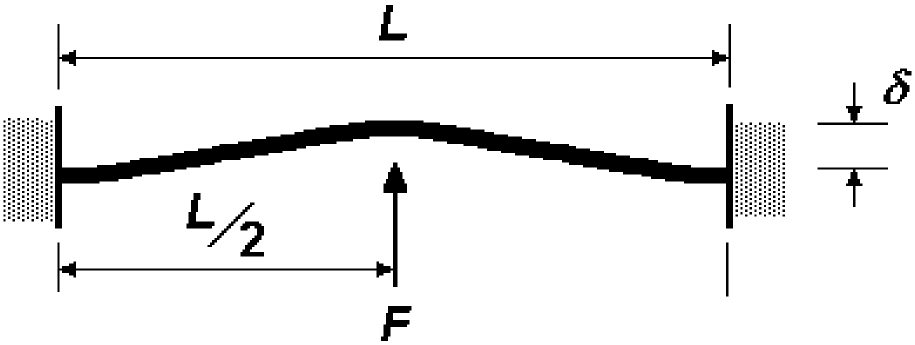

Figure 2-3 – Center load on beam with two fixed supports. Figure from [13].

Figure 2-3 and Equation 2-1 are adapted from figures and equations contained in *Mechanics of Materials (Fourth SI edition)* by J. M. Gere, S. P. Timoshenko and Stanley Thornes [13]. A beam with span L is fixed on both ends, and a load force F is applied at the center of the beam in a direction perpendicular to the beam at rest. The maximum deflection δ, occurring at the center of the beam, is given by [13]

$$\delta = \frac{FL^3}{192EI}, \qquad \text{Equation 2-1}$$

Where F is the load force and L is the total original span of the beam as shown in Figure 2-3, E is the Young's Modulus of the material, and I is the area moment of inertia of the beam's cross section.

This model in Figure 2-3 is the same as our model of one pair of legs in Figure 2-2, with the only difference being the notation of $\mathrm{l} = \frac{\mathrm{L}}{2}$, or equivalently $\mathrm{L} = 2\mathrm{l}$.

In our device leg model, the neutral axis of the beam is along the direction of the height of the beam h in the z-direction, and the cross-sectional area is a rectangle with uniformly distributed mass, so [14]

$$\mathrm{I} = \frac{b^3h}{12}. \qquad \text{Equation 2-2}$$

Combining with Equations 2-1 and 2-2, we have

$$\delta = \frac{F(2l)^3}{192E\frac{b^3h}{12}} = \frac{l^3}{2Eb^3h}F, \qquad \text{Equation 2-3}$$

Where F is the load force on each pair of leg. Equivalently

$$F = \frac{2Eb^3h}{l^3}\delta. \qquad \text{Equation 2-4}$$

Equation 2-4 here is consistent with the result given by Equation 2-5 in Dighe's [11]. The factor of two discrepancy is because the F in Dighe's is load force per leg, while here is load per pair of legs.

According to Newton's Third Law, the reaction force at the center point of this beam when the load force F is released has equal magnitude but opposite direction as F. So the force the device tip, which is connected to the shuttle, provides when the glue is released can be approximated using Equation 2-4.

2.2.1.3 Stress vs. Load Force in a Fixed-Fixed Beam

In the same setting has above in *Figure 2-3*, we can calculate the maximum stress induced at the load and both ends using [15]

$$\sigma_{max} = \frac{FL}{8Z}, \qquad \text{Equation 2-5}$$

Where Z is section modulus of the beam, [16]

$$\mathrm{Z} = \frac{b^2h}{6}. \qquad \text{Equation 2-6}$$

This gives

$$\sigma_{max} = \frac{FL}{8\frac{b^2h}{6}} = \frac{3FL}{4b^2h}\,. \qquad \text{Equation 2-7}$$

Substituting Equation 2-4, we get

$$\sigma_{max} = \frac{3\frac{2Eb^3h}{l^3}\delta(2l)}{4b^2h} = \frac{3Eb}{l^2}\,\delta\,. \qquad \text{Equation 2-8}$$

Which is also consistent with Equation 2-6 in Dighe’s.

2.2.2 Limitations of the Original Linear Model

These linear equations, however, are no longer appropriate approximations of the mechanical system once the deflection is large comparative to the span.

Table 2-1 – Device specifications of Gen 3 devices.

Device Type	Beam Length [µm]	Min. Target Deflection [µm]	Min. % of Span	Max. Target Deflection [µm]	Max. % of Span
T10	300	50	16.67%	80	26.67%
T20	500	50	10.00%	80	16.00%

The lengths of the legs in Gen3 devices were either 300 µm or 500 µm, while the target deflection range was 50µm to 80µm. This means the target deflection range has been greater than 10% of the length of the beams, which should no longer be considered *small deflection* settings. Thus, nonlinear models should be used to get a better approximation of the system.

2.2.3 FEA Simulation Model

2.2.3.1 FEA Simulation Software

Since solutions using nonlinear models are not easily calculated analytically, *COMSOL Multiphysics 4.2* was used to perform 3-D Finite Element Analysis (FEA) of the system. The linear elastic materials model under Structural Mechanics Module was used, and geometric nonlinearity for large deformations was included.

Table 2-2 – Equations used in COMSOL linear elastic materials model [17]

Not including geometric nonlinearity	Including geometric nonlinearity
$-\nabla \cdot \sigma = \mathbf{F}\upsilon,\ \sigma = \boldsymbol{S}$ $\boldsymbol{S} - \boldsymbol{S}_0 = \mathbb{C} : (\varepsilon - \alpha(T - T_{\mathrm{ref}}) - \varepsilon_0)$ $\varepsilon = \frac{1}{2}[(\nabla \mathbf{u})^{\mathrm{T}} + \nabla \mathbf{u}]$	$-\nabla \cdot \sigma = \mathbf{F}\upsilon,\ \sigma = \left(\boldsymbol{S} \cdot (\mathbf{I} + \nabla \mathbf{u})\right)$ $\boldsymbol{S} - \boldsymbol{S}_0 = \mathbb{C} : (\varepsilon - \alpha(T - T_{\mathrm{ref}}) - \varepsilon_0)$ $\varepsilon = \frac{1}{2}[(\nabla \mathbf{u})^{\mathrm{T}} + \nabla \mathbf{u} + (\nabla \mathbf{u})^{\mathrm{T}} \nabla \mathbf{u}]$
σ - symmetric stress tensor **F** - loads υ - Poisson’s ratio $\boldsymbol{s}$ - stress tensor, $\boldsymbol{S}_0$ - initial stresses **I** - identity matrix $\nabla \mathbf{u}$ - displacement gradient $\mathbb{C}$ - 4th order elasticity tensor $:$ - double-dot tensor product (or double contraction) ε - strain tensor, ε_0 - initial strains α - thermal expansion tensor T - temperature, T_{ref} – reference temperature	

2.2.3.2 Material Properties

The material properties of Polyimide HD-4100 from HD MicroSystems™ used in the simulations are listed in Table 2-3.

Table 2-3 – Material Properties of Polyimide

Material Property Name	Value	Unit
Young's Modulus [18]	3.3	GPa
Density [19]	1430	kg/m3
Poisson's ratio [19]	0.33	(unitless)

2.2.3.3 Equivalent Stress

In the simple modeling used for previous generations, *only stress induced by bending moments was explicitly calculated*. Previously, Dighe performed an analysis that showed the significant impact on the total stress by stretching, and concluded that the effect could be taken account for by including a safety factor [11]. For this new generation of devices, we use the equivalent tensile stress, or von Mises stress, to compare to the approximated yield stress of the material, which is a commonly used approach in engineering design [20].

2.2.3.4 Stress Concentrations vs. Stress Singularities

One particular issues that needs to be dealt with carefully while using FEA to solve for stress is the occurrence of stress singularities in the solutions. In steady-state simulations, if the model is set up correctly, the solution should converge to a specific value as finer spatial discretization is used, which is known as a mesh sensitivity study [21]. But sometimes due to the unrealistic geometric elements (such as perfectly sharp corners) and constraints in simplified models used for simulation, the solutions at certain points will not converge and go to infinity instead. This is caused by the non-differentiability of the non-linear functions due to the geometry or the constraints. To demonstrate, we set up the following simple model of a device leg in Figure 2-4 with one end fixed and the other constrained to move freely only in the x-direction.

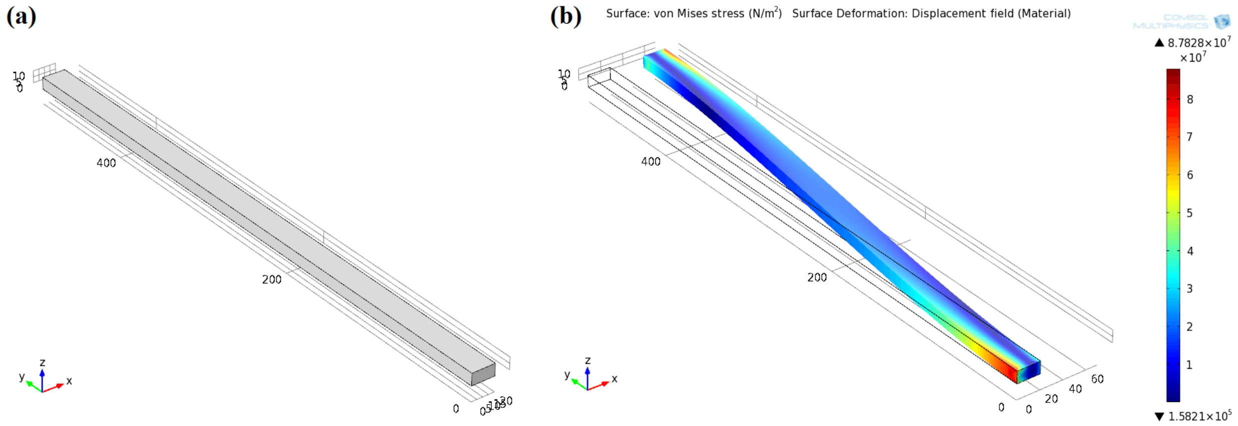

Figure 2-4 – (a) The simple model of the leg using a beam with rectangular cross-section. (b) An example surface plot of the FEA result of von Mises stress on the deformed beam using a mesh of 2305 elements. Beam length (z-direction) l = $500\mu m$, width (x-direction) b = $20\mu m$, and height (z-direction) h = $10\mu m$.

The surface plot of von Mises stress by using a simple mesh in Figure 2-4 suggests that the stress concentrations or singularities are in the corners, as expected. Therefore, the mesh and increase the number of FEA elements by locally refining the mesh near the corners. This was achieved by defining the mesh distribution by fixed numbers of mesh elements on all four edges in z-directions and constraining the growth rate of elements to a fixed value (here 1.35 was used).

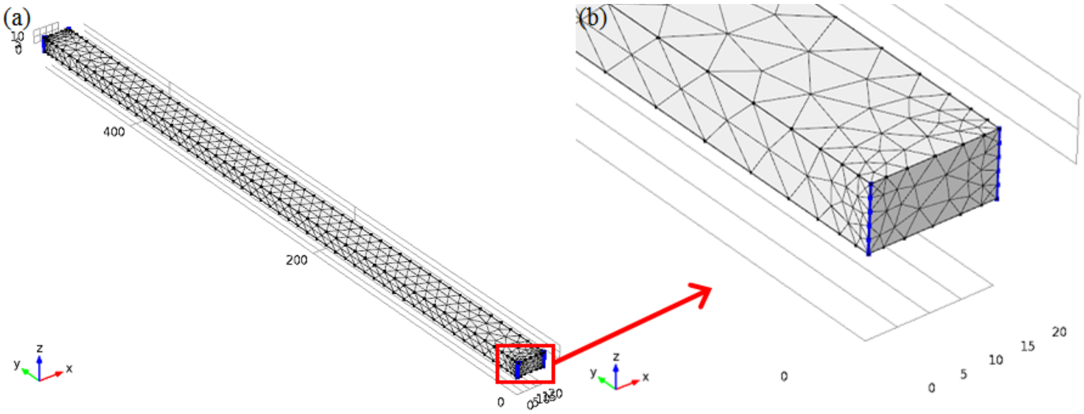

Figure 2-5 – Locally refining the mesh near the corners in simple beam model. The number of mesh elements on the blue edges are specified.

Table 2-4 - # of mesh elements used with the model in Figure 2-4 and the corresponding total number of elements

# of elements on edges in z-direction	# total elements
5	3002
10	5117
15	7863
20	9822
25	12527
30	14888
35	17357
40	20170

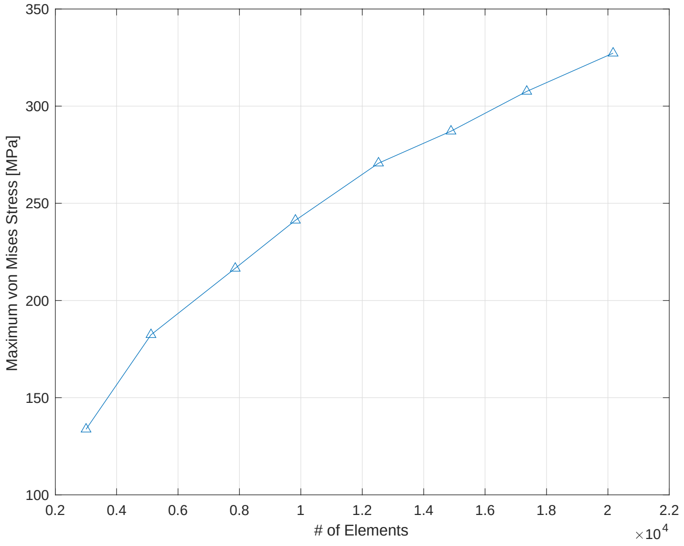

Figure 2-6 - Maximum von Mises stress induced by $50\mu m$ deflection of one end in a $500\mu m$ beam vs. the number of elements calculated in the FEA study by COMSOL.

As shown in Figure 2-6, the increasing maximum stress versus number of elements does not approach a limiting value over the tested range, which is consistent with a stress singularity at the corners (see Figure 2-4b), rather than stress concentrations.

This phenomenon has been thoroughly studied in similar settings. For example, M. Acin performed a mesh sensitivity test on a 2-D cantilever beam with one end fixed and shear force applied on the other end [21].

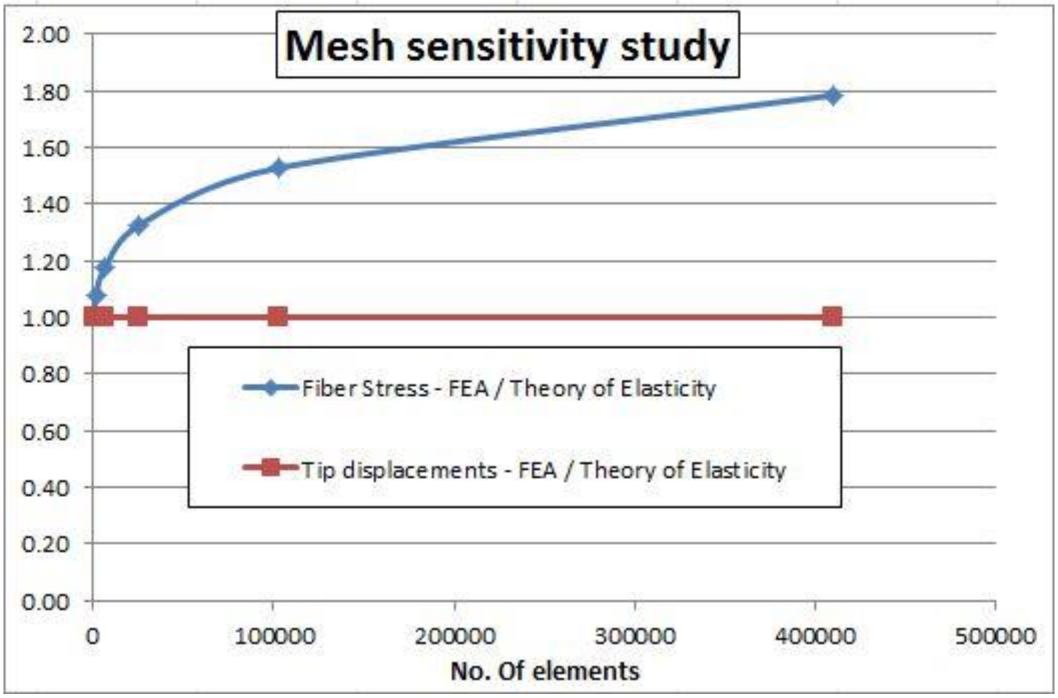

Figure 2-7 from [21] - Mesh sensitivity study – Fiber stress at clamped section and tip displacements of 2D model against Theory of Elasticity predictions.

This study showed that the stresses at the corners do not converge even with more than 400,000 elements, which means the elements were less than 0.04% of the beam length that Acin used in this simulation [21]. This singularity is due to the conflict of the Poisson's ratio effects and the fixed constraints. Furthermore, as Acin pointed out, Tullini, N. and Savoia, M. has performed a mathematical analysis of this setting and found that this singularity is of a logarithmic type [22]. Although our setting is not identical to the one in our study of a beam fixed at both ends instead of one, and we are using non-linear equations instead of linear ones, the same Young's Modulus and Poisson's ratio method were used, so the conflict between stress and displacement boundary constraints cannot be avoided.

The same study by Acin suggests that if we do not care about the stress solutions at or close to the singularities, they can be ignored. In our case, however, we would expect the maximum stress to be at the corners, where the singularities occur if not dealt with carefully, and we want to make sure that concentration does not exceed the yield stress. Therefore, the singularities at these corners needs to be removed. In setting up the model, we should maximally avoid unnecessary constraints near these corners. Since sharp reentrant corners and point loads are also known causes of stress singularities in FEA studies involving partial differential equations, these elements should be avoided as well [23].

2.2.3.5 Revised Simulation Model Setup

A new model was built to avoid causes of stress singularities such as conflicting boundary constraints, sharp reentrant corners and point or edge loads.

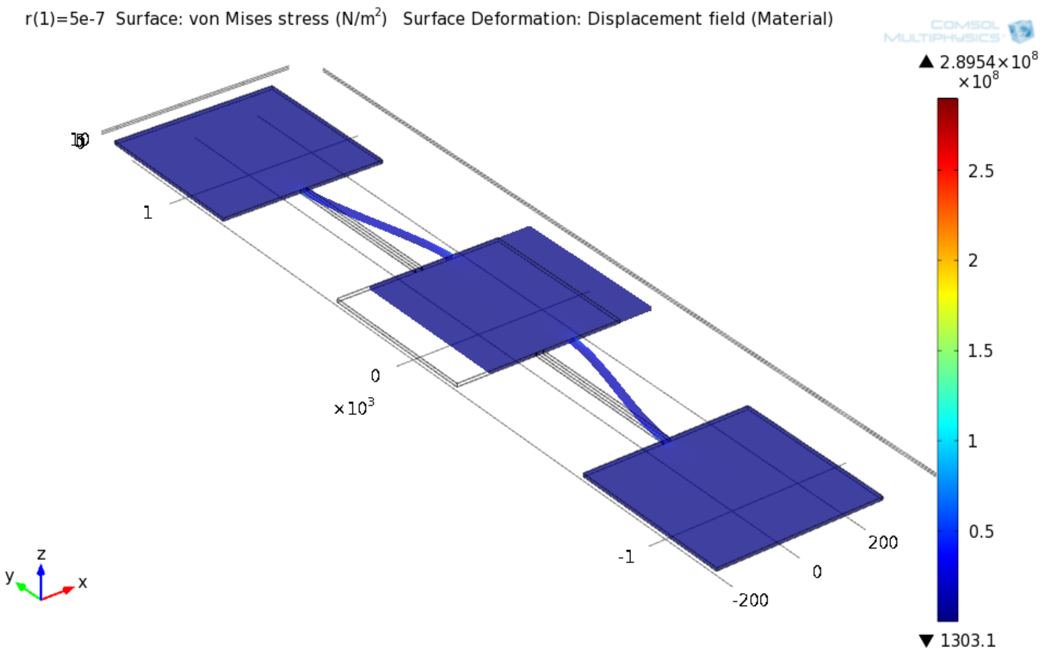

Figure 2-8 - The COMSOL model to simulate the mechanics of this device is a symmetric section of the device including a pair of legs and a section of the shuttle in the center. A cross-sectional view of this model in the x-y plane is further detailed in Figure 2-9.

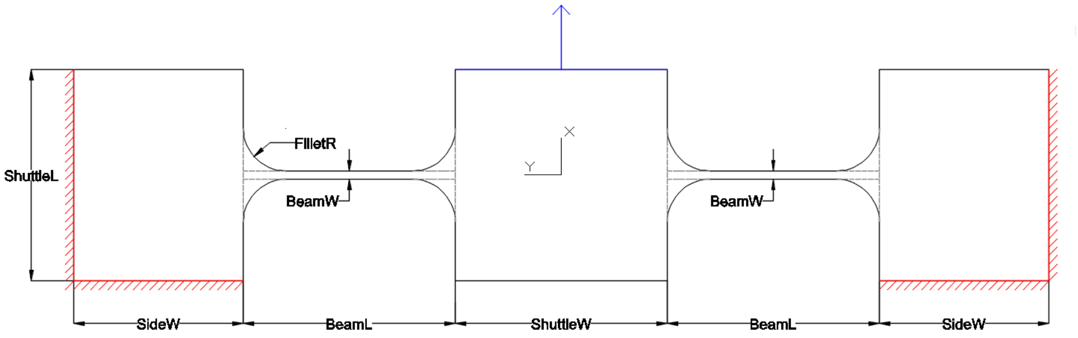

Figure 2-9 - The revised model with no deformation in x-y plane. In this model, one pair of legs is modeled instead of one leg to avoid constraining the end of the beam to move only in one direction.

The left and right panels are the frame of the device. These panels are added to keep the fixed displacement constrains far away from the ends of the beams.

The center panel is the device shuttle. It is added to avoid an edge load in z-direction, which is unrealistic in 3-D and is expected to pause a singularity just like a point load in 2-D.

Thin rectangular beams connecting the panels are the device legs.

Fillets in the shape of 90-degree arcs are added at the reentrant corners of the structure to make sure of the differentiability of equations at the corners. They should also help reduce the level of stress concentrations. The inclusion of fillets is well supported by the fact that the optics used to manufacture the photomask of the device has a $0.5\mu m$ radius, making a square of $1\mu m$ side length rounded circle, as stated on the manufacturer's website [24].

Fixed constraints are applied to the edges shown in red, while an edge load Fx or a fixed displacement dx in the x-direction is applied on the edge shown in green. Due to the symmetry of this structure, we do not need to put further constraints on the system to make sure the shuttle moves only in x-directions.

2.2.3.6 The Effect of Fillets

Mesh sensitivity tests were performed using the new model without (FilletR = 0) and with the fillets in the reentrant corners using a similar process as described in Section 2.2.3.4.

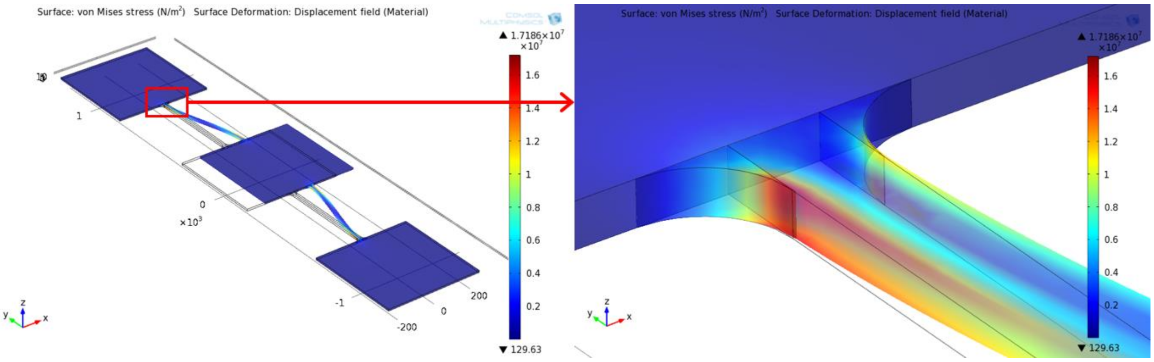

Figure 2-10 – Simulated equivalent stress using a non-locally-refined extra-fine mesh.
Simulation parameters were: $BeamL = 500\ \mu m$, $BeamW = 20\ \mu m$, $BeamH = 10\ \mu m$, $SideW = 500\ \mu m$, $ShuttleW = 500\ \mu m$, $ShuttleL = 500\ \mu m$, $Fx = 0.1\ mN$ and $FilletR = 20\ \mu m$.

A look at simulated equivalent stress using a non-locally refined mesh shown in Figure 2-10 suggested that the stress concentration is indeed near the corners. Therefore, instead of globally refining the mesh, again local refinement was used. The number of mesh elements is defined on each of the 8 edges in the z-direction in the reentrant corners when there is no fillet, as well as on the 16 edges at the intersection of the fillets and the beams/panels when the filter is added. Other meshing parameters were the same as in Section 2.2.3.4.

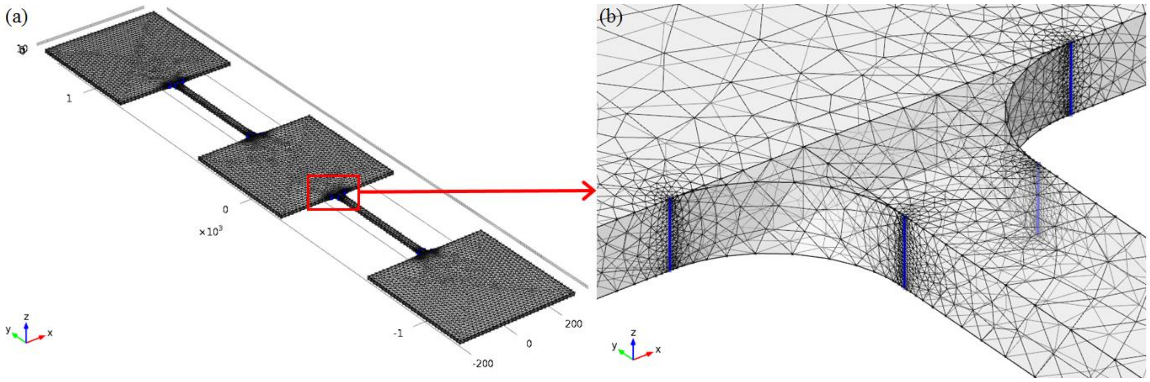

Figure 2-11 – Locally refining the mesh near the corners in device model. The number of mesh elements on the blue edges are specified.

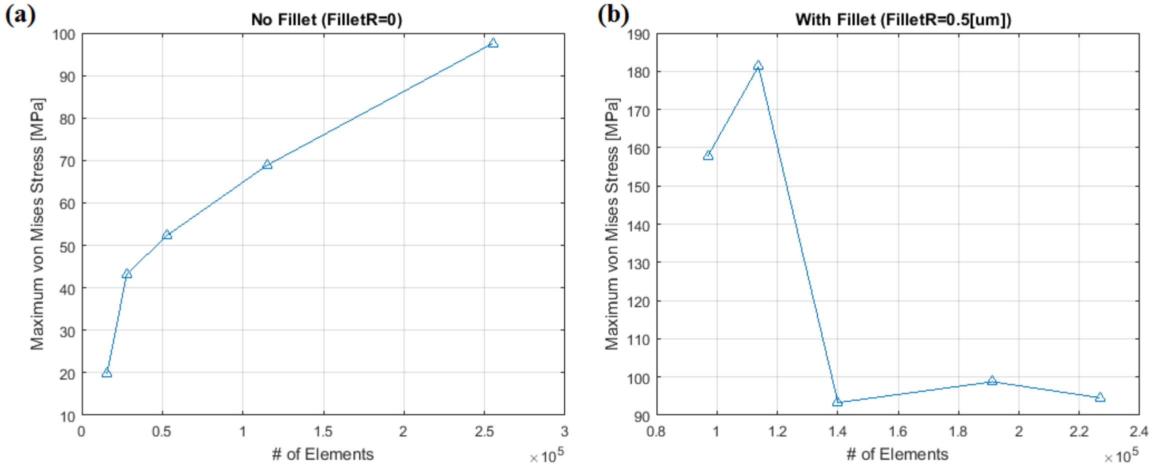

Figure 2-12 - Mesh Sensitivity Tests of maximum von Mises stress vs. number of FEA elements from simulating the model in Figure 2-9 using nonlinear model, without (Figure 2-12a) and with (Figure 2-12b) fillets.
Simulation parameters were: $BeamL = 500\ \mu m$, $BeamW = 20\ \mu m$, $BeamH = 10\ \mu m$, $SideW = 400\ \mu m$, $ShuttleW = 500\ \mu m$, $ShuttleL = 500\ \mu m$, $Fx = 0.1 mN$ and (a)$FilletR = 0$ or (b)$FilletR = 0.5\ \mu m$.

Results of stress induced by a fixed deflection in Figure 2-12 confirm that adding fillets in these reentrant corners is indeed essential to avoiding stress singularities. The maximum equivalent stress in (a) without fillets shows no sign of convergence with increasing number of elements if using the model without fillets, but stabilizes in the range of 90 to 100MPa when small fillets were added in (b).

As a confirmation of that stress singularities do not affect force versus deflection results [21], mesh sensitivity studies were also performed with a fixed load force on the shuttle.

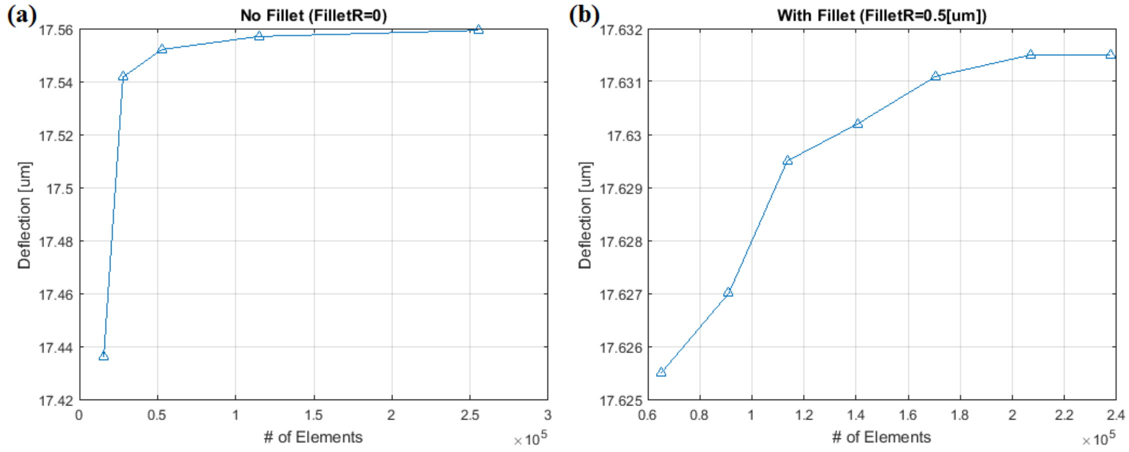

Figure 2-13 – Mesh Sensitivity Study of the deflection induced by a fixed load force of 1e-4N shows clear sign of convergence, (a) without and (b) with fillets.
Simulation parameters are: $BeamL = 500\ \mu m$, $BeamW = 20\ \mu m$, $BeamH = 10\ \mu m$, $SideW = 500\ \mu m$, $ShuttleW = 500\ \mu m$, $ShuttleL = 500\ \mu m$, and $FilletR = 0.5\ \mu m$.

As shown in Figure 2-13, when studying the load force versus deflection relationship, singularities did not occur in the simulation model, with or without the addition of fillets in the corners.

Unless specifically noted, all remaining simulations presented in this thesis used meshes refined in the same way as in Figure 2-11, and results were recorded when further refining the mesh did not significantly change their values.

2.2.3.7 The Effect of Added Panels

The effects different parameters of the three panels on the simulated deflection and maximum von Mises stress results were studied. The widths of the three panels were swept from 50 µm to 650 µm with 50 µm instance, and lengths of the panels from 100 µm. The mesh refinement at the corners in each plot was kept consistent to maximally reduce the effect of meshing method on the plotted trend.

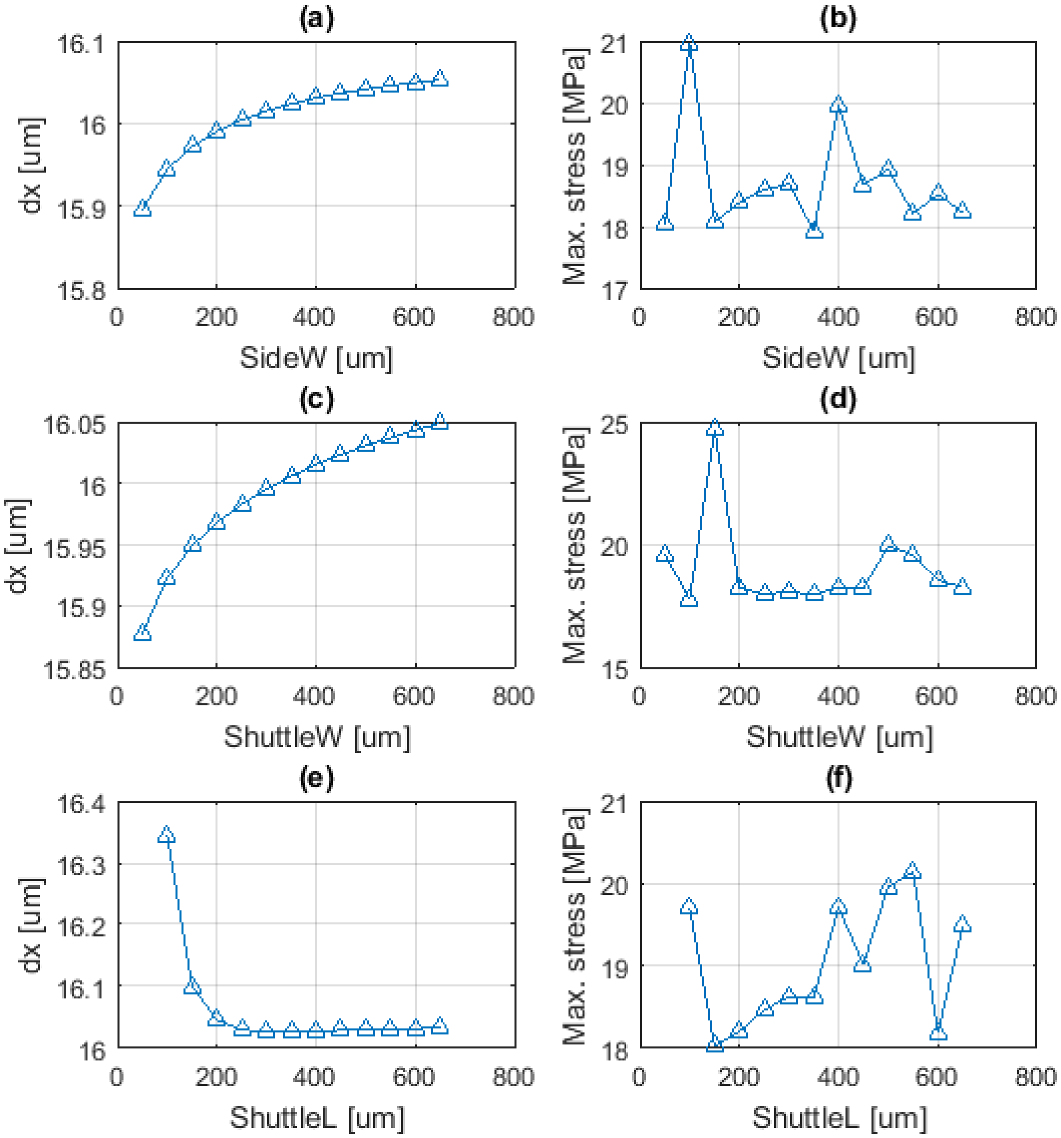

Figure 2-14 – Simulation results of the deflection and maximum von Mises stress induced by a fixed load force, with variations of SideW, ShuttleW and ShuttleL from 50 µm to 650 µm. In each trial, only one parameter was swept while others were kept constant.
Simulation parameters when unchanged were: $BeamL = 1500\ \mu m$, $BeamW = 20\ \mu m$, $BeamH = 10\ \mu m$, , $FilletR = 20\ \mu m$, $Fx = 0.1\ mN$, $SideW = 500\ \mu m$, $ShuttleW = 500\ \mu m$, $ShuttleL = 500\ \mu m$.

Results in Figure 2-14 show that although the simulated deflection monotonically changes with increasing SideW, ShuttleW or ShuttleL in the testing range, the results were all within 1% difference from others, which is very small for simulation purpose.

The stress results show greater variation, but also in an acceptable range. For lengths greater than 200 µm, the results stabilizes in the range of 18 to 20 MPa.

Therefore, the choice of SideW, ShuttleW and ShuttleL within this tested range is not critical to the simulation result.

2.2.4 Simulation Results: Stress vs. Deflection Relationships

With a reasonably refined mesh that is verified using mesh sensitivity test, the relationship between the maximum induced stress and the deflection amount was studied by putting a fixed deflection dx = 50 µm on the shuttle, which is the design target deflection [11]. The parameters of Gen 3 T20 devices were used.

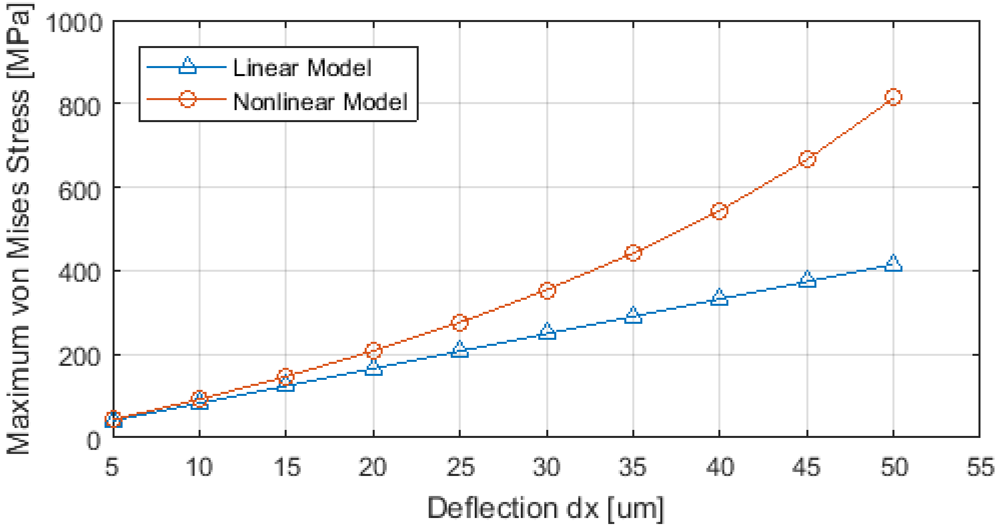

Figure 2-15 – Comparison of simulation results using linear and nonlinear equations. Simulation parameters are: $BeamL = 500\ \mu m$, $BeamW = 20\ \mu m$, $BeamH = 10\ \mu m$, $SideW = 500\ \mu m$, $ShuttleW = 500\ \mu m$, $ShuttleL = 500\ \mu m$, and $FilletR = 0.5\ \mu m$.

Figure 2-15 shows that the maximum stress increases monotonically with increasing deflection as expected. It also shows that while the simulations using linear and nonlinear equations give close results with smaller deflections, the results deviate as the deflection becomes larger. Using the parameters of Gen 3 T20 devices, the maximum equivalent stress is almost twice as high using the nonlinear model at the target deflection of 50 µm. This confirms that including geometric nonlinearity is necessary despite it takes much more computational time than using only linear models.

2.2.5 Simulation Results: Force vs. Deflection Relationships

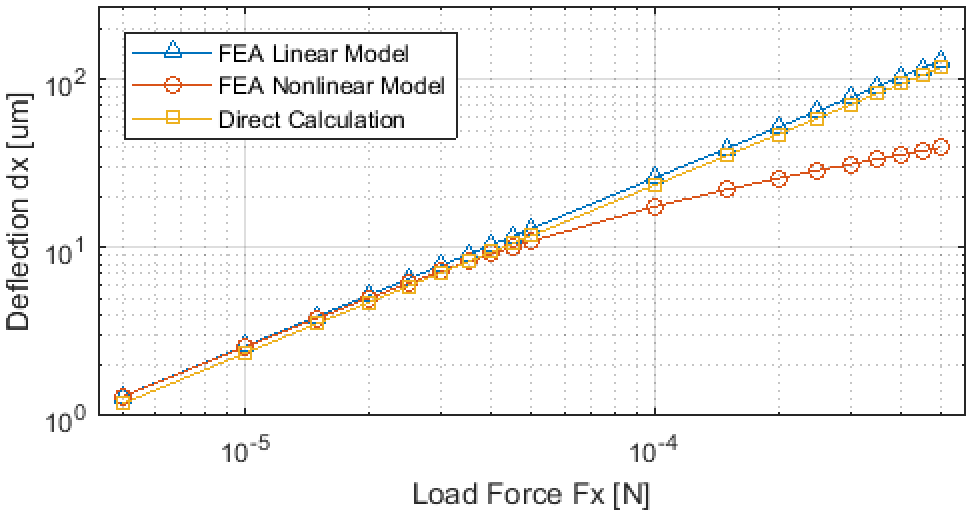

Figure 2-16 - Comparison of simulation results using linear and nonlinear equations. Simulation parameters are: $BeamL = 500\ \mu m$, $BeamW = 20\ \mu m$, $BeamH = 10\ \mu m$, $SideW = 500\ \mu m$, $ShuttleW = 500\ \mu m$, $ShuttleL = 500\ \mu m$, and $FilletR = 0.5\ \mu m$.

Similar to the equivalent stress vs. deflection relationship, the simulation results of the deflection induced by a given load force using linear or nonlinear equations are also close at smaller deflections while large at greater ones.

Another comparison we can make is the comparison of the FEA simulation results with direct hand calculation using Equation 2-3. In the stress simulations, we are using von Mises equivalent stress in the software while only accounting for the bending stress in equations, so the difference between the simulation result using linear model and that using hand calculations is expected to be large. But in the force calculations, both the simulation software and Equation 2-3 are calculating the same thing, which should give similar results, which is confirmed by the plot in Figure 2-16. The slight but consistent-in-ratio discrepancy could be contributed to the fact that FEA is applying the linear equations on small meshing segments while hand calculation applies the same equations to the whole beam at once.

2.2.6 Limitations of the FEA Model

There are several assumptions that we make from the device in reality to the above model for simplification.

1. We are assuming that the stretching of the shuttle and the frame is negligible with respect to the deflection of the legs. Therefore, when comparing the displacement of the shuttle from its original position to the design target, we just use the simulation result from the above model, which is only any one pair of legs in the hundreds.
   A confirmation of this assumption is by performing the calculation of the strain when all of the target force of 5mN is applied on the shuttle only. In Gen 3 devices, the ShuttleW is 300, so the stress is $\frac{5mN}{300\mu m * 10\mu m} = 1.67 \times 10^6 Pa$. The Young's Modulus of Polyimide is 3.3GPa, so the response strain portion is $\frac{1.67\times10^6 Pa}{3.3\text{GPa}} = 5.05 \times 10^{-4}$, which is very small. When legs are

connected, the stress experienced by the shuttle itself will be much less, making the stretching effect negligible.

2. We assume that all dynamics take place in x-y plane only. In reality, the motion of the shuttle may not strictly be in the x-plane, since the pulling is done by hand. The legs may also twist out of plane. The out of plane rotations of the legs, however, should tend to reduce the stress concentrations. Therefore, excluding these motions in our calculation gives a safer estimate of the stress induced.

3. We assume that the variation of the device only happens in x-y directions; nothing should change in the z-direction. In other words, the thickness of the device (height in the z-direction) is uniform. This is far from practical in the actual fabrication process, as both the curing of the polyimide precursor and the oxygen plasma etching processes decrease the thickness more near the edge of the structures.

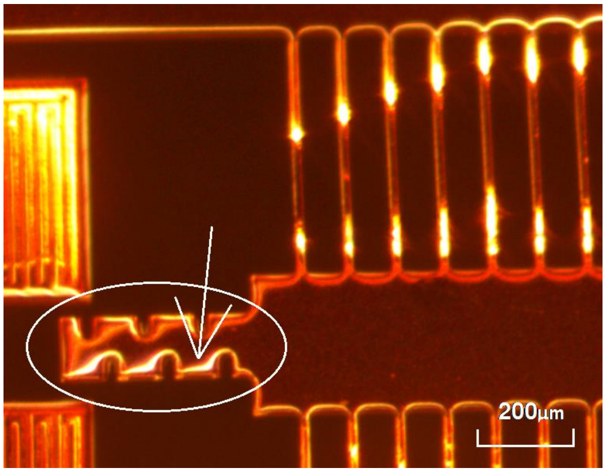

Figure 2-17 - Photo of one Gen 3 T-20 Device under microscope. The reflection of light shows that the top surface is not flat.

The reflection of the light is near the edges confirm that the top surface of the device is not flat but instead gets thinner towards the edges.

2.2.7 A Review of Gen 3 Parameters

FEA simulations using Gen 3 device parameters from [11] were performed to examine their mechanical characteristics if including geometric nonlinearity for large deflections and compare to the design targets.

2.2.7.1 Stress vs. Deflection

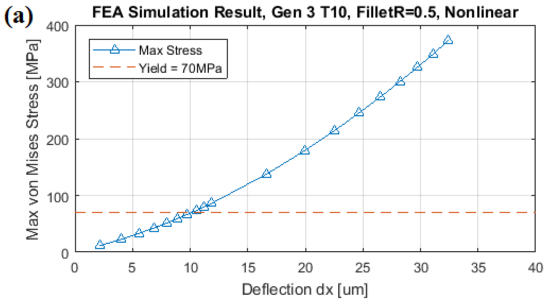

Figure 2-18 – Simulation results of stress vs. deflection using parameters of Gen 3 devices (as shown in Table 2-1): (a) T10 Devices and (b) T20 Devices. Simulation parameters are: $BeamH = 10\ \mu m$, $SideW = 500\ \mu m$, $ShuttleW = 500\ \mu m$, $ShuttleL = 500\ \mu m$, $FilletR = 0.5\ \mu m$, and (a) $BeamL = 300\ \mu m$, $BeamW = 10\ \mu m$; (b) $BeamL = 500\ \mu m$, $BeamW = 20\ \mu m$.

The simulations using parameters of Gen 3 devices show that the equivalent stress well exceeds the yield of the material, which is estimated to be 70 Mpa [11], when the deflection goes above $10\mu m$. This could have made the implanted device unable to restore its original form. Thus the tip of the device could have been pushed less than the desired distance to pierce through the glial sheath formed in the week after implantation. And the force provided could also have not been enough.

2.2.7.2 Deflection vs. Load Force

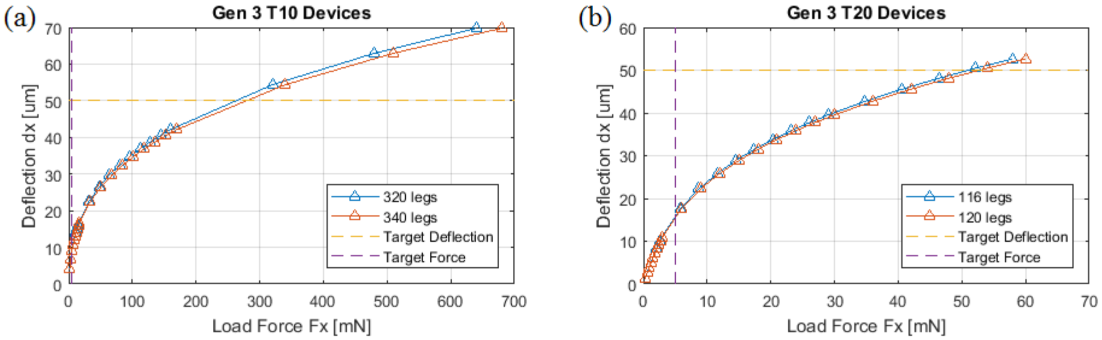

Figure 2-19 – Simulation results of deflection vs. load force using parameters of Gen 3 devices (as shown in Table 2-1): (a) T10 Devices and (b) T20 Devices. Simulation parameters are: $BeamH = 10\ \mu m$, $SideW = 500\ \mu m$, $ShuttleW = 500\ \mu m$, $ShuttleL = 500\ \mu m$, $FilletR = 0.5\ \mu m$, and (a) $BeamL = 300\ \mu m$, $BeamW = 10\ \mu m$; (b) $BeamL = 500\ \mu m$, $BeamW = 20\ \mu m$.

Simulation results in Figure 2-19 show that for all Gen 3 device variations, the load force for the deflection to reach 50 µm was massively overshooting the 5 mN target, if the elastic equations still hold. However, this result is likely no longer valid for deflections greater than 10 µm for T10 or 7 µm for T20 devices, since the maximum stresses exceed the yield.

2.2.8 Verification of FEA Results: Deflection vs. Load Force Test

Unlike the induced stress, which is not easily measurable on benchtop settings, both the deflection and the force can be measured. Hence, a deflection vs. load force experiment was performed to compare with the simulation results.

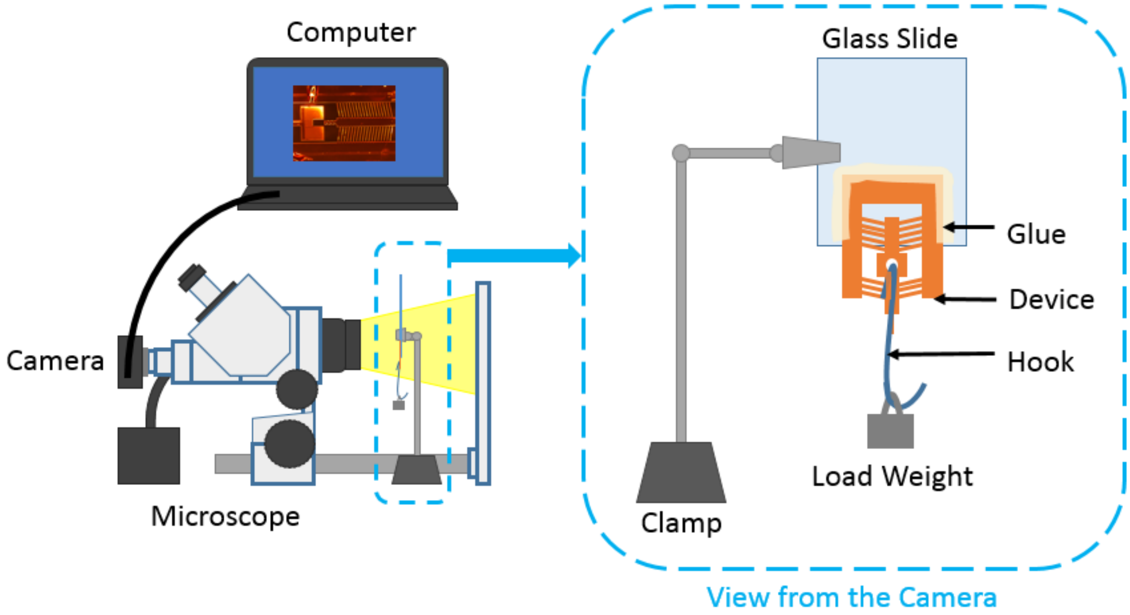

Figure 2-20 – Experiment setup for load force vs. deflection measurements.

The experiment was performed using a Gen 3 NH-PS-T20 device. The device was glued to a holding glass slide, and the slide was held in vertical position by a clamp. A hook made from AWG-30 wire, which provided enough strength while having a small enough diameter, was hung through the hold in the device head. Different load weights were hung on the hook, whose masses were measured using an A&D Weighing GR-200 lab balance. ZEISS® Stemi 2000C Microscope with an Amscope® MU300 CMOS color camera was used to take images of the device with each different load. The images were later analyzed to get the measurement readings.

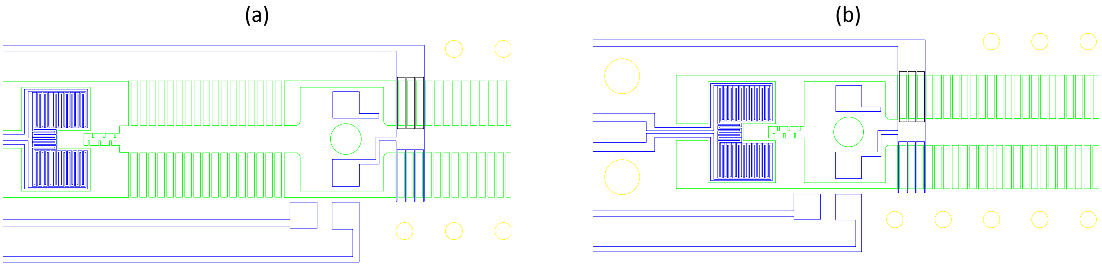

Figure 2-21 – Gen 3 device design from [11]. (a) NH-type device head, with the head in the middle of the moveable shuttle structure. (b) OH-type device head at the opposite end of shuttle as the tip.

The NH-PS-T20 device was chosen because the device head was in the middle of the shuttle, as shown in Figure 2-21, making it easier to hang weights through the hold in the header while holding more of the device on the glass slide.

The parallelism of the camera plane and the device x-y plane is checked by comparing the number of pixels of lengths of known segments in perpendicular directions on the device.

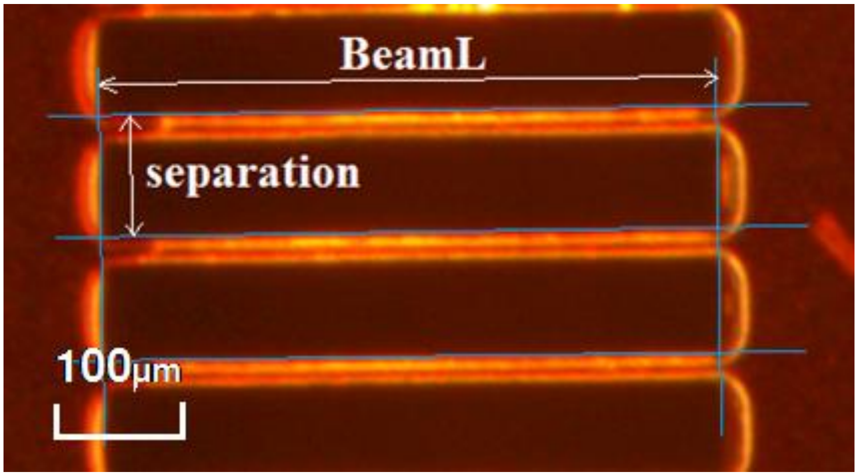

Figure 2-22 – A section of a microscopic picture of the device. The length of the leg BeamL and the separation between legs are both known values, and with no load weight the two segments are perpendicular by design.

Table 2-5 – Average number of pixels of the lengths of the legs (BeamL) and the separation of the legs in the picture with no deformation.

	Average [pixel]	Theoretical length [μm]	μm/pixel
BeamL	309.04	500	1.62
Leg Separation	61.51	100	1.63

The comparison in Table 2-5 shows that the μm/pixel result in both directions are very close, confirming that the camera plane is almost parallel to the device x-y plane.

The deflection amount is determined using the following process:

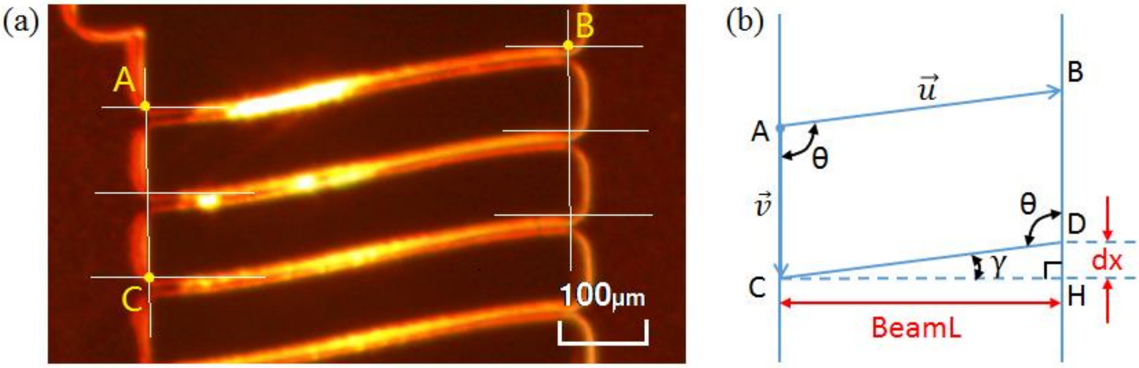

Figure 2-23 – Measuring scheme of the deflection dx. $\overline{CD}$ is parallel to $\overline{AB}$. $\overline{AC}$ and $\overline{BD}$ represent the edge of the shuttle and the frame connected by the legs, respectively, and are parallel by design.

1. Mark the intersections between the legs and the shuttle/frame by crossing lines tangent to the legs and to the shuttle/frame. Figure 2-23a shows an example section of the image.

2. Read x and y coordinates in pixels for points A, B and C. A and B are at the ends of one leg, and C is on the same side of the legs as A.
3. Calculate vectors $\vec{u}$ and $\vec{v}$ using A, B and C, as shown in Figure 2-23b.
4. Use vectors $\vec{u}$ and $\vec{v}$ to get $\angle\theta$. Then $\angle\gamma = \angle\theta - 90°$.
5. Since the frame is glued to the holding glass slide and the setup is symmetric, $BeamL$ should not change significantly during the experiment. Therefore, $dx = BeamL \times \tan\gamma$.

Calculated dx's from multiple legs were averaged. Two sets of two legs were chosen on either side of the shuttle, making a total of 8 legs calculated per image. The same set of the 8 legs were measured in all images taken at different load forces. Since the readings are from microscope images, they may still not be precise.

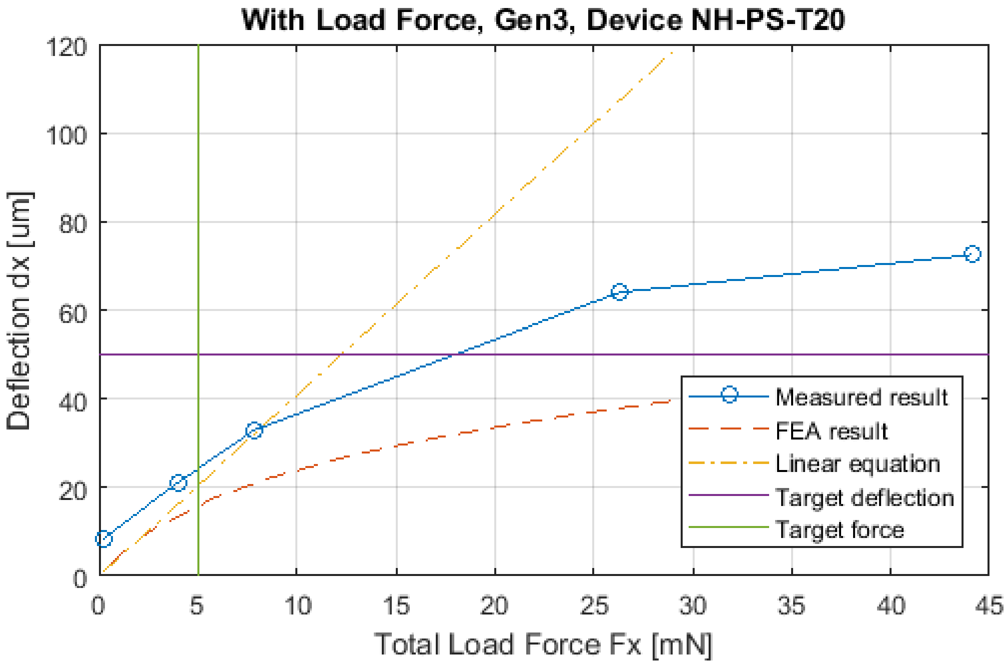

Figure 2-24 – Measured deflection versus load force in Gen 3 T20 device with 58 pairs of legs and a comparison against simulation result. The load weight was applied in strictly increasing order for the data points in this plot.
Simulation parameters: $BeamL = 500\ \mu m$, $BeamW = 20\ \mu m$, $BeamH = 10\ \mu m$, $SideW = 500\ \mu m$, $ShuttleW = 500\ \mu m$, $ShuttleL = 500\ \mu m$, and $FilletR = 0.5\ \mu m$.

Figure 2-24 shows that measurement and FEA simulation results are in the same order of magnitude, which is supportive of our simulation model.

Measured deflections from this experiment show that the relationship is no longer near linear while reaching the desired range of deflection. In fact, the trend looks very similar to the curve given by FEA simulation.

Besides the limitations of the model already mentioned in Section 2.2.6, a factor contributing to the deviation of the measured data from simulation results is that the legs were not perfectly straight at rest. As shown in Figure 2-24, the legs had a deflection of almost 10 μm when there is no load force.

Also, due to the design of Gen 3 NH-type devices (Figure 2-21b), only half of the device frame could be glued to the glass slide. The unattached part of the frame could be pulled towards the middle, making it easier for the legs there to bend.

Furthermore, the devices was made more than 1.5 years before used in this test, meaning that the Polyimide film may have degraded in time, causing the material properties to change slightly. For example, a decrease in Young's Modulus could have made the device easier to bend.

And in the aspect of verifying the yield stress, the result was inconclusive. As previously shown in Figure 2-18, the simulated von Mises stress goes beyond the yield as the deflection exceeds $7\ \mu m$ in T20 devices. The deflection induced by the same load of $26.29\ mN$ before and after a greater load of $44.11\ mN$ was measured. Beforehand the measurement was $64.00\ \mu m$, but afterward it was $67.36\ \mu m$. The structure could have been damaged and lost its ability to restore its original elasticity. However, this difference may also have been partially due to measurement error, so it is inconclusive.

2.3 Gen 3 Impedance Test

Benchtop *in vitro* studies were performed to verify the observed decrease over time of the impedance of the electrodes in the *in vivo* studies [11]. In this study, Phosphate-buffered-Saline (PBS) was used to mimic the environment in the rodent brain.

2.3.1 Experiment Setup

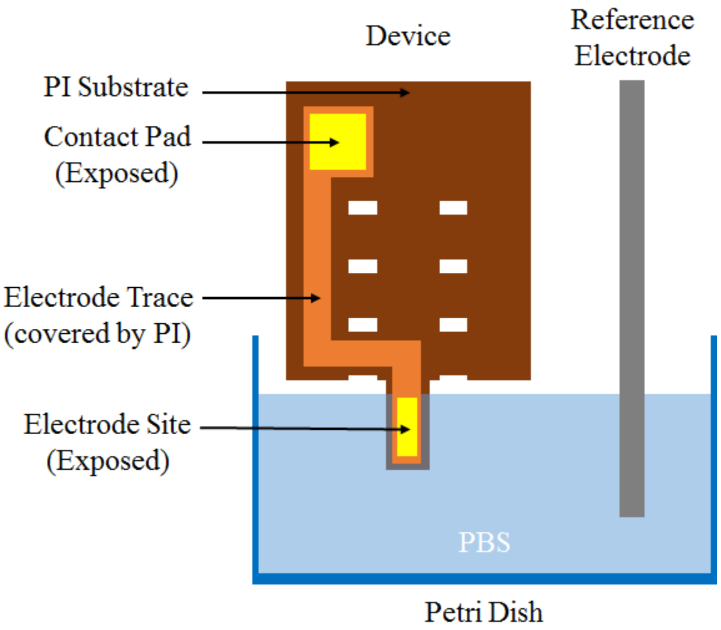

Figure 2-25 – Electrical path in the device.

Figure 2-25 shows a diagram of the electrical path in the device whose impedance was to be measured. The edge of the device frame was glued to a glass slide, and a clamp was used to hold the device in position such that only a desired part of the device is immersed in PBS. The exposed contact pad on the opposite end on the electrode trace was connect to a 5 cm 0.002'' annealed stainless steel wire via silver epoxy. Another 0.002’’ stainless steel wire of similar length was used as the reference electrode, with about 0.5 cm exposed to the PBS solution. The impedance between the ends of the two wires was to be measured.

The two stainless steel wires have a diameter of 0.002’’, which is equivalently about 5×10^{-5} m. With a resistivity of around $1.6 \times 10^{-7}\ \Omega \cdot m$ [25], a 5-cm wire has a resistance of about 4 **Ω**. The contact resistance between the wire and the contact pad on the device are typically on the order of a few ohms [11]. The electrode trace covered by PI on both sides has a maximum length of 42 mm, a width of 100 µm and a thickness of 200 nm [11]. Gold has resistivity of $2.2 \times 10^{-8}\ \Omega \cdot m$ [11], so the trace has a resistance of about 46.2 **Ω**. These resistances connected in series give a total of around 50 to 60 **Ω**, which is negligible compared to the typical measurements of a few hundreds of k**Ω** to more than 1 M**Ω** total impedance previously done by Dighe [11].

The interface between metal and electrolytes in solution can be estimated as a double-layer capacitance proportional to the surface area, which means that the impedance is inversely proportional to the contact surface area. The stainless steel wire had an area of about $8 \times 10^{5}\ \mu m^{2}$ exposed to the solution, which is about 3 orders of magnitude higher than that of the electrode sites of Gen 3 which was designed to be 507 μm^2 [11]. If the behavior or the double-layer interfaces on gold and annealed stainless steel surfaces are similar, that means the impedance of the interface between the wire and PBS is about 3 orders of magnitude lower than the impedance of the electrode site.

Therefore, it is appropriate to assume that the dominant portion of the impedance measured between the two wires is of the electrode site.

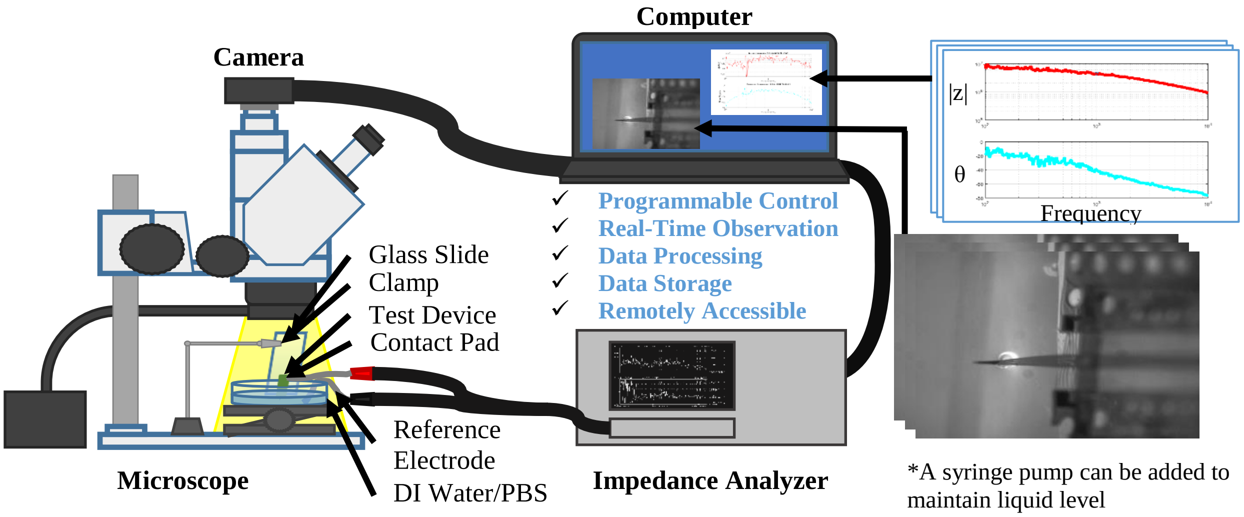

*A syringe pump can be added to maintain liquid level

Figure 2-26 – Experiment setup for long-term impedance monitoring.

A programmable impedance analyzer (Agilent® 4294A Precision Impedance Analyzer) was used to measure the magnitude and phase of the impedance of one electrode site over a frequency span of 100 Hz to 10 kHz. The analyzer was connected to a computer using a GP-IB to USB convertor and USB cable, and can communicate with the computer thorough a virtual USB COM port. Prior to the experiment, the impedance analyzer was calibrated using fixture compensation, and the accuracy of the magnitude and phase was confirmed using several resistors and capacitors of known values.

A Matlab® script was used to set a timer routine. Each time the timer is triggered, the program sends a command to the 4294A to trigger an impedance sweep and read the results from the analyzer. It then plots the magnitude and phase of the received impedance against sweep frequency in separate axes, and shows the magnitude value at 1 kHz. The 1 kHz value is especially relevant for recording neural signals since an action potential usually takes about 1ms. Finally, it writes the raw data into a text file and saves the plots with time stamps.

The computer may simultaneously receive a live feed from the camera installed on the microscope, and saves the image with the impedance data. The imaging system used was ZEISS® Stemi 2000C Microscope with an Amscope® MU300 CMOS color camera mounted on top. Figure 2-27 shows an example of the view of the device in water from the microscope.

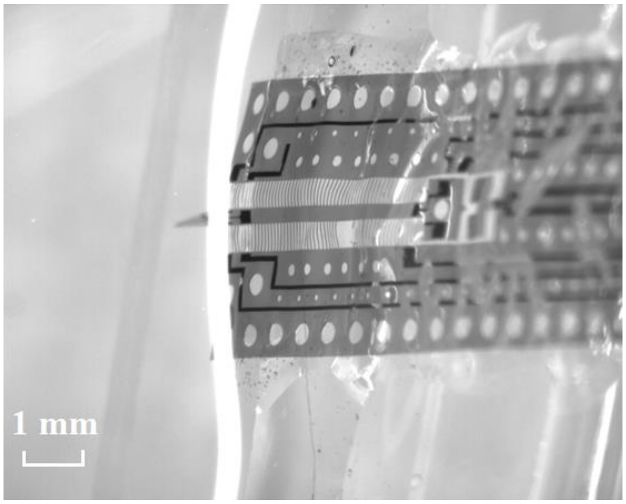

Figure 2-27 – Microscope image of the device in water.

For trials in which the solution level must be held constant, a syringe pump was used to pump in DI water to compensate for the water evaporated. The evaporation rate in the experiment environment was calculated from the distance water level dropped in the container by evaporation with no water intake in one day, and the rate of the syringe pump was set accordingly.

2.3.2 Results and Discussions

2.3.2.1 Impedance of the Reference Electrode

In one experiment, two of the same stainless steel wire with similar lengths were put in PBS, and the impedance between the non-immersed ends were measured. The measured result was about 3 kΩ. This means either reference electrode had an impedance of about 1.5 MΩ, which was about 3 orders of magnitude lower than the previous measured impedances of Gen 3 from a few hundred kΩ to 1 - 2 MΩ. This confirms of assumption in section 2.3.1 that the impedance of the reference electrodes should be negligible in the measured total impedances in this setup. Notably, this 3 orders of magnitude difference is also consistent with our previous estimation from the assumption that the double-layer capacitance behavior at gold and annealed stainless steel surfaces are similar.

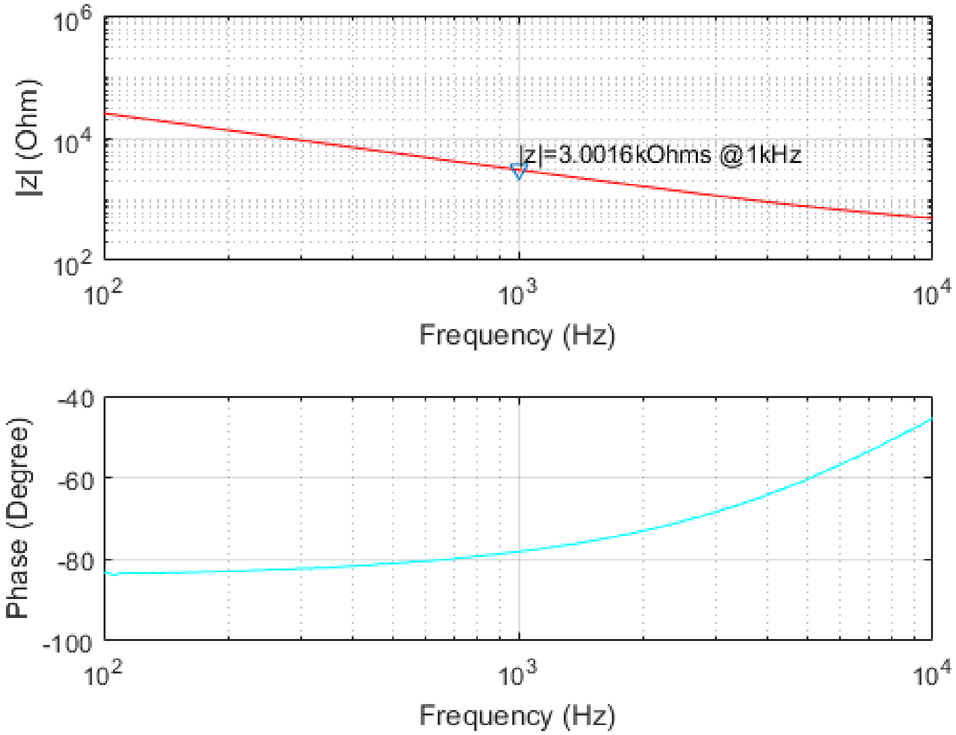

Figure 2-28 – A typical measurement between two reference electrodes.

Figure 2-28 shows a typical measurement between two reference electrodes. The magnitude of the impedance is almost linear as expected. But the underlying explanation of the linearity – that the impedance of the wire in water was expected to be dominated by the capacitance at the interface of the metal surface and water – is challenged by the behavior of the phase. The phase started about -80 degrees at low frequency but increased fast after the frequency was above 1 kHz to about -50 degrees at 10 kHz. This was a curious result, since the behavior we expected was near capacitive, which means the phase would stay close to -90 degrees. This measurement was repeated several times with different wires, but the behaviors of the magnitude and phase against frequency were all similar. The cause of the significant phase increase is yet to be studied.

2.3.2.2 Only Tip in PBS, Constant Solution Level

To test whether the impedance of the electrode also drops in *in vitro* environment and if so, how fast the drop was, one experiment was done with the device tip in PBS while keeping the PBS level unchanged. Measurements were taken every 5 minutes.

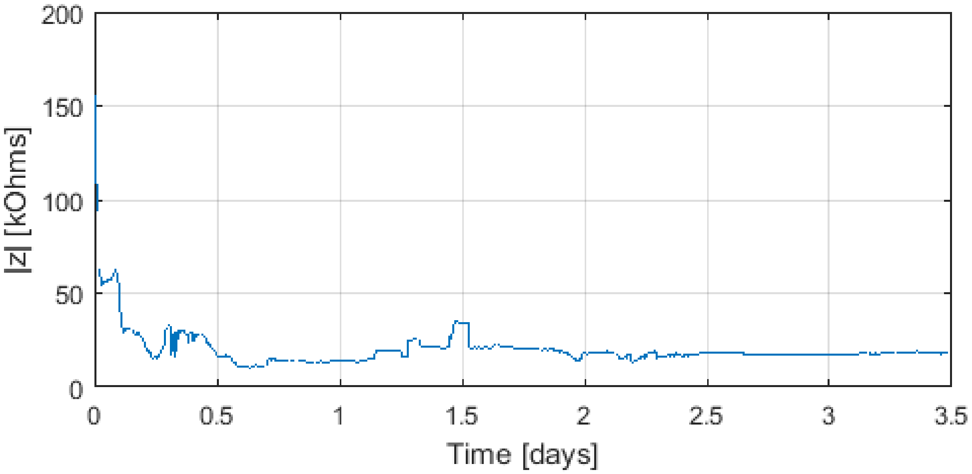

Figure 2-29 – Magnitude of impedance at 1 kHz over time measured with constant PBS level on device tip: full experiment.

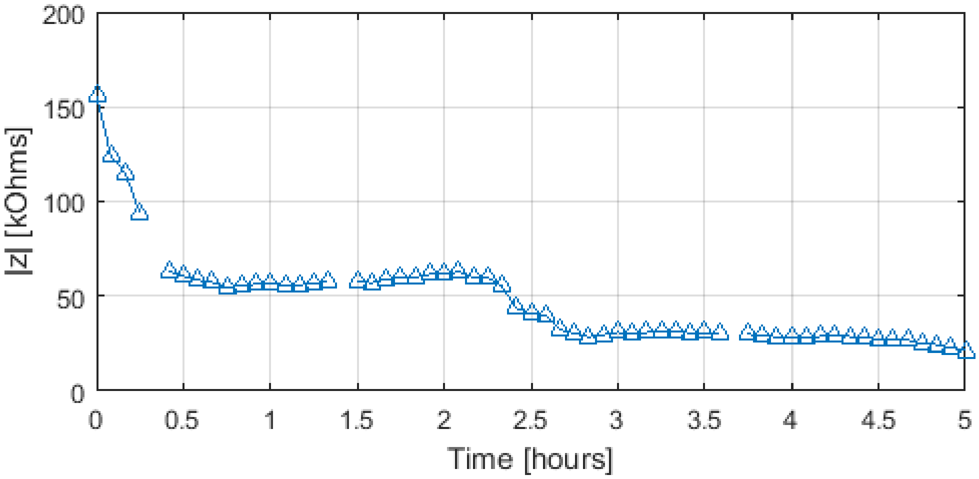

Figure 2-30 - Magnitude of impedance at 1 kHz over time measured with constant PBS level on device tip: first 6 hours.

The recording of the impedance data confirmed that the impedance magnitude of the electrode site at 1 kHz was actually dropping in the *in vitro* setup, as shown in Figure 2-29 and Figure 2-30. A few data points were missing due to occasional GPIB command error or serial communication timeout, cause unidentified. Regardless, the recorded data showed a clear trend over time, which eliminates that the cause of the drop recorded in *in vivo* tests in [11] was not or not only due to *in-vivo*-specific issues such as the animals' movements.

The trend of the impedance magnitude at 1 kHz shows a significant drop in the first half hour and then relatively stabilized at about 18 kΩ after 15 hours. The trend started at 156 kΩ, which was much lower than typical of Gen 3 device benchtop measurements (600-1500 kΩ [11]). This could be due to the set up time between clamping the device and starting the auto-measurements. It was possible that the impedance started at a higher value but had already decreased by the time the first measurement was taken, since the impedance dropped so rapidly in the first half hour. This assumption could potentially have been verified by starting the auto-measurement Matlab® script right after submerging the tip of the device in PBS.

This results is consistent with the hypothesis that delamination took place between the two PI layers. If there is a small gap between the two thin PI layers, the PBS solution would gradually go up in between the layers due to capillary. This would result in much more surface area of the gold trace to be exposed to the ionic environment than initially as designed. An increased exposure would cause an increase in the capacitance of the interface between the trace and the solution, which in turn would decrease the magnitude of the total impedance measured.

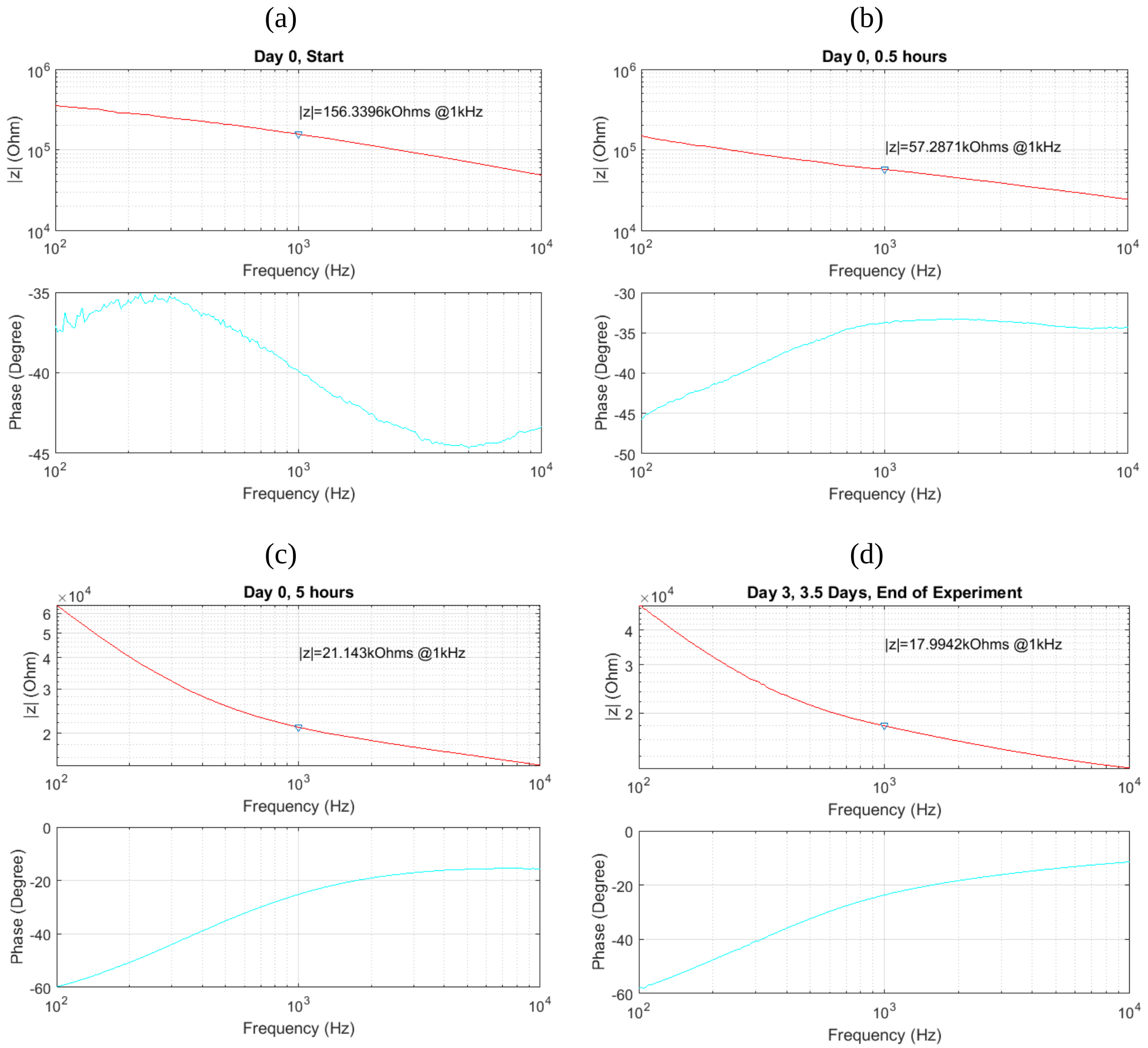

Figure 2-31 – Magnitudes and phases of the impedance at significant time points.

A closer look at the impedance vs. frequency plots at start of recording, after 0.5 hours, after 5 hours, and after 3.5 days (end of recording) showed that the shape of the impedance magnitude and phase curves were changing over time, suggesting a shift of the composition of the measured electrical path over time. At the beginning of the recording, both the shape of the magnitude and the phase resembles those from measurements taken of Gen 2 devices by Dighe [11]. The magnitude curve was slightly convex while the phase curve was sinusoidal in frequency domain. However, after the first half hour as the impedance magnitude dropped significantly as shown in Figure 2-30, the shape of the magnitude curve changed to near linear and the phase curve completely changed. Then as Figure 2-31c shows, in 5 hours, the magnitude curve became concave, and the phase curve became more near monotonically increasing. After that, both the values and shapes of the magnitude and phase curves did not change much till the end of experiment, as shown in Figure 2-29 and Figure 2-32b. These observations are also consistent with our delamination hypothesis, since it would cause the electrical path to change.

The specific shapes of the curves, however, requires further study. In this thesis, we will focus on the temporal change.

Due to the limited working devices from Gen 3 left for testing, this test was not repeated.

2.3.2.3 Only Tip in DI Water, Constant Water Level

To see whether this trend is PBS-specific, a control experiment was done using DI water instead of PBS.

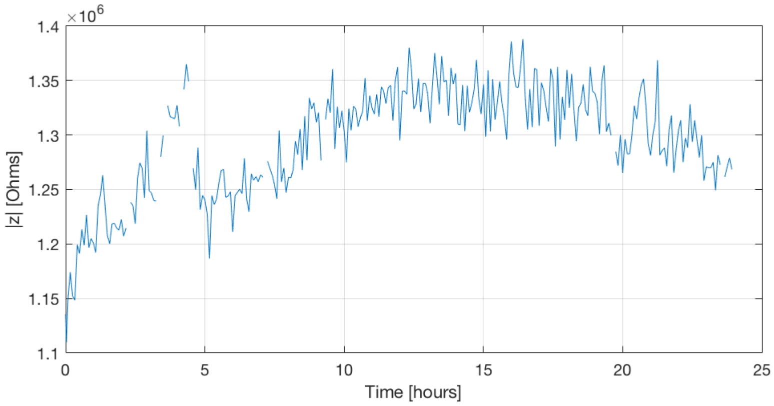

Figure 2-32 - Magnitude of impedance over time measured with constant DI level on the device shows a significant rise in the first few hours and then relatively stabilized.

In this test, the magnitude of impedance increased at first, then stabilized around the higher level, then eventually dropping a little after 20 hours, as shown in Figure 2-32. A few data points were missing due to occasional GPIB command error or serial communication timeout, cause unidentified.

It was surprising that the measured impedance did not show near open circuit behavior, as DI water should have been a poor conductor. This was very likely because the device originally had ions trapped inside the Polyimide due to the extensive exposure to Aluminum etchant when releasing the devices from the wafer. The aluminum etchant used was Transene® Type A [11], which consists of Phosphoric Acid, Nitric Acid, and Acetic Acid [26]. The devices on the wafers were immersed inside the etchant for days before the devices could be released while only rinsed promptly afterwards. The Polyimide HD-4100 is highly water and ion permeable, as HF is one of the recommended methods of pealing cured films from wafers [27]. Therefore, it is reasonable to suspect that although ions from these acids on the surfaces of the device were more likely rinsed away, the ones inside the PI films could have stayed.

This hypothesis also explains the initial increase, as the ions dissolved in DI water and diffused slowly to the whole container in time, decreasing the ion concentration around the device tip. When PBS was used instead of DI water, this initial increase did not show on the plot probably because the ion concentration change caused by the amount of ions in PI was less significant due to the already relatively high ion concentration of 1x PBS, so the factors causing the drop was much more dominant. The same decrease did not show up possibly because the decrease in ion concentration around the device outraced the delamination, and the observed increase is a combination of the two effects.

Another potential reason why the water was conducting is contamination of the container of DI water by ions. This, however, does not explain the initial increase of impedance.

The cause for the drop after 20 hours was still unclear, and how long or to what final value the impedance magnitude decreased to remained unknown since the experiment was only done for 24 hours.

Also, it was inconclusive whether there was another peak at about 4 hours. The recorded values suggested a peak; however, the fact that there were lots of GPIB command errors occurring around that time might not have been by accident. There might have been unknown outside factors that affected the performance of the impedance analyzer during that time, causing the measurement results to be less reliable.

Due to the extremely limited number of electrically functional devices left from Gen 3, the individual experiments were not repeated and thus the results were inconclusive.

2.3.2.4 Other Observations

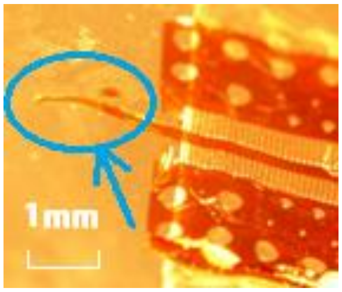

Figure 2-33 – Microscopic picture of one of the test devices after 35h in DI water showed severe delamination on the tip.

One device had its tip submerged in DI water for 35 hours. When the tip was taken out, the two layers were no longer attached to each other and curved apart after drying, as shown in Figure 2-33. This strongly corroborates the delamination theory in Section 2.3.2.2.

2.4 Conclusions and Directions for Gen 4 Design

Mechanical re-modeling of the leg deflection using FEA simulation with geometric nonlinearity suggested that, while the reaction force provided by the legs greatly exceeded the target force in the target deflection range, the stress in the device may have caused plastic deformation. This could have been a cause to the failure of shuttle deployment after 5 weeks in the Gen 3 *in vivo* study.

Meanwhile, *in vitro* testing of the impedance showed the significant decrease in the first few hours after inserting the device tip in PBS. Visible delamination on the tip was also observed after one device was submerged in water for 35 hours. These results were consistent with the PI delamination hypothesis, and they suggested that the delamination happens rather quickly. Therefore, if we are aiming at long-term (~weeks) experiments with the device or even chronic usage for a longer time, the design or fabrication of the device must be improved to solve the delamination problem.

Chapter 3: Gen 4 Device Design and Testing

3.1 Introduction

In Chapter 2, simulations revealed that the maximum stress induced in the device legs could have exceeded the yield with a deflection in the target range. Hence, the design of the legs much be improved to lower the stress concentrations. The FEA simulation model is again used to help determine the design parameters of the legs.

Impedance measurement experiment results in PBS supported our hypothesis that delamination of the PI layers happened when the device was implanted in tissue. Therefore, the composition of the metal trace layer and the fabrication process were revised aiming at improving the adhesion between the metal trace and the PI layer as well has between the PI layers.

3.2 Gen 4 Device Parameters

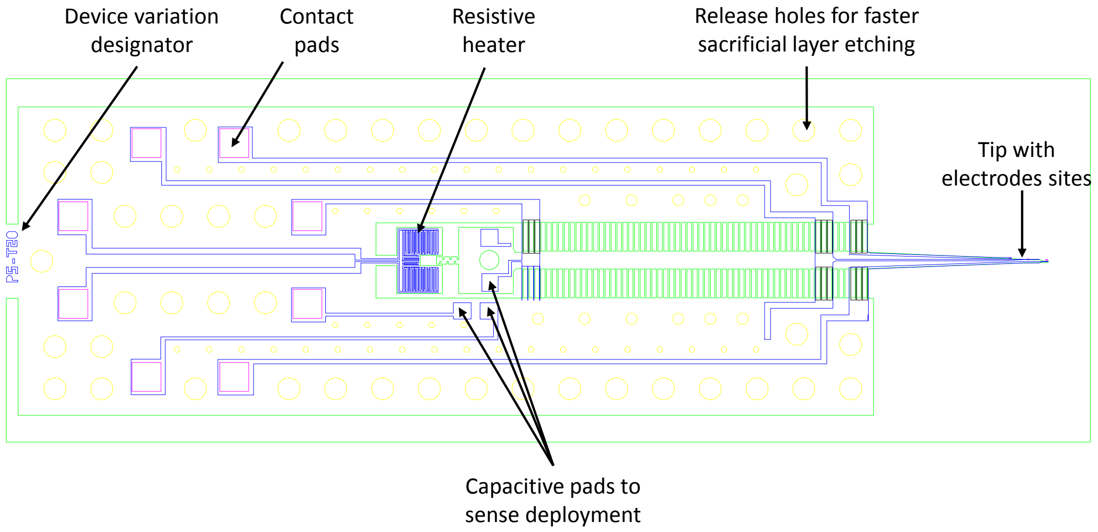

Figure 3-1 – Gen 3 PS-T20 design schematics from [11].

The Gen 4 devices were revised from Gen 3 PS-T20 Devices. The FEA simulation model introduced in the previous chapter revealed that the maximum stress in the old design may have exceeded the yield, and benchtop testing confirmed that the total force required to reach the target deflection of the legs was massively overshooting the force target. Therefore, in Gen 4 the parameters of the legs are revised based on simulation results. Since the device tip, metal trace, resistive heater, capacitive sensors, and contact pads were tested to be functional in Gen 3, their design was not changed.

In revising the parameters of the legs, the main design objective was that the maximum stress induced in the system did not exceed the Yield stress of the material with required deflection range. The other design objective, the total delivered force, could easily be adjusted by changing the total number of legs, as long as the size of the device is kept within practical range in terms of fabrication (fits on a 6-inch wafer) and experimental concerns (not too long to be kept straight when implanted).

The height of the leg was constrained by the thickness of the device, which was determined by the size constraint of the probe tip. Therefore, the author decided to keep the 10 µm thickness as used in Gen 3 devices [11].

3.2.1 Effects of Design Parameters on Stress-Deflection Relationship

The *COMSOL*® FEA model as detailed in Section 2.2.3 was used to examine how varying the fillet size and the width and length of the legs affects the induced stress at a fixed deflection amount.

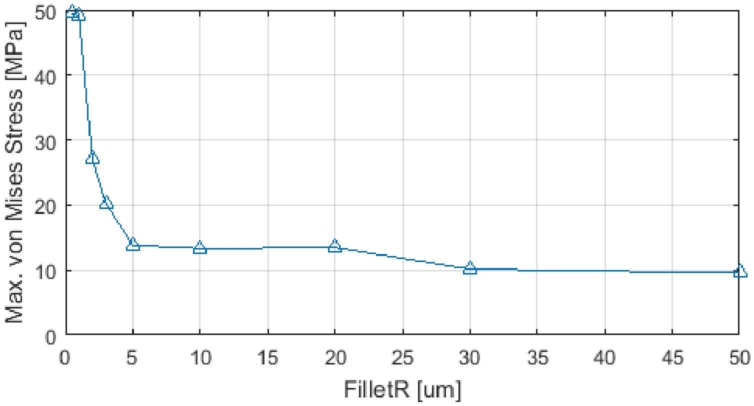

Figure 3-2 – Simulated maximum von Mises stress vs. fillet radius with fixed deflection amount. Simulation parameters: $BeamL = 1500\ \mu m$, $BeamW = 20\ \mu m$, $BeamH = 10\ \mu m$, $SideW = 500\ \mu m$, $ShuttleW = 500\ \mu m$, $ShuttleL = 500\ \mu m$, and $dx = 50\ \mu m$.

Figure 3-2 shows that increasing the fillet size decreases the maximum stress induced in the structure.

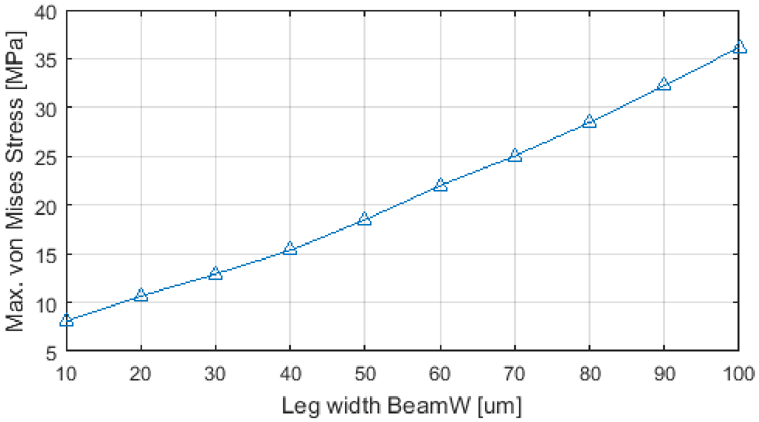

Figure 3-3 – Simulated maximum von Mises stress vs. leg width with fixed deflection amount. Simulation parameters:$BeamL = 1500\ \mu m$, $BeamH = 10\ \mu m$, $SideW = 500\ \mu m$, $ShuttleW = 500\ \mu m$, $ShuttleL = 500\ \mu m$, $FilletR = 20\ \mu m$, and $dx = 50\ \mu m$.

Figure 3-3 shows that increasing the width of the legs increases the max stress.

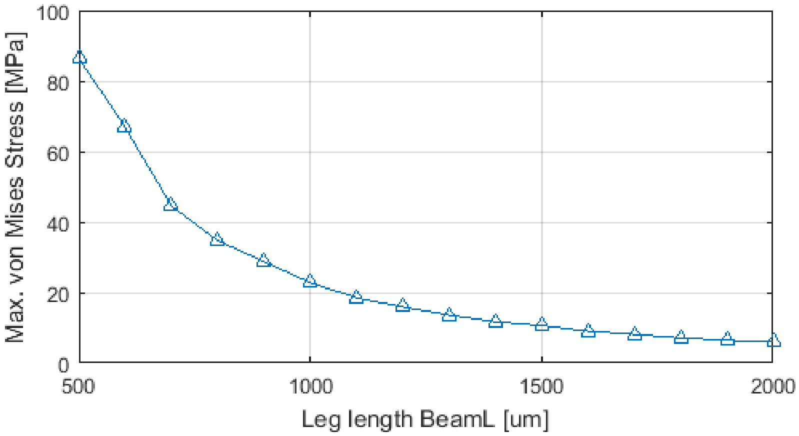

Figure 3-4 – Simulated maximum von Mises stress vs. leg length with fixed deflection amount. Simulation parameters: $BeamW = 20\ \mu m$, $BeamH = 10\ \mu m$, $SideW = 500\ \mu m$, $ShuttleW = 500\ \mu m$, $ShuttleL = 500\ \mu m$, $FilletR = 20\ \mu m$, and $dx = 50\ \mu m$.

Figure 3-4 shows that increasing the length of the legs decreases the maximum stress induced.

3.2.2 Proposed Leg Parameters

Comparing the plots in Section 3.2.1, increasing the leg length is the most space-efficient way to decrease the stress concentrations. The fillet size decreases the stress very slowly as the radius goes beyond 5 µm, and there is a fabrication limit on how thin the legs can be. Therefore, in this section, we will first decide on the fillet size and leg width, then look deeper into specific leg lengths to use for Gen 4 devices.

3.2.2.1 Fillet Size (FilletR)

Increasing the fillet size decreases the maximum stress induced in the structure, as shown in Figure 3-2. Meanwhile, as the fillet gets larger, each pair of the legs takes more space and in turn increase the total size of the device. When one device takes more space, there can be less instances of the device per wafer, and each one is more prone to potential fabrication defects such as bubbles, residues, or alignment errors, which lead to a lower yield of functional devices per wafer. Larger devices are also harder to operate. Therefore, we want a fillet size that is large enough to reduce the stress concentration while keeping the total size of the device reasonable.

The choice was 20 µm.

3.2.2.2 Leg Width (BeamW)

Figure 3-3 shows that increasing the width of the legs increases the max stress.

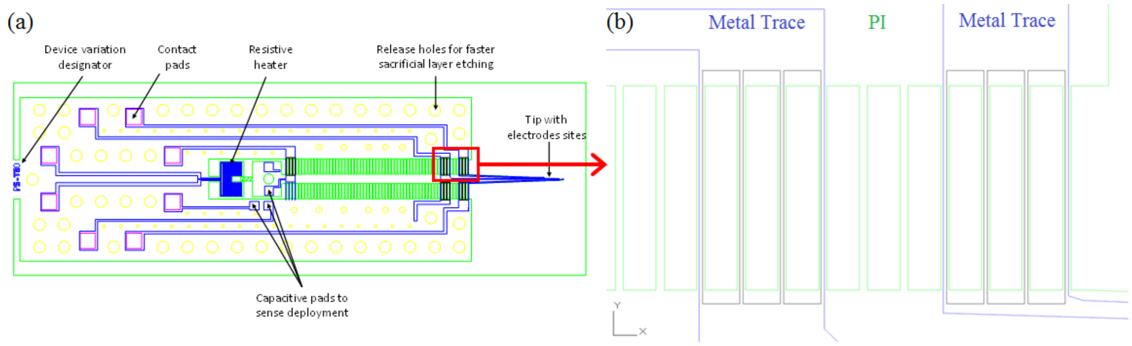

Figure 3-5 – (a) Design of the device from [11] and (b) the metal traces that goes through the legs.

In fabrication of the multiple layer structure, since the metal traces of the electrodes need to go through the legs, as shown in Figure 3-5, the precise alignment of the different layers of the legs may be especially challenging. Having a 20-µm instead of 10-µm leg width allows a higher tolerance of miss-alignment due to equipment precision limit or human error, while still keeping the stress relatively low. A slightly wider leg length also makes the legs less likely to break while releasing the devices from the wafers, which was a lesson learned from the process of releasing Gen 3 T10 (legs 10 µm wide) vs. T20 (legs 20 µm wide) devices from the wafers.

3.2.2.3 Leg Length (BeamL)

As longer legs reduces the stresses, increasing the length also makes the devices wider, taking more space on the wafer. For similar reasons as stated in Section 3.2.2.1, the BeamL should be kept reasonably short.

With fixed FilletR = 20 µm and BeamW = 20 µm, more simulations were run to take a closer look at the maximum stresses within our target range of deflections above 50 µm. A safety factor of 1/3 was used on the maximum stress to account for the limitations of the FEA model.

Table 3-1 – Simulated maximum von Mises stress vs. leg length with fixed deflection amount. Simulation parameters:$BeamW = 20\ \mu m$, $BeamH = 10\ \mu m$, $SideW = 500\ \mu m$, $ShuttleW = 500\ \mu m$, $ShuttleL = 500\ \mu m$, $FilletR = 20\ \mu m$.

BeamL [µm]	dx [µm]	Max stress [MPa]	dx [µm]	Max stress [MPa]	dx [µm]	Max stress [MPa]	dx [µm]	Max stress [MPa]
500	50.0370	86.5806	60.0507	115.7018	70.0653	149.2321	80.0807	186.7456
600	50.0277	66.8700	60.0382	89.1694	70.0497	114.7778	80.0620	143.3479
700	50.0214	44.6476	60.0296	59.7716	70.0388	77.1096	80.0488	96.9253
800	50.0170	34.7460	60.0236	46.5573	70.0311	60.0368	80.0392	75.5024
900	50.0138	28.7516	60.0192	38.5910	70.0254	49.8191	80.0322	62.4047
1000	50.0114	22.7851	60.0160	30.6435	70.0211	39.6286	80.0268	49.7188
1100	50.0096	18.5180	60.0134	25.7346	70.0178	33.3013	80.0227	41.8039
1200	50.0082	15.9212	60.0115	21.4182	70.0152	27.7039	80.0194	34.7619
1300	50.0071	13.6155	60.0099	18.3319	70.0132	23.7208	80.0168	29.7733
1400	50.0062	11.7192	60.0086	15.6148	70.0115	20.2205	80.0147	25.3981
1500	50.0054	10.6331	60.0076	14.3230	70.0101	18.5476	80.0129	23.2967
1600	50.0048	9.0635	60.0067	12.7953	70.0090	16.5845	80.0115	20.8492
1700	50.0043	8.1279	60.0060	10.9904	70.0080	14.2552	80.0103	17.9322
1800	50.0038	7.1325	60.0054	9.6216	70.0072	12.4759	80.0092	15.6895
1900	50.0035	6.4510	60.0049	8.7060	70.0065	11.2931	80.0083	14.2068
2000	50.0031	5.9378	60.0044	8.0200	70.0059	10.4113	80.0076	13.1073

🟥	Above yield	🟨	Above 1/3 of yield	🟩	Safe

BeamL = 1200 µm gives about 10 µm of operational error tolerance while pulling the legs. If BeamL = 1500 µm, the shuttle can be pulled up to 80 µm without the maximum stress going over 1/3 of the yield stress. Another variation, BeamL = 2000 µm, was chosen as a back up, in case there were other large contributing factors neglected in the simulations.

3.2.2.4 Summary of Gen 4 Leg Dimensions and Fillet Size

Table 3-2 – Gen 4 Leg Dimensions and Fillet Size

Type	BeamL	BeamW	BeamH	FilletR
1	1200	20	10	20
2	1500	20	10	20
3	2000	20	10	20

3.2.3 Force-Deflection Relationships using Chosen Parameters

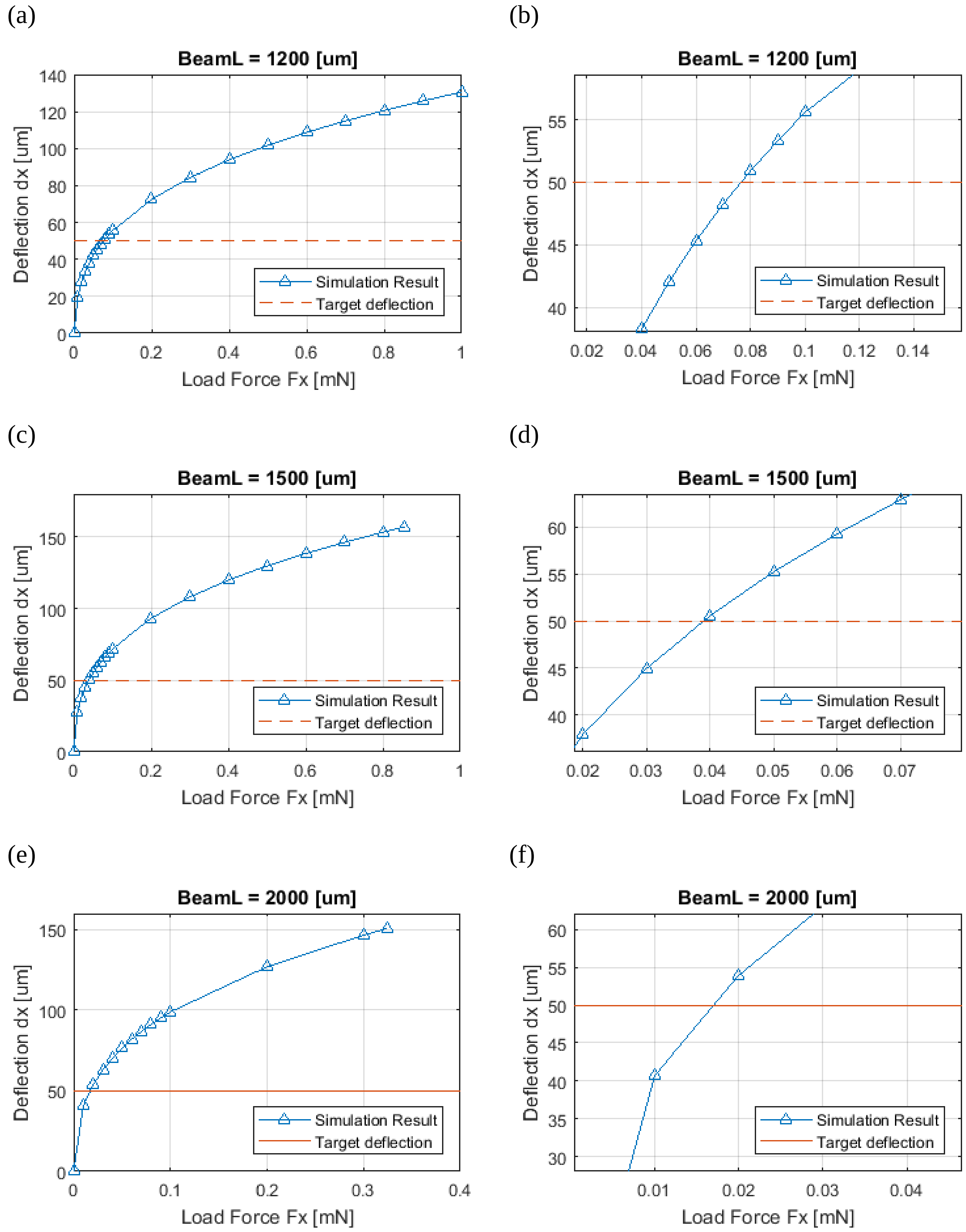

Figure 3-6 – Deflection vs. load force per pair of legs using chosen BeamL.
Simulation parameters: $BeamW = 20\ \mu m$, $BeamH = 10\ \mu m$, $SideW = 500\ \mu m$, $ShuttleW = 500\ \mu m$, $ShuttleL = 500\ \mu m$, $FilletR = 20\ \mu m$.

From Figure 3-6, we can read the approximate force required to reach the target deflection in each pair of legs. The number of legs required to provide 5 mN of total force is detailed in Table 3-3. The actual number of legs was determined while including a safety factor. They were chosen to be 1.6 times of the number required predicted by the FEA model.

Table 3-3 – Load force required per pair of legs and the number of legs

BeamL	Load Force per pair at 50 µm	# Pair of legs required	# Pair of legs in Gen 4
1200	0.08	63	100
1500	0.04	125	200
2000	0.02	250	400

3.2.4 Leg Separation

How far apart each pair of legs are from their neighbors should have negligible effect on the mechanical characteristics of the device. Theoretically, the spacing in between only need to leave enough space for two fillets. In fabrication, however, small spacing in the structure can be hard for the developer to sink in and react fully with the photoresist. On the other hand, large spacing makes the devices longer, which, as detailed in Section 3.2.2.1, is undesired.

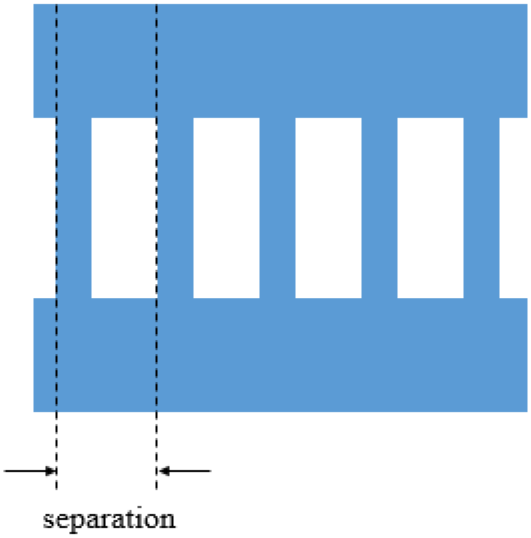

Figure 3-7 – Leg separation.

Here, we define the separation as the total space taken by each pair of legs, measured between the edges on the same side of two neighboring legs. In Gen 4, separation of 60, 70 and 100 µm were used.

3.2.5 Summary: Proposed Variations of Gen 4 Devices

Table 3-4 – Summary of Proposed Gen 4 Parameters and Simulation Predictions

Name	BeamL [µm]	Separation [µm]	# Pair of legs	Force at 50 µm [mN]		Max. stress [MPa] at 50 µm	Deflection safe range* [µm]
				Per pair	Total		
1200A	1200	60	100	0.08	8	15.9212	< 59
1200B	1200	70	100	0.08	8	15.9212	< 59
1200C	1200	100	100	0.08	8	15.9212	< 59
1500A	1500	60	200	0.04	8	10.6331	< 81
1500B	1500	70	200	0.04	8	10.6331	< 81
1500C	1500	100	200	0.04	8	10.6331	< 81
2000A	2000	60	400	0.02	8	7.1325	< 98
2000B	2000	70	400	0.02	8	7.1325	< 98
2000C	2000	100	400	0.02	8	7.1325	< 98
*The maximum deflection for which the induced stress does not exceed 1/3 of the yield stress.							
For all variations, device height = 10 µm, leg width = 20 µm, fillet radius = 20 µm.							

3.3 Device Design and Mask Layout

3.3.1 Device Schematics

The design was modified from

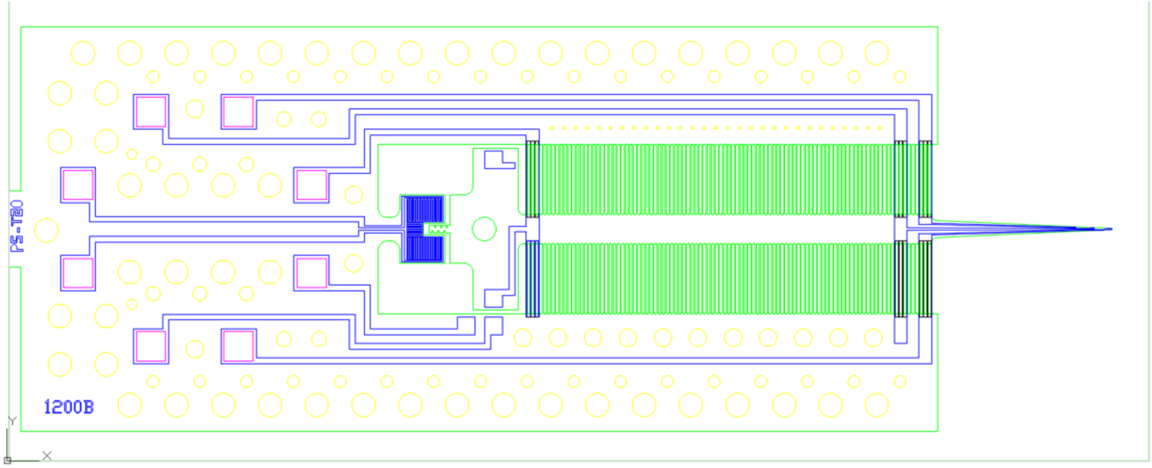

Figure 3-8 – Gen 4 design revised from the Gen 3 devices.

3.3.2 Test Devices for Deflection vs. Force Measurement

To verify the new Gen 4 leg design parameters using FEA simulation results, an additional type of devices was designed specifically for testing deflection vs. load force relationships.

Table 3-5 - Summary of Proposed Gen 4 Test Device Parameters and Simulation Predictions

Name	Legs identical to	BeamL [µm]	Separation [µm]	# Pair of legs	Force at 50 µm [mN]		Max. stress [MPa] at 50 µm	Deflection safe range* [µm]
					Per pair	Total		
T1200	1200B	1200	70	100	0.08	8	15.9212	< 59
T1500	1500B	1500	70	200	0.04	8	10.6331	< 81
T2000	2000B	2000	70	400	0.02	8	7.1325	< 98
*The maximum deflection for which the induced stress does not exceed 1/3 of the yield stress.								
For all variations, device height = 10 µm, BeamW = 20 µm, FilletR = 20 µm.								

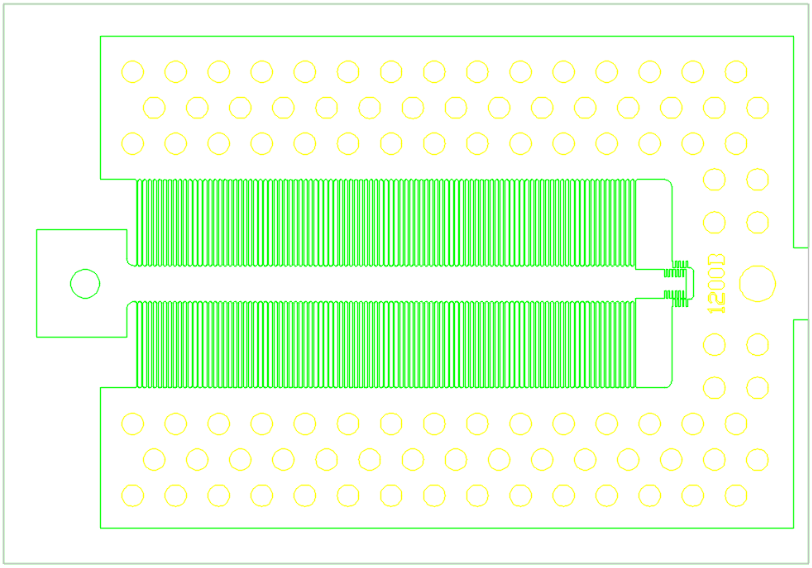

Figure 3-9 – Design schematics for the test devices.

The leg parameters are the same as the B-series devices, with no metal traces. The device head is placed such that it is easier to hang a hook through the hole in it during the experiment, while gluing most part of the device frame to the holding glass slide.

3.3.3 Mask Layout

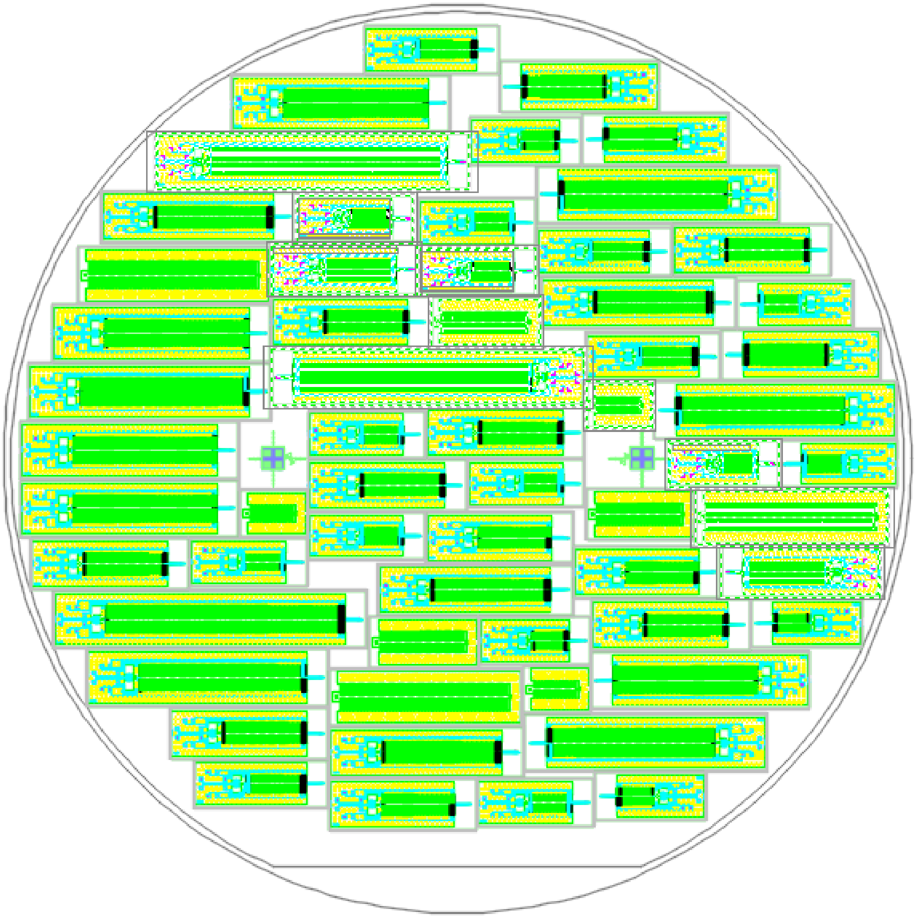

Figure 3-10 – Mask layout of variations of Gen 4 devices and the test devices.

Devices with the same parameters were spread out on different places of the wafer to avoid failure of one particular variation of the device due to fabrication error on one section of the wafer. The tips were maximally facing the center of the wafer since the areas near the edges were more prone to fabrication errors.

3.4 Gen 4 Device Fabrication

The fabrication process of the device is adjusted from that of Dighe's devices as in [11]. Section 3.4.1 will include a description of the process, with the main adjustments and their justifications highlighted in Section 0. Some issues observed in the final fabrication product as well as experienced in device testing will be described in Section 3.4.3 as reference for future fabrication process modifications.

3.4.1 Fabrication Process Flow

The fabrication process uses 6-inch-diameter silicon wafers and includes 7 steps.

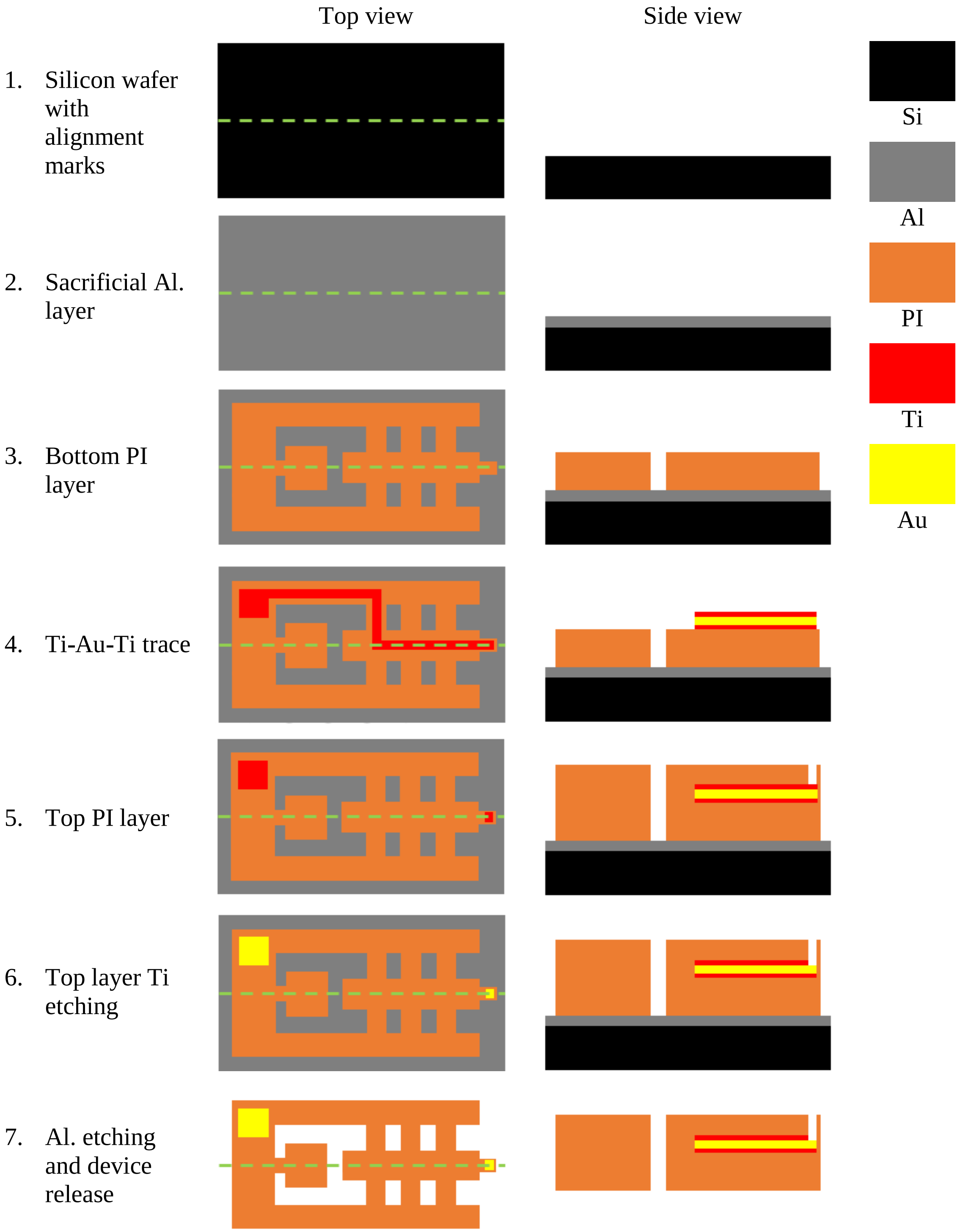

Figure 3-11 – Fabrication process of the device. The side view on the right shows a cross-sectional view along the green dashed line of the corresponding top view on the left.

3.4.1.1 Etching Alignment Marks on Silicon Substrate

An 1-µm-thick layer of positive photoresist patterned with alignment marks is put on a 6-inch, single-side polished silicon wafer. A LAM AutoEtch 490B plasma etcher is then used to etch the alignment marks into the silicon wafer through the exposed areas uncovered by photoresist (primary gas: Cl_2; secondary gas: He; etch time: 3 min 45 sec). Afterwards, the photoresist layer is removed by piranha etch (3:1 concentrated H_2SO_4: 30% H_2O_2).

3.4.1.2 Sacrificial Aluminum Layer

Immediately after the wafers are cleaned in piranha etch and spin-dried, a 1-µm aluminum layer is deposited onto the wafer using an Applied Materials Endura® metal sputtering system. This aluminum layer will be etched away to release the devices from the silicon wafer in the final step.

3.4.1.3 Bottom Polyimide Layer

The precursor of Polyimide HD-4100 from HD MicroSystems™ is dispensed on the wafer with a low spinning speed. After making sure no air is trapped in the highly viscous precursor solution, the precursor is spread with a spin speed of 1000 rpm for 25 sec with an initial 200 rpm/s ramp up, and then with a final spin speed of 3000 rpm for 60 sec with an initial 500 rpm/s ramp up. This set of parameters of the spinning process is tested to be optimal for the target thickness of the two PI layers after curing, which is 10 µm total.

The wafer then goes through a soft bake process on horizontal hot plate surfaces (90℃ for 3 min and then 110℃ for 3 min), in order to provide the surface with resistance against the developer after exposure [27].

The polyimide layer is then patterned with photolithographic masks using Electronic Visions 620 (top side transparent; soft contact; interval; 30 µm separation; expose 5 sec, delay 8 sec, expose interval 6). After exposure, the wafer is developed in HD MicroSystems™ PA-400D using a puddle process for 4 min. It is rinsed in 1 PA-400D : 1 PA-400R solution for 10 sec, in PA-400R solution for 10 sec, and then dried. A post-develop bake of 150℃ for 2 min and 200℃ for 2 min follows.

The polyimide precursor layer then goes through a partial-cure process in an oven in a nitrogen environment. The temperature of the oven ramps up from room temperature to 200℃ at a rate of 10℃/min, hold at 200℃ for 15 min, ramp up to 250℃ at a rate of 10℃/min and then hold at 250℃ for 15 min. The wafers are then allowed to gradually cool down to room temperature.

3.4.1.4 Conductive Metal Trace

A 10-nm titanium – 200-nm gold – 10-nm titanium metal layer including the traces of the electrodes and resistive heater is patterned on the wafer. The titanium layers are added to improve the adhesion between gold and PI. The trace is patterned using Microchemicals AZ® 5214 photoresist, exposed using Electronic Visions 620 and developed in AZ® 422 using a puddle process. The metal deposition process uses an Temescal® FC2000 electron beam evaporator. The excessive metal and photoresist is then removed using acetone liftoff process.

3.4.1.5 Top Polyimide Layer

The process is very similar to building the bottom PI layer as described in step 3. Minor adjustments include a short oxygen plasma etch cleaning process before dispensing the PI precursor on the wafer. The final spinning speed to spread the precursor is decreased from 3000 rpm to 2500 rpm. And instead of the partial-cure process, the wafer now goes through a full cure process with the final holding temperature and time increasing from 250℃ for 15 min (as in step 3) to 375℃ for 60 min.

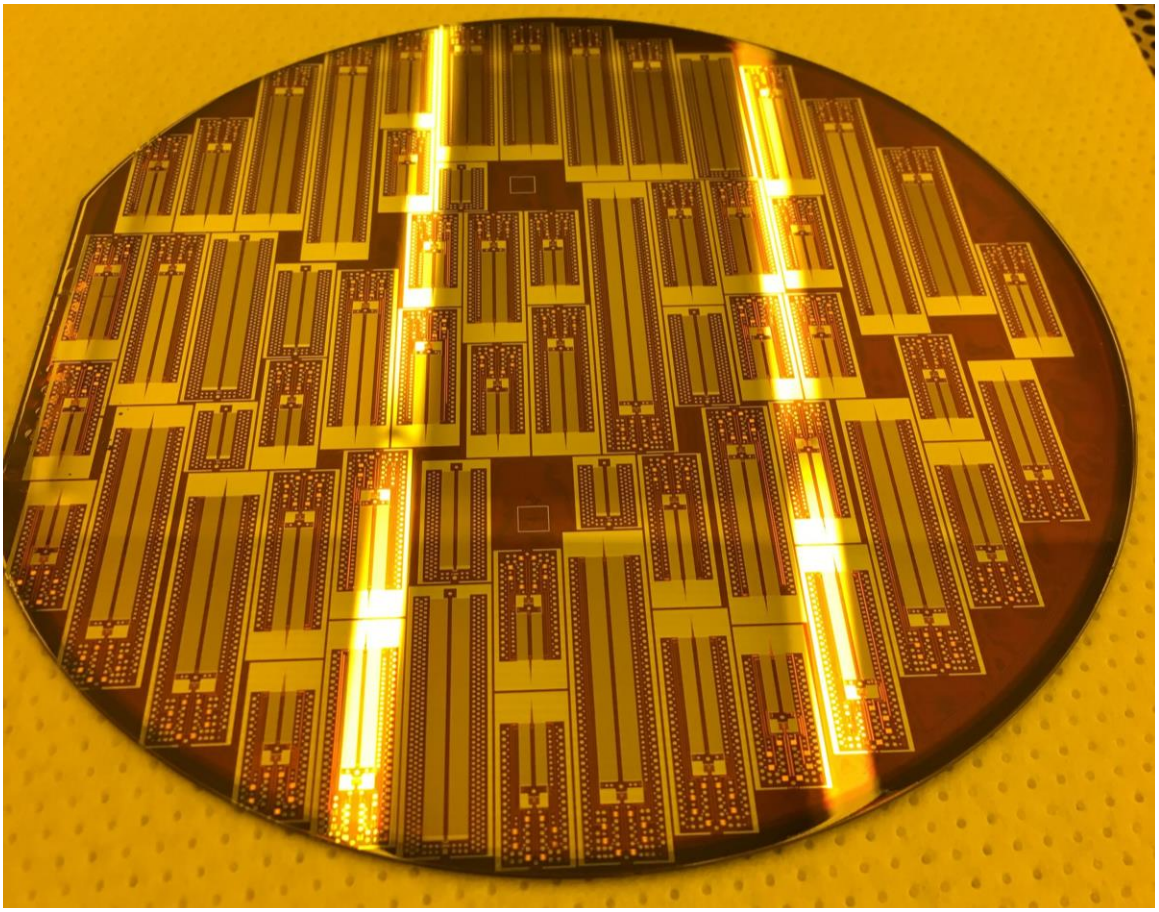

Figure 3-12 – Wafer with patterned devices after fully curing both PI layers.

3.4.1.6 Etching Top Titanium Layer

The titanium at the exposed areas on the top PI layer such as the electrode sites and contact pads is removed using diluted hydrofluoric acid (10 H2O: 1 49% HF).

3.4.1.7 Device Release

In this final step, the sacrificial aluminum layer is removed by emerging the wafer in Transene® type A aluminum etchant, allowing the devices to be released from the wafer.

3.4.2 Main Adjustments from Gen 3 Process

3.4.2.1 Partial Cure Temperature and Time of the Bottom PI Layer

The benchtop impedance measurements of the Gen 3 devices suggested that the adhesion between two PI layers was not ideal, causing delamination. An approach to improve this issue was to lower the curing temperature and shortening the curing time of the devices, leaving more free bonds at the surface to attach to the second layer. In previous generations, the final curing temperature and holding time after ramping up the temperature from room was 300 ℃ for 30 minutes. This step was modified to 250 ℃ for 15 minutes for Gen 4 devices.

3.4.2.2 Composition of the Metal Layer

In Gen 3, the metal trace layer was Ti-Au. The 10 nm Ti layer was put between the bottom PI layer and the 200 nm Au trace to enhance the adhesion of the Au trace to the PI. In Gen 4, another 10 nm Ti layer was added on top of the Au layer to help the adhesion between the Au trace and the top PI layer.

In order to remove the top Ti layer in the electrode site and contact pad openings, after the second layer was fully cured before releasing the devices from the wafer, the Ti was etched in Etch Ti with 10:1 HF (10 H_2O: 1 49%HF) for 2 sec at room temperature. Since HF was also one of the recommended methods of removing cured PI films from the wafers [27], the process was kept extremely prompt to avoid the HF solution from penetrating the PI layers and attack the unexposed parts of the Ti layers as well as from releasing the devices from the wafer.

3.4.2.3 Plasma Etching of the Bottom PI Layer

To further enhance the adhesion between PI layers, before starting the top (second) PI layer, an oxygen plasma-etching step was added. The partially cured bottom (first) PI layer with patterned metal trace layer on top was plasma-etched in oxygen at 1000W for 1 minute immediately before the PI precursor was dispensed on the wafer.

3.4.3 Lessons Learned from Fabrication Modifications

3.4.3.1 Edge Space on Mask Layout

The layout should leave more space near the outer edge of the wafer, in case alignment markers on the silicon wafer in the initial fabrication step was slightly off-center. It should allow even more space near the flat of the wafer, allowing more space for the tweezer to operate. The author recommends a minimum of 0.5 inch.

3.4.3.2 Wrinkles in the Metal Trace Layer

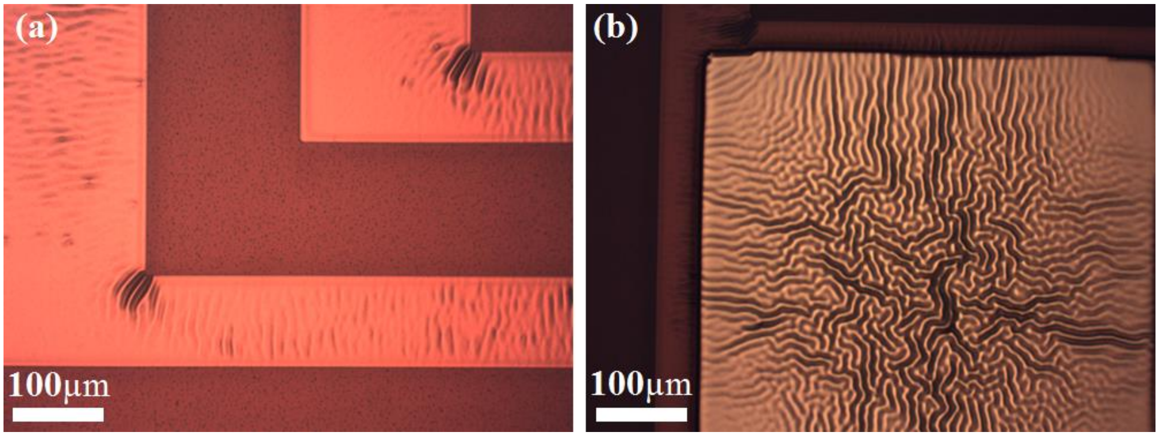

Figure 3-13 – Wrinkles in the metal trace layer

As shown in Figure 3-13, wrinkles were observed in the metal trace layer, especially near corners of the metal trace (Figure 3-13a) or in the exposed area such as the contact pad (Figure 3-13b). The most likely cause of this issue is that the partial curing of the bottom PI layer was insufficient. Aiming at enhancing the adhesion between two PI layers by leaving more open bonds on the first one, the partial curing temperature and time were dropped in Gen 4 fabrication. It is likely that the temperature was too low and the time was too short, so the solvent in the PI precursor had not been fully vaporized before the metal trace layer was deposited. As a result, the solvent in the bottom PI layer got released during the final curing process with the top PI layer, attacking the metal trace which blocks the way out during the process. Therefore, in future modifications of the fabrication process, the temperature and time parameters of the partial curing process should be increased to avoid this problem.

Due to this issue, the electrical properties of the electrode traces would deviate from the original design target. Both the length and width of the traces, as well as the contact area of the electrode sites with the environment, have changed, which should lead to a non-negligible change in the impedance. Nevertheless, no visible cracks were observed in the traces, suggesting that the devices should still be functional for testing.

3.4.3.3 Leg Spacing

The 70-µm leg separationg or 40-µm spacing between adjacent legs were more than sufficient for developing photoresists cleanly. Longer devices were proven to be harder to work with. They were more easily damaged by curling or folding while releasing the devices from the wafer, since the double-layer of PI would be be floating in the acid solution when no longer attached to the wafer via the sacrificial aluminum layer. Therefore, it is strongly recommended to keep the overall device size minimum.

3.5 Gen 4 Benchtop Characterization: Mechanical Performance

3.5.1 Deflections with Load Forces

The deflection vs. total load force relationship was measured using the same setup as previously introduced in Section 2.2.8. More data points were taken in the test of each device by increasing the variation of different load weights added. Two legs that are ten legs apart were used for the calculation for each data point, and the same set of two legs were used for all images for each device. They were taken ten legs apart so that even if end of the legs were marked 1 or 2 pixels off, the effect of the error is effectively low because 1 or 2 pixels represents very small distance (1.6 to 3.2 µm) compared to the distances between any two points (the chosen legs were 700µm apart). Due to this improvement of the measurement process, only two legs' (four points') coordinates were obtained on each image, compared to the 4 sets of 3 adjacent legs used in the previous test of Gen 3 device (where adjacent legs were 100 µm apart).

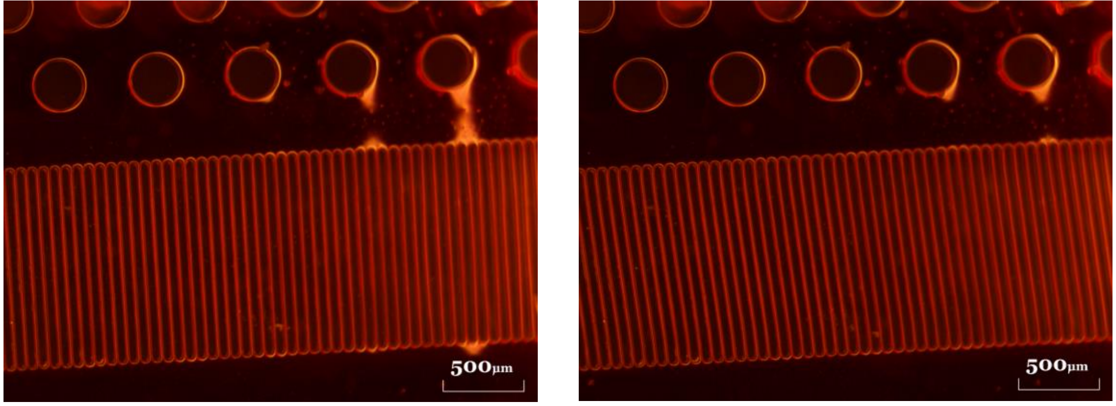
(a) T1200, No Load (b) T1200, Load = 73.74 mN

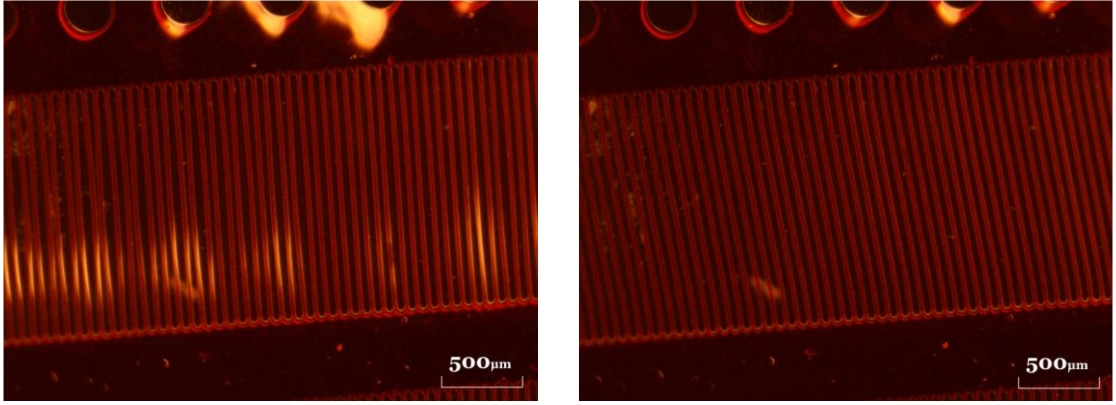
(c) T1500, No Load (d) T1500, Load = 107.98 mN

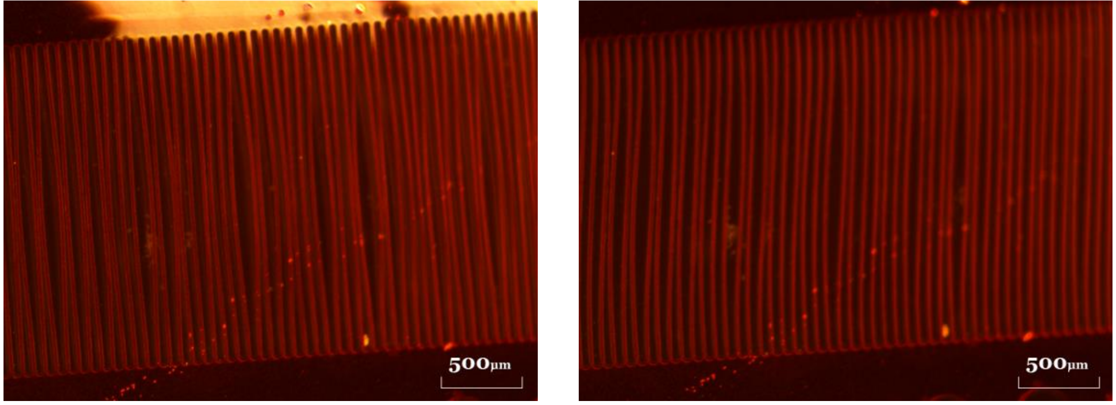
(e) T2000, No Load (f) T2000, Load = 98.18 mN

Figure 3-14 – Microscope images of the test device legs when there is no load weight attached vs. when there is load.

As Figure 3-14 shows, putting a large load weight on the shuttle produced an obvious deflection in the legs. The images in (b), (d) and (f) shows the maximum loads the author was able to apply to the devices before the holes holding the hook in the device head broke.

It was notable that, while the legs were mostly straight in the T1200 devices, they were bending before any load was put on the shuttle in T1500 or T2000 devices, and the bending was more severe in the T2000 devices. This bending could have been caused by unbalanced residual stress in the two PI layers, so that the devices were not flat. It may also have been caused by the swelling of the PI material due to the excessive exposure to acid solution (Al. Etchant) during device release. The swelling could potentially lower the stress in the legs [12]. It may also lower the required force to deflect, since it makes the legs longer.

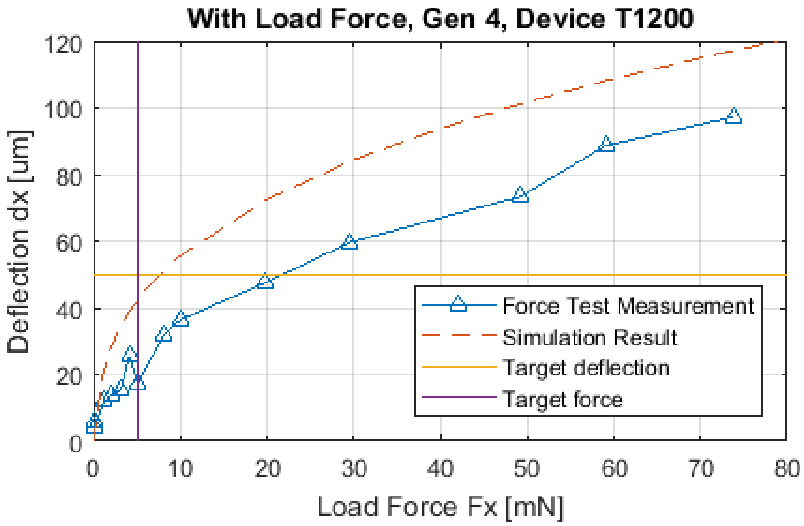

Figure 3-15 – Measured deflection vs. load force result in T1200 Device.

For the T1200 Devices, Figure 3-15 shows that the measured deflections were consistently lower than the simulation result. The measured results were mostly 20% to 30% lower than simulation predicted, which means a relatively high simulation validity. There could have been due to the simplification of the simulation model. They may also have been partly due to differences in material properties from simulation parameters. The simulations used results from HD Microsystems™ [18] and Grady et al. [19], but the actual device material may perform differently due to differences in the PI precursor product batch or fabrication process. In terms of the goal of the device, however, a lower deflection at a given load force means that the reaction force provided by the shuttle is higher than expected at the target deflections, which means that the device still works.

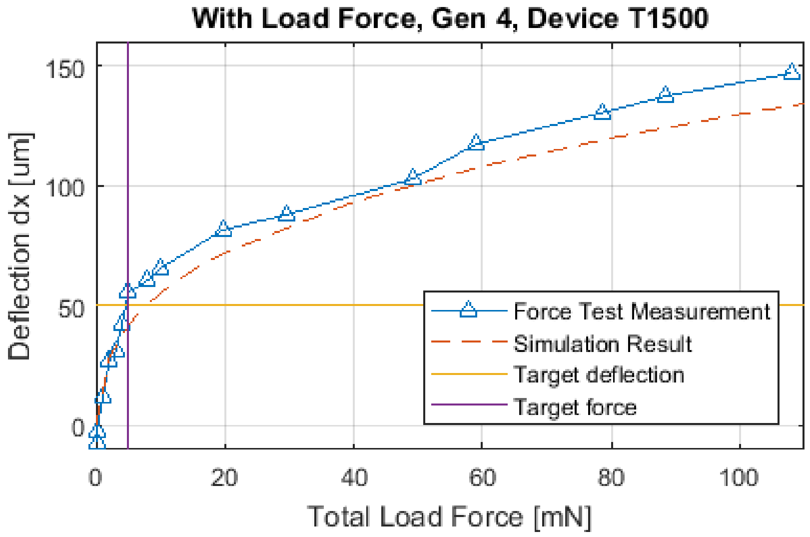

Figure 3-16 – Measured deflection vs. load force result in T1500 Device.

Result using T1500 device shows that the deflections were mostly slightly higher to the simulation result. Unlike in T1200 devices in which the pre-existing bending was not so obvious, the bending may have canceled out the factors that causes the deflections to be lower and simulation predicted. Although it is undesired that the actual reaction force is lower than expected at a given deflection, since we have included a safety factor in design, the deflection only needed to be slightly higher than the 50 µm target for the force to pass 5 mN. Considering the measurement precision from 300M pixel microscope images in which 1 pixel corresponds to 1.6 µm, this small force deficiency may be partly due to measurement error. For the design to be safer, future generations of the device should use more legs if using such leg dimensions.

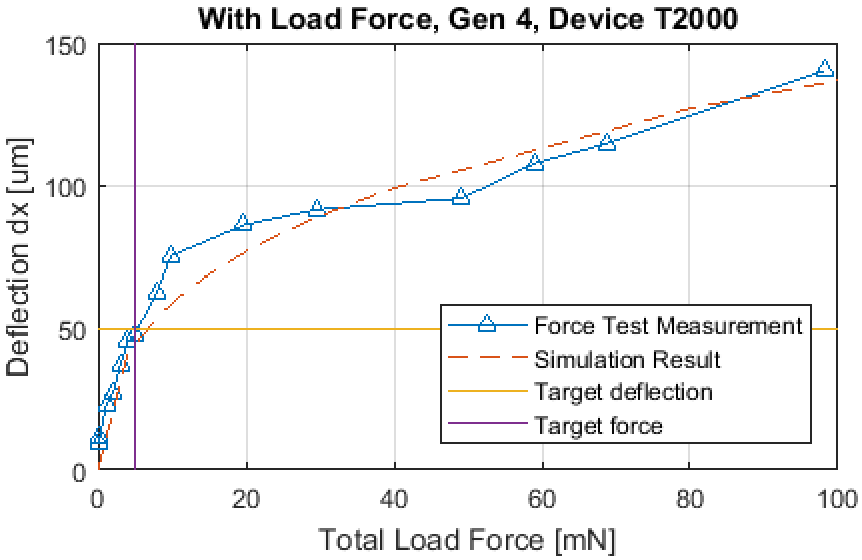

Figure 3-17 – Measured deflection vs. load force result in T2000 Device.

In the T2000 device, as shown in Figure 3-17, the measure results goes around the simulation curve. This could be a combined result of simulation simplification, pre-existing bending, or measurement error. Similar to the case of T1500 device, thanks to the safety factor used in design, the design target is still marginally achieved. For the design to be safer, future generations of the device should use more legs if using such leg dimensions.

In general, the measured results using different variations of the design showed that our simulation predictions were all within good range from the reality.

3.5.2 Challenges with the Elasticity Test

The simulation predictions of the forces and deflections at which the stress in the material reaches its estimated yield stress of 70 MPa are the follows:

Table 3-6 – Simulation predictions of the forces and deflections at which the stress in the material reaches its estimated yield stress.

			Deflection [µm]		Total load force [mN]	
Name	BeamL [µm]	# Pair of legs	At 1/3 yield stress	At yield stress	At 1/3 yield stress	At yield stress
T1200	1200	100	59	115	12	70
T1500	1500	200	81	153	28	160
T2000	2000	400	98	207	40	320

Theoretically, the elasticity of the material while the stress is lower than the yield can be tested by verifying that the legs may restore their original shape after the applied load is removed. However, this was proven to be challenging especially due to the pre-existing bending in the devices.

The T1200 device started with a 4.11 µm deflection before load was applied, and after the maximum load was applied and then removed, the deflection was measured to be 5.64 µm. Because the difference was only 1.53 µm, which was less than a pixel in the image, it was unclear whether it was due to loss of elasticity or due to measurement error. The result is highly inconclusive before repetitions of the experiment with many more devices may potentially provide more insights.

On the other hand, in the case of T1500 and T2000 devices, because the pre-existing bending was so severe, meaning that the legs were much longer than the distance between their two ends, the way of bending could be changed significantly by a very small force. This was verified by measuring the deflection of the legs when only the hook (0.1 mN) is attached on the device after different loads were added.

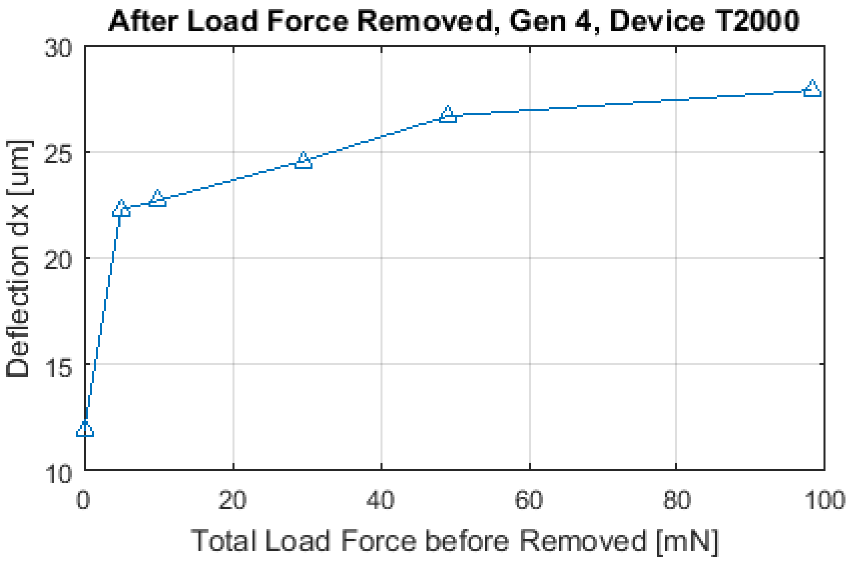

Figure 3-18 – Deflection of the legs in T2000 after load forces were removed.

As results in Figure 3-18 show, the 5 mN load already caused legs to bend 10 µm more in the direction of the shuttle after it is removed. The observation of severe leg bending in Figure 3-14e and the fact that the deflection vs. load force relationship in Figure 3-17 still greatly resembles the simulation result assuming full elasticity suggests that the increase in deflection after loads were released do not prove a lost in elasticity.

Unfortunately for T1500 and T2000 devices, the author was not able to add loads up to the predicted load force or deflection at the estimated yield, because the device heads holding the hook broke. In future experiments, adhesive material such as epoxy may be applied to the device head before experiments start to increase the strength of the heads.

Although the experiments did not prove or prove against loss of elasticity, the inability for the T1500 and T2000 device legs to restore their original shape was still discouraging of the design regardless of what cause it—plastic deformation or pre-existing bending. It still means that the distance the pulled-back shuttle will travel when the glue on the head melts is lower than expected. This, however, does not necessarily mean that the design is not usable. Assuming that the elasticity is still intact, it only means that initially the shuttle should be pulled further back.

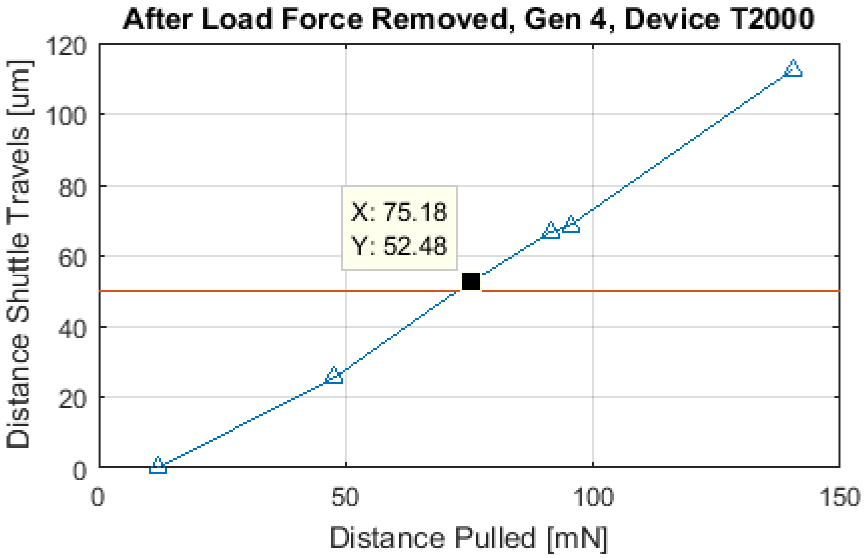

Figure 3-19 – Distance shuttle travels when load force is removed.

For example, Figure 3-19 shows the curve of the distance the shuttle traveled by the comparing the deflections with the load hanging on the shuttle and after the loads are removed. In order to make sure that the shuttle to travel 50 µm to pierce through the glial sheath, initially it should be pulled farther back to about 75 µm.

3.5.3 Discussions and Future Directions

Due to limited time, the tests were not repeated, so all findings were only preliminary. The fabrication process may vary slightly between wafers and fabrication batches, causing the material properties to change and hence affecting the mechanical performance. To more systematically study the mechanical properties of the devices and make sure of the performance of the product, more sample devices from different wafers or different batches should be tested.

Since the severe pre-existing bending caused unexpected complications in the mechanical performance of the device, the author recommend avoiding or minimizing the bending in future generations. An obvious way is to use shorter legs, as all devices with 1200-µm legs were generally flatter and their legs showed much less bending than the ones with 1500-µm or 2000-µm legs.

3.6 Gen 4 Benchtop Characterization: Impedance

Impedance tests using the same setup and procedure as introduced in Section 2.3 were run using Gen 4 devices to verify whether the modified fabrication process has made improvements on the issue of impedance dropping over time. Measurements were taken every 1 or 2 minutes to give a better temporal resolution of the change and minimize the effect of occasional data loss due to GPIB communication errors between the impedance analyzer and the computer.

3.6.1 Device 1

3.6.1.1 Experiment 1

In Experiment 1, the tip of the device was put in PBS for 23 hours to observe the change of impedance over time.

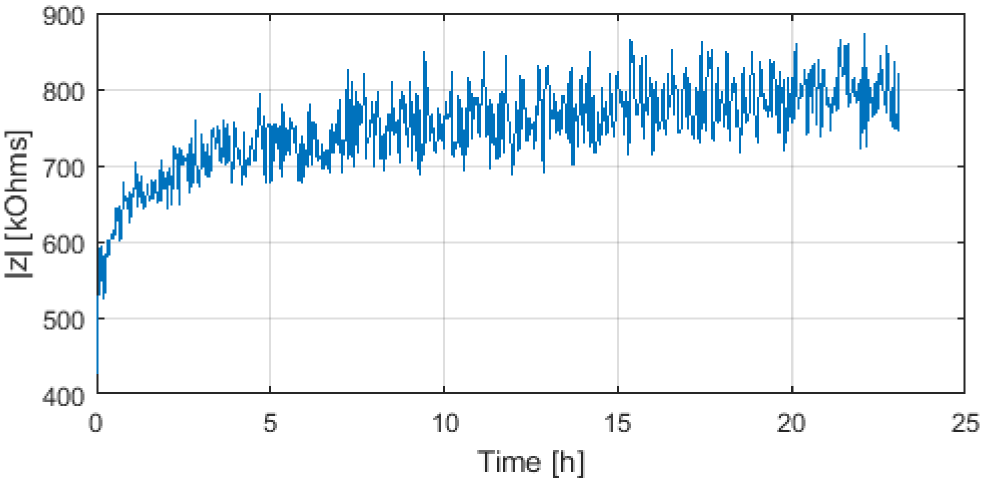

Figure 3-20 – Experiment 1: impedance magnitude of Gen 4 Device 1 tip in PBS at 1 kHz over time for 23 h.

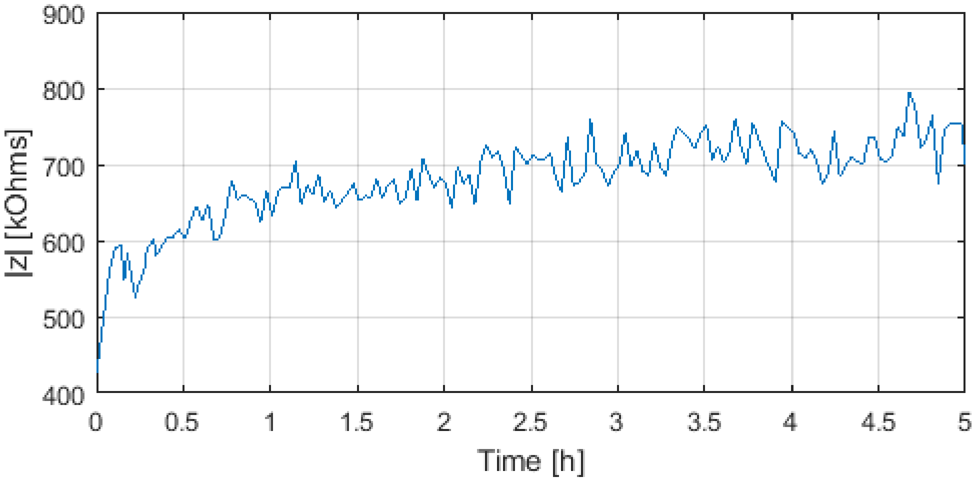

Figure 3-21 - Experiment 1: impedance magnitude of Gen 4 Device 1 tip in PBS at 1 kHz over time for 23 h: first 5 hours.

As shown in Figure 3-20, the trend was opposite to the case of the Gen 3 device we tested under the same experimental setting. It started at around 500 to 600 kΩ, which is in the range of typical Gen 3 devices [11], which makes sense because Gen 4 has identical tip electrode site opening design as Gen 3. Then the magnitude of impedance rose up to about 800 kΩ in 15 hours, which is also in the range of typical Gen 3 device measurements. Then unlike the Gen 3 device in DI water that showed a drop in impedance after 20 hours, the impedance stayed relatively stabilized.

Since our fabrication improvements were based on the delamination hypothesis of the impedance drop in Gen 3 devices, and now the impedance is no longer dropping rapidly, Figure 3-20 proves that that our delamination hypothesis was likely right and the modifications were effective.

And since the time frame of increase in the initial 15 hours is similar to that in the case of the Gen 3 device with tip in DI water, the cause of the increase could be similar. Our assumption was that initially the ions from the Aluminum etchant stored in the PI layers dissolved in water and caused a higher concentration of electrolytes around the device tip. Then as they diffused away the concentration was back down. The reason that this increase did not show in the case with Gen 3 device in PBS could be that the drop due to delamination was too dominant.

3.6.1.2 Experiment 2

To test whether the increase observed in Experiment 1 was reversible, after Experiment 1, Device 1 was rinsed in DI water and dried in room temperature for 20 min, then the tip was put back in PBS with constant level.

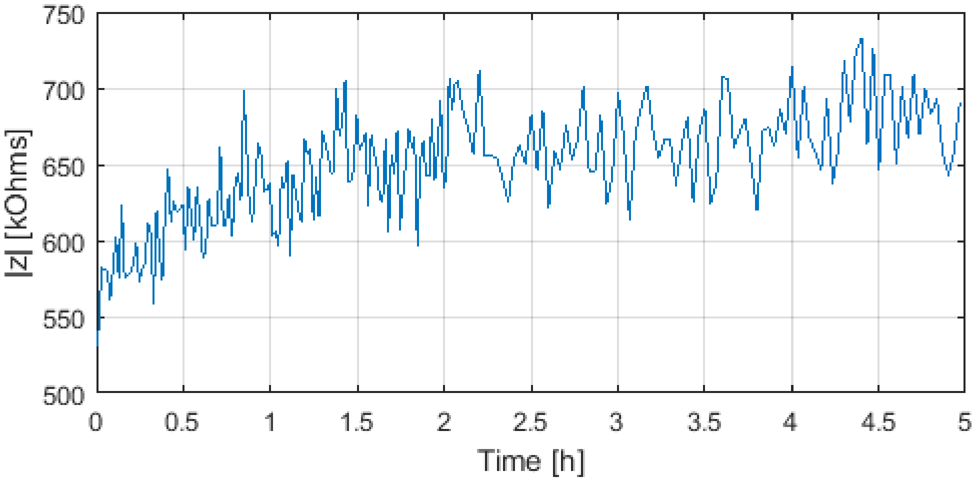

Figure 3-22 – Experiment 2: impedance magnitude of Gen 4 Device 1 tip in PBS at 1 kHz over time for 5 h, after rinsed in DI water and dried after Experiment 1.

As shown in Figure 3-22, initially the magnitude dropped back to about 500 to 600 kΩ. Then in 5 hours, it slowly increased to about 700 kΩ. Unfortunately, the device became open circuit after 5 hours. A careful inspection of the metal traces under 40x microscope revealed no visible cracks in the electrode traces. It could be due to invisible small cracks in the traces caused by the wrinkles shown in xxxxxxxxxxxxxx. It could also be due to the failure of the connection point between the stainless steel wire and the contact pad of the device by silver epoxy, which was unable to be reworked without damaging the device.

The start value range, end value range and rate of increase in the first 5 hours were very similar to those in Experiment 1 in Figure 3-21. The measurements in Experiment 2, however, was noisier, suggesting more instability of the electrical path. The increase of instability was likely due to the rinse in DI water, which could have damaged the trace already fragile due to the wrinkles.

The initial increase's still being present and having the same time frame could be because of the salt on the surface and in PI causing effects similar to that caused by the etchant residues, since the device was only rinsed promptly because it was fragile. However, it is uncertain whether the effect should be as strong. It could also mean that our previous hypothesis was incorrect.

Another potential causes is swelling of the PI covering the electrode site. But it is unlikely that the PI would have completely dried and resumed its volume in 20 minutes between the two experiments.

It could also potentially be because the water injection rate controlled by the syringe pump did not precisely match the evaporation rate, causing the PBS concentration to change slightly. However, this is unlikely because the change of PBS solution volume should still be very small compared to the total volume, which should not cause a change of almost 50% in the measured impedance in a day.

The effect by the position of the syringe pump injection pipe and the device was also eliminated because the device was at least 2 cm from the pipe and their relative position was changed in between Experiment 1 and 2. If it is because the PBS concentration is lower near the water injection point, the rising rates in the two experiments should not match. Also, since the injection rate was very slow (10 µL/min), it is unlikely that it would lower the concentration significantly enough to affect the measurement result in a place not in its direct adjacency (more than 2 cm away).

Other causes include slightly stirring of the PBS solution due to the insertion of the device and height adjustment of the holding z-stand causing a temporary drop in impedance. This hypothesis was tested with the next device.

3.6.2 Device 2

3.6.2.1 Experiment 3

Another device was put in PBS for a longer period of time to observe whether the impedance magnitude changes further after the seemingly stabilized level was reached after 15 hours.

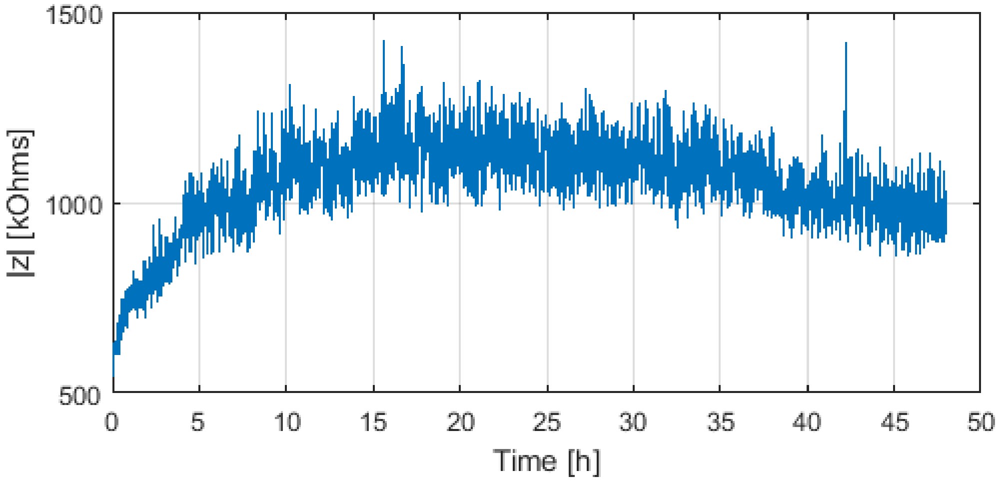

Figure 3-23 - Experiment 3: impedance magnitude of Gen 4 Device 2 tip in PBS at 1 kHz over time for 48 h.

Figure 3-23 shows that the trend in the first 23 hours of Device 2 were similar to that of Device 1 in the previous two experiments. However, although the trends started in a similar range, in the case of Device 2, the trend increased to a much higher value around 1.1 to 1.2 MΩ, which, however, is still within the typical range [11].

After about 25 hours, a decreasing trend started. The decrease was very slow and it was unclear to what value since it seemed to continue decreasing at the 48-hour mark, when the value was about 1 MΩ.

Due to limited time, this experiment was not continued.

3.6.2.2 Effect of stirring

After the impedance magnitude was initially stabilized, the author manually stirred the PBS solution in the container to see whether the stirring may be the explanation of the initial increase after the tip was put in PBS. The stirring was not very violent such that the PBS level was almost maintained during the process.

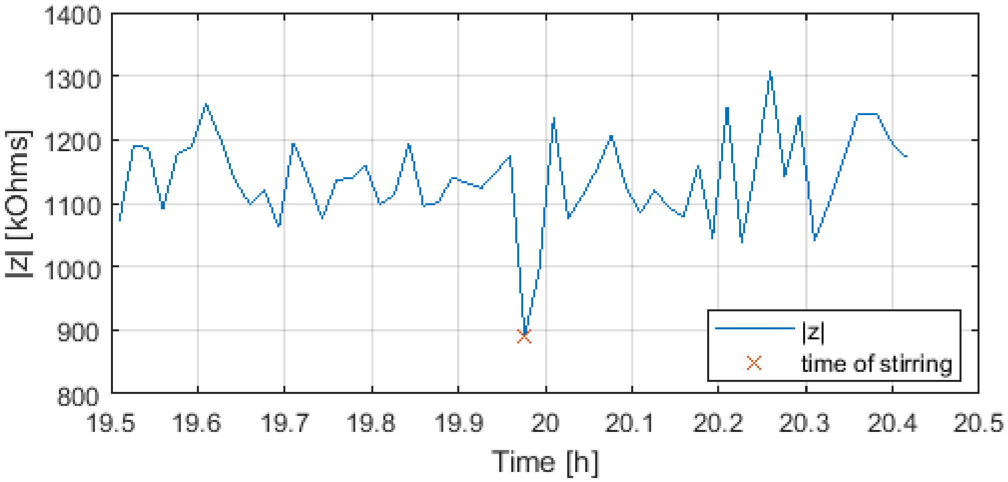

Figure 3-24 – Measured impedance magnitude of Gen 4 Device 2 tip in PBS at 1 kHz around the time of stirring of the PBS.

Figure 3-24 shows the hour around the time of stirring. Although the stirring did temporarily decrease the impedance, the original level was restored in 2 min. This was a very short restoring time compared to the 15-hour increase after the device tip was put in PBS in all three experiments so far. Therefore, the hypothesis that turbulence of the PBS solution due to injection of device was more likely false.

3.6.3 Discussions and Future Directions

Experiments using Gen 4 devices showed that the impedance magnitudes measured did not decrease rapidly like using Gen 3 device, and the magnitude stayed in the designed range of the device during the experiments.

However, an increase of the impedance in the first 15 hours showed up in all three experiments, as well as the later much slower decrease after 25 hours in Experiment 3. The cause of the increase and the timeline remains uncertain. In future experiments, if time allows, the experiments may be run for longer periods (~weeks) to make a better characterization of the change of impedance over time and they may provide more insights to the observations in the three experiments here.

The failure of Device 1 after 5 hours in Experiment 2 suggested that the wrinkles in the electrode traces (see Section 3.4.3.2) might have caused them to be very fragile. Therefore, modifications of the next generation's fabrication process should avoid these wrinkles.

3.7 Conclusions

On the mechanical aspect, measurement results of leg deflection vs. load weight using test devices with different leg lengths confirmed that our simulation model made a considerably good approximation of reality. They showed that the modified design was able to meet the design targets. During the experiment, the measurement of leg deflection of the device prior to holding any load weight revealed that when the device legs are long, they suffer severe bending even at rest, which is a problem that should be avoided in future generation design. Due to this bending and the lack of repetition of the experiment, whether the deformation of the legs was elastic or plastic at the target force remains inconclusive.

On the electrical aspect, impedance tests showed that the impedance magnitude of the electrode sites were no longer dropping rapidly as in Gen 3 devices. This suggests that our modification of the fabrication process successfully improved the adhesion between the PI layers. However, longer experiments should be performed before concluding that the delamination problem is solved. Meanwhile, wrinkles in the metal traces were observed, which made the traces fragile and very likely caused electrical failure of one of the test devices. This means that the fabrication needs further improvements. Since the insufficient partial curing of the first PI layer was most probable source of the wrinkles, the curing temperature and time should be increased in future fabrications.

Chapter 4: Conclusions and Future Directions

4.1 Contributions

4.1.1 Mechanical Model and Benchtop Experiment Setup

This work provides a FEA simulation model setup of the spring structure using fixed-fixed beam with fillets and is capable of predicting the mechanical behavior of the actual fabricated device with considerably good accuracy, as verified by benchtop tests.

The benchtop experiment setup to measure deflection vs. load force on the structure is simple to use and requires only common lab supplies such as a microscope and a weighing balance. This setup can be used to perform systematic mechanical studies of the device design and the material. Alternatively, a digital camera with high resolution and good close-up clarity may be used in place of the microscope, since the magnification required was only 5x with a 300M camera. For this application, the weighing balance requires about 0.001 g readability, and 100 g capacity should be more than enough for studying the mechanical performances of the devices up to the yield point, if the simulation results are not far off. Therefore, equipment required in this setup can be potentially low-cost and easily accessible.

4.1.2 Real-Time Impedance Monitoring

The automatic impedance recording setup described and tested in this thesis provides a reliable tool to study the temporal change of the electrical behavior of this device, as well as any other electrical device whose temporal change in impedance may be of interest. The system is capable of taking an impedance measurements as fast as about every 20 seconds with reasonably good frequency sweeping resolution and averaging bandwidth. The complete raw data from the experiments can be automatically stored, and specific values of the impedance at frequencies of interest may also be extracted and recorded automatically. When the computer in control is connected to a network, the result may be remotely accessed anytime from anywhere, the progress of the experiment as well as whether there are problems occurring can be monitored constantly. Therefore, this system makes long-term experiments up to weeks or even months more convenient.

4.2 Future Directions

4.2.1 Fabrication

Although the fabrication modifications in Gen 4 were proven to have enhanced the adhesion between PI layers, they caused unexpected issues in the device such as wrinkles in the metal trace due to insufficient partial curing of the first PI layer. Therefore, in future fabrication using the PI and recipe, the optimal temperature and time of the curing of the first layer should be studied. There is no evidence to suggest any problems caused by the short plasma etch before depositing the second PI layer, or by the Ti layer in between the Au trace and the second PI layer, so these should be kept.

Insufficient opening of the electrode sites was also observed in some of the devices. The optimal spinning speed of the second PI precursor layer and its exposure time should also be studied to avoid the need of excessive plasma etching to open up the electrode sites.

Also, it should be tested whether the acid residue from the aluminum etchant used in device release is kept inside the devices, since it was one hypothesis for the impedance increase of the measured electrode sites in the *in vitro* setting. A device may be immersed in DI water of small but sufficient volume for days, and the DI water may be tested for the chemicals present in the etchant formula afterwards. If there was actually acid residue in the PI layers, additional steps should be considered to either remove or shield the acid from leaking before the devices are used for *in vivo* tests. One approach is to immersed the device in DI water of large quantity for long enough to maximally dissolve the acid ions. However, in such an approach, delamination and swelling caused by excessive direct exposure to DI water may be of concern.

4.2.2 Mechanical and Electrical Characterization

Due to the limited time and number of working devices from the Gen 4 fabrication batch available for this thesis, the experiments carried out were only from one to a few days. Devices from different wafers and different batches should be tested for mechanical properties to provide a more systematic characterization of the design.

Longer experiments of the impedance measurements should be carried out to gain a better knowledge of whether the delamination problem have been solved or was the delamination process only slowed down. The unexpected shape and value of the impedance phase vs. frequency could also be studied, potentially by first running simulations to see what combination of circuit elements produces similar magnitude and phase characteristics, then study the parts of the device that could perform as such circuit elements accordingly.

REFERENCE

[1] L. F. Nicolas-Alonso and J. Gomez-Gil, "Brain Computer Interfaces, a Review," *Sensors*, vol. 12, no. 2, p. 1211–1279, 2012.

[2] V. S. Polikov, P. A. Tresco and W. M. Reichert, "Response of brain tissue to chronically implanted neural electrodes," *Journal of Neuroscience Methods*, vol. 148, no. 1, pp. 1-18, 15 October 2005.

[3] J. N. Turner, W. Shain, D. H. Szarowski, M. Andersen, S. Martins, M. Isaacson and H. Craighead, "Cerebral Astrocyte Response to Micromachined Silicon Implants," *Experimental Neurology*, vol. 156, p. 33–49, 1999.

[4] A. Prasad and J. C. Sanchez, "Quantifying long-term microelectrode array functionality using chronic in vivo impedance testing," *J. Neural Eng.*, vol. 9, no. 2, p. 026028, 2 April 2012.

[5] L. Rao, H. Zhou, T. Li, C. Li and Y. Y. Duan, "Polyethylene glycol-containing polyurethane hydrogel coatings for improving the biocompatibility of neural electrodes," *Acta Biomaterialia*, vol. 8, no. 6, pp. 2233-2242, July 2012.

[6] J. P. Seymour and D. R. Kipke, "Neural probe design for reduced tissue encapsulation in CNS," *Biomaterials*, vol. 28, no. 25, pp. 3594-3607, September 2007.

[7] T. D. Y. Kozai, N. B. Langhals, P. R. Patel, X. Deng, H. Zhang, K. L. Smith, J. Lahann, N. A. Kotov and D. R. Kipke, "Ultrasmall implantable composite microelectrodes with bioactive surfaces for chronic neural interfaces," *Nat. Mater.*, vol. 11, no. 12, p. 1065–1073, December 2012.

[8] H. C. Lee, F. Ejserholm, J. Gaire, S. Currlin, J. Schouenborg, L. Wallman, M. Bengtsson, K. Park and K. J. Otto, "Histological evaluation of flexible neural implants; flexibility limit for reducing the tissue response?," *Journal of Neural Engineering*, vol. 14, no. 3, 4 May 2017.

[9] N. Jackson, A. Sridharan, S. Anand, M. Baker, M. Okandan and J. Muthuswamy, "Long-Term Neural Recordings Using MEMS Based Movable Microelectrodes in the Brain," *Front Neuroengineering*, vol. 3, no. 10, 2010.

[10] P. Stice and J. Muthuswamy, "Assessment of gliosis around moveable implants in the brain," *J Neural Eng.*, vol. 6, no. 4, p. 046004, 2009.

[11] A. Dighe, "Reconfigurable Neural Probes for Chronic Electrical Recording," Cambridge, MA, 2015.

[12] M. Ghosh, Polyimides: Fundamentals and Applications, CRC Press, 1996, p. 784.

[13] R. Elliott, "Deflection of beams," The Central London Area Group of the Scalefour Society, 30 December 2010. [Online]. Available: http://www.clag.org.uk/beam.html. [Accessed 28 July 2017].

[14] "Rectangular Area," efunda, [Online]. Available: http://www.efunda.com/math/areas/rectangle.cfm. [Accessed 28 July 2017].

[15] E. Oberg, F. D. Jones, H. L. Horton and H. H. Ryffel, Machinery's Handbook, 28th Edition, New York, NY: Industrial Press, 2008, p. 258.

[16] J. M. Gere, Mechanics of Materials, 6 ed., Belmont, CA: Brooks/Cole–Thomson Learning, 2004, p. 313.

[17] "COMSOL Multiphysics User's Guide," COMSOL AB., May 2012. [Online]. Available: http://people.ee.ethz.ch/~fieldcom/pps-comsol/documents/User%20Guide/COMSOLMultiphysicsUsersGuide.pdf. [Accessed 17 August 2017].

[18] "HD MicroSystems™ Product Selection Guide," HD MicroSystems™, December 2013. [Online]. Available: http://www.hdmicrosystems.com/HDMicroSystems/en_US/pdf/ProductSelectorGuide.pdf. [Accessed 20 August 2017].

[19] M. E. Grady, P. H. Geubelle and N. R. Sottos, "Interfacial adhesion of photodefinable polyimide films on passivated silicon," *Thin Solid Films,* vol. 552, p. 116–123, 2014.

[20] N. E. Dowling, Mechanical Behavior of Materials, 4 ed., Pearson, 2013, p. 298.

[21] M. Acin, "Stress singularities, stress concentrations and mesh convergence," 2 June 2015. [Online]. Available: http://www.acin.net/2015/06/02/stress-singularities-stress-concentrations-and-mesh-convergence/. [Accessed 29 July 2017].

[22] N. Tullini and M. Savoia, "Logarithmic stress singularities at clamped-free corners of a cantilever orthotropic beam," *Composite Structures,* vol. 32, no. 1–4, pp. 659-666, 1995.

[23] H. Sönnerlind, "Singularities in Finite Element Models: Dealing with Red Spots," COMSOL Inc., 3 June 2015. [Online]. Available: https://www.comsol.com/blogs/singularities-in-finite-element-models-dealing-with-red-spots/. [Accessed 29 July 2017].

[24] "Direct Write Pricing," Front Range Photo Mask, [Online]. Available: https://frontrange-photomask.com/direct-write-pricing-2/. [Accessed 4 February 2017].

[25] A. I. H. Committee, ASM Handbook, Volume 1: Properties and Selection: Irons, Steels, and High-Performance Alloys, ASM International, 1990, p. 199.

[26] Transene Company Inc., *Safety Data Sheet, Aluminum Etchant Type A.*

[27] "HD-4100 Process Guide," HD Microsystems™, September 2009. [Online]. Available: http://www.hdmicrosystems.com/content/dam/dupont/products-and-services/electronic-and-

electrical-materials/semiconductor-fabrication-and-packaging-materials/documents/HD-4100_ProcessGuide.pdf. [Accessed 20 August 2017].

[28] J. K. Nguyen, D. J. Park, J. L. Skousen, A. E. Hess-Dunning, D. J. Tyler, S. J. Rowan, C. Weder and J. R. Capadona, "Mechanically-compliant intracortical implants reduce the neuroinflammatory response," *J. Neural Eng.,* vol. 11, no. 5, p. 056014, October 2014.

[29] J. Thelin, H. Jörntell, E. Psouni, M. Garwicz, J. Schouenborg, N. Danielsen and C. E. Linsmeier, "Implant Size and Fixation Mode Strongly Influence Tissue Reactions in the CNS," *PLoS ONE,* vol. 6, no. 1, p. e16267, January 2011.

[30] A. Jackson and E. E. Fetz, "Compact Movable Microwire Array for Long-Term Chronic Unit Recording in Cerebral Cortex of Primates," *J. Neurophysiol.,* vol. 98, no. 5, p. 3109–3118, November 2007.

[31] A. B. Schwartz, X. T. Cui, D. J. Weber and D. W. Moran, "Brain-controlled interfaces: movement restoration with neural prosthetics," *Neuron,* vol. 52, no. 1, p. 205–220, October 2006.